2012

Failure Analysis Of Impact-damaged Metallic Poles Repaired With Fiber Reinforced Polymer Composites

Robert Arthur Slade
University of Central Florida

FAILURE ANALYSIS OF IMPACT-DAMAGED METALLIC POLES REPAIRED WITH FIBER REINFORCED POLYMER COMPOSITES

by

ROBERT ARTHUR SLADE
B.S.C.E University of Central Florida, 2010

A thesis submitted in partial fulfillment of the requirements
for the degree of Master of Science
in the Department of Civil, Environmental, and Construction Engineering
in the College of Engineering and Computer Science
at the University of Central Florida
Orlando, Florida

Spring Term
2012

Major Professor: Kevin R. Mackie

ABSTRACT

Metallic utility poles, light poles, and mast arms are intermittently damaged by vehicle collision. In many cases the vehicular impact does not cause immediate failure of the structure, but induces localized damage that may result in failure under extreme service loadings or can promote degradation and corrosion within the damaged region. Replacement of these poles is costly and often involves prolonged lane closures, service interruption, and temporary loss of functionality. Therefore, an *in situ* repair of these structures is required.

This thesis examines the failure modes of damaged metallic poles reinforced with externally-bonded fiber reinforced polymer (FRP) composites. Several FRP repair systems were selected for comparison, and a set of medium and full-scale tests were conducted to identify the critical failure modes. The material properties of each component of the repair were experimentally determined, and then combined into a numerical model capable of predicting global response.

Four possible failure modes are discussed: yielding of the unreinforced substrate, tensile rupture of the FRP, compressive buckling of the FRP, and debonding of the FRP from the substrate. It was found that simple linear, bilinear, and trilinear stress-strain relationships accurately describe the response of the composite and substrate components, whereas a more complex bond-slip relationship is required to characterize debonding. These constitutive properties were then incorporated into MSC.Marc, a versatile nonlinear finite element program. The output of the FEM analysis showed good agreement with the results of the experimental bond-slip tests.

To my parents

ACKNOWLEDGMENTS

The research presented in this document was conducted in conjunction with projects sponsored by the Florida Department of Transportation (FDOT). Additionally, the following individuals contributed to the success of this research:

- David Wagner, FDOT Structures Research Center
- Alberto Sardinas, FDOT District 4
- Chris Lazzara, Neptune Research Inc.
- David Wilburn, CarbonWrap Solutions LLC
- Cara Brown, UCF
- James Duryea, UCF

To all of the other students working in the UCF Structures Lab, thank you for providing a supportive, fun, and often humorous atmosphere in which to work:

- Patti AuBuchon
- Nick Najdovski
- Elie Zghayar
- Masoud Malekadeh
- Jun Xia, Ph.D
- Zachary Haber, UNR
- MJ Levy
- Tom Terrell
- Christopher Vanek

TABLE OF CONTENTS

LIST OF FIGURES

LIST OF TABLES

(1) INTRODUCTION

1.1 Problem Statement

Steel and aluminum utility poles, light poles, and mast arms are intermittently damaged by vehicle collision. In 2000, there were 1,103 fatalities and about 60,000 injuries related to utility pole crashes in the United States (Ivey & Scott, 2004). In many cases the vehicular impact does not cause a global failure of the structure, but only induces localized damage (see Figure 1 and Figure 2). This damage may not cause immediate collapse of the structure, but under extreme service loadings may result in a failure, or can promote degradation and corrosion within the damaged region. Replacement of these poles is costly and often involves prolonged lane closures, service interruption, and temporary loss of functionality. Therefore, *in situ* repair of these damaged structures is required for effective asset management.

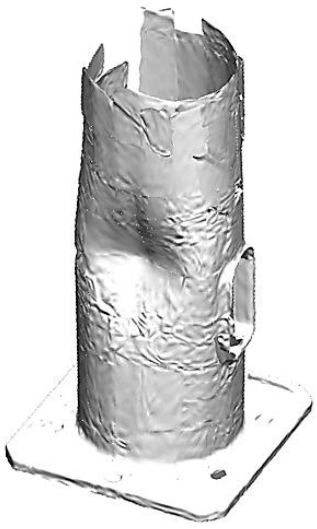

Figure 1. Laser scan of dented steel utility pole

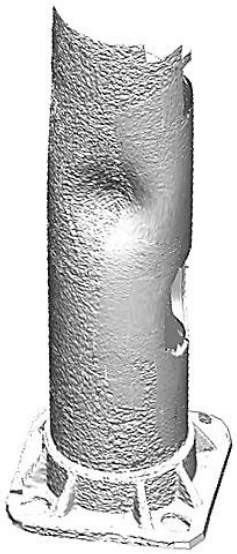

Figure 2. Laser scan of dented aluminum utility pole

There are few options available for repairing these structures including the use of steel jackets attached around the exterior of the dented region, cutting and welding a repair plate to the damaged portion, or filling the interior of the pole with grout. Additionally, externally-bonded fiber reinforced polymer (FRP) composites have been successfully used to repair these structures. This repair technique allows for inexpensive, in-place, and speedy restoration without the need for large equipment, service interruption, or lane closures.

This thesis examined the failure modes of damaged metallic poles reinforced with externally-bonded FRP composites. Several FRP repair systems were compared, and a set of medium and full scale tests were conducted to determine the critical failure modes. Each dominant failure mode was identified and examined. Then the material properties of each component were experimentally determined and combined into a numerical model capable of predicting system response.

1.2 Research Objectives

A recent study was funded by the Florida department of Transportation (FDOT) to determine the effectiveness of using externally-bonded fiber reinforced polymer composites to repair impact-damaged metallic poles. That study found that externally-bonded FRP was capable of returning the structures to their previous capacity; however, additional study is required to develop a standard design guideline for such a repair.

This thesis will experimentally identify and quantify each likely failure mode of poles repaired with externally-bonded FRP. A material response relationship for the components that related to each failure mode will be determined and incorporated into a nonlinear finite element model capable of predicting system response.

1.3 Thesis Outline

This thesis is presented in the following format:

1) *Literature Review*: The literature presented is a comprehensive overview of the background, materials, and previous work integral to the motivation and understanding of this study. Also included are summaries of composite design and a brief overview of the relevant design guidelines.
2) *FRP Repair Systems*: A rationale describing which FRP repair systems were selected, and the material properties supplied by the manufacturer of each component of the various repair systems are presented.
3) *Experimental Testing*: A series of large-scale tests were performed to study the response of damaged metallic poles repaired with FRP and to identify the various failure modes of these structures.
4) *Failure Modes*: The failure modes identified from experimental testing are described by the material response of one or more of the system components. To quantify this response, several small-scale tests were conducted and simple relationship models were developed for each component. These material properties and relationships were then incorporated into a nonlinear finite element model.
5) *Discussion and Conclusions*: Based on the results of the tests conducted, conclusions are drawn relating to each failure mode, as well as the accuracy of the nonlinear finite element model produced. Areas for additional future research are also suggested.

(2) LITERATURE REVIEW

The following chapter includes the literature review that was conducted for this study. This chapter initially surveys the current applications of externally-bonded fiber reinforced polymers (FRP) composites as related to civil infrastructure, and then covers the material components that make up an FRP. Finally, the standard approach for modeling FRP, and the current set of guidelines concerning structural FRP design are presented in summary.

2.1 Civil Infrastructure Applications of FRP

The use of externally-bonded FRP to reinforce civil infrastructure has been studied and developed for many years. Beginning with applications on concrete bridge girders and decks in the 1980s applications have extended to column and pile reinforcement, seismic retrofit of joint connections, and even reinforcing blast walls (Sen, et al., 2007).

More recent studies have examined the use of FRP for pressurized pipe repair (Schaumann, et al., 2005; Hauch & Bai, 1999), and steel bridge applications (Schnerch, et al., 2007). Several other studies have focused on reinforcing wood, concrete, and steel utility poles used to support power cables, cameras, lighting, signaling, and signage. However, thus far these studies primarily dealt with improving the maximum carrying capacity of the structures, and not repairing damaged elements (Chahrour & Soudki, 2006; Lanier, et al., 2009; Polyzois & Kell, 2007)

2.2 Externally-Bonded FRP Composites

Fiber reinforced polymer (FRP) composites are advanced materials consisting of fibers impregnated with a polymer matrix. The fibers act as the primary strengthening element, while the matrix transfers stress to the fibers and maintains the fiber orientation. Externally-bonded FRP reinforcement is a structural repair technique in which these composites are adhered to the exterior surface of a structural member. This form of retrofit allows for quick installation, while maintaining a low profile that can conform to the shape of the member. Additionally, by selecting different fibers or matrix materials, the properties of the FRP can be optimized and tailored for any given application.

2.2.1 Epoxy-Matrix Composites

Epoxy resins are the most common matrix material used in externally-bonded FRP composites. Though epoxy resins are considered more expensive than many other matrix materials, they have several advantages that add to their popularity. Among these are high strength, low viscosity, good fiber wetout, low volatility, low shrinkage, and ease of availability (Kaw, 2006).

A wet layup process is used for externally-bonded applications. This involves combining the epoxy resin with a hardener that initiates a chemical reaction curing the mixture. The fibers are then impregnated with the resin by saturation at room temperature. The FRP composite can then be affixed to the substrate directly, relying on the adhesive properties of the epoxy as it cures, or a separate adhesive primer layer can be used.

2.2.2 Polyurethane-Matrix Composites

Relatively new to the field of structural composites, polyurethanes are a group of resins that exhibit similar chemical and physical properties to each other. Generally, polyurethane resins display good fiber wetout, have a rapid cure time, are cost effective, and work well at low temperatures. However, research has shown that they also have limited thermal and hydraulic stability, are sensitive to bulk moisture, and are critically affected by curing conditions (Haber, et al., 2009).

As opposed to epoxy resins, polyurethanes are activated by exposure to water. Therefore, a standard wet layup process is impractical. Instead, pre-impregnated woven fiber meshes (prepregs) are cut to length and kept hermetically sealed until installation, at which point they are exposed to water and set in place for curing. Typically this process involves the use of a separate adhesive primer layer to affix the polyurethanes prepreg to the substrate.

2.2.3 Concrete Substrate

Use of externally-bonded FRP composites to reinforce structural concrete members has become increasingly popular in the last few decades. Much research has been conducted to investigate the effectiveness of such a repair, and the mechanical response is well understood. Studies have shown that externally-bonded FRP composites can be used to improve the stiffness, static, cyclic, and fatigue load caring capacity, and environmental durability of a structural member (Buyukozturk, et al., 2004).

However, a primary design consideration for FRP-strengthened concrete members is FRP debonding. Due to the sudden and unpredictable nature of a debonding failure, the FRP reinforcement may cause a brittle failure, thus decreasing the overall level of safety (Gunes,

et al., 2009). Another important design consideration is shear failure. FRP tension reinforcement can cause the applied load to exceed the shear capacity of an RC member. Side bonding and U-jacketing of FRP can help to increase the shear capacity, but shear debonding and cover peel-off become critical failure modes (Pellegrino, et al., 2008).

2.2.4 Metallic Substrate

Unlike concrete, externally-bonded FRP has only recently been investigated for use on steel or aluminum structures. The low material characteristics of FRP and the ease with which it can be added to a structural element make it an ideal candidate for many retrofit situations.

However, one concern associated with using FRP to reinforce metallic structures is the possible electro-chemical interaction. Specifically, when dealing with carbon fiber composites, galvanic corrosion is a major concern. Due to the high degree of galvanic potential associated with carbon, if these composites come in contact with a metallic substrate that is low in the galvanic series, such as steel or aluminum, the potential for corrosion is large (Hollaway & Cadei, 2002). Therefore, precautions must be taken when dealing with CFRP reinforcement of steel or aluminum structures.

2.2.4.1 Steel Substrate

Studies involving FRP reinforcement of steel bridges began in the 1990s and were shown to be a promising form of retrofit (Zhao & Zhang, 2007). These studies indicate that bonding FRP to the tension face of a steel girder can increase the overall stiffness and strength of a structure (Miller, et al., 2001). More recent studies examine using FRP in

conjunction with concrete grout to reinforce deficient steel column sections. The FRP is often used as a confining formwork to house the concrete grout that encompasses the existing steel column member (Karimi, et al., 2010). This composite repair technique was shown to increase the overall capacity of the member, but has not yet become commercially prevalent.

A recent study examined FRP reinforcement of steel circular hollow sections (CHS). The focus was to derive an analytical method to determine the ultimate capacity of FRP reinforced CHS beams subjected to bending loads (Haedir, et al., 2009). The moment capacities of steel CHS reinforced with FRP are derived for three assumed material responses: elastic, elastic-perfectly-plastic, and plastic conditions. The stress and strain distributions for these conditions are given in Figure 3. However, it should be noted that the method derived is only applicable for analysis of symmetrically round sections, and not damaged or dented cross-sections.

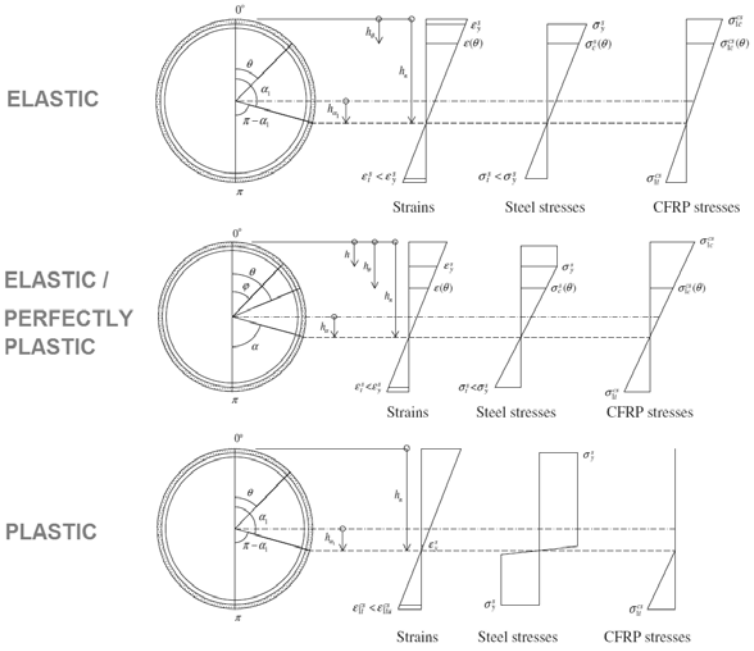

Figure 3. Strain and stress distributions under various material conditions (Haedir, et al., 2009)

Additional studies were conducted involving polygonal monopoles strengthened with CFRP. These studies involved pultruded CFRP plates or wet-layup CFRP sheets that were adhered at the base directly on the outside of large steel monopoles. Due to the cross-sectional geometry of these poles, the FRP was applied in flat sheets as can be seen in Figure 4. These studies demonstrated that FRP is a viable option for increasing the strength and stiffness of poles subjected to a cantilever loading, as can be seen in Figure 5 (Schnerch & Rizkalla , 2004).

Figure 4. CFRP reinforcement on steel monopole (Schnerch & Rizkalla , 2004)

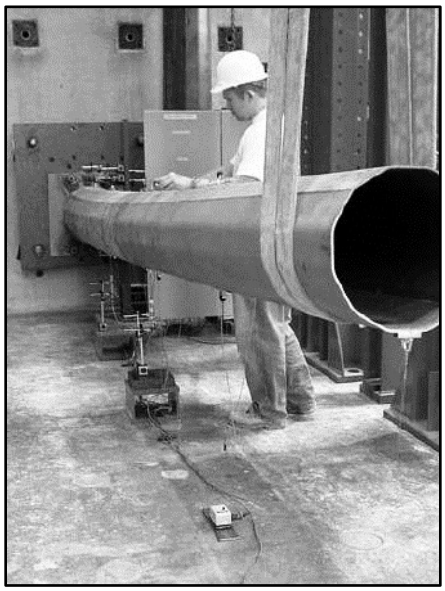

Figure 5. Test of CFRP strengthened monopole (Schnerch & Rizkalla , 2004)

2.2.4.2 Aluminum Substrate

Investigation into the use of FRP reinforcement of aluminum sections is only in its infancy, with few comprehensive studies being completed. One study involving high-modulus carbon fibers and various commercial adhesives found that externally-bonded FRP plates were effective in resisting web buckling of rectangular aluminum tube sections, though

it was also found that little additional capacity was gained by extending the FRP beyond the load bearing region (Islam, et al., 2011).

One set of studies was conducted within the past decade to examine the use of FRP to repair fatigued joints on aluminum highway sign structures. It was found that fatigue induced cracking was resulting in failure of these structures at welded joints. Therefore, several agencies such as the Delaware, Utah, and New York State departments of transportation funded studies which concluded that commercial FRP systems involving both glass and carbon fibers could be used to economically restore damaged aluminum joint connections (Fam, et al., 2006; Pantelides, et al., 2003; Bhattacharya & Seifried, 2005). These studies focused on welded joint failure of a small-diameter section, and did not suggest a repair approach for the primary vertical component of sign structures. Few additional studies exist that have looked at the infrastructure applications of FRP reinforcement applied to aluminum structures.

2.3 Modeling of FRP Composites

Modeling of fiber reinforced polymers, as with any composite material, involves a more complicated design method than traditional isotropic, homogeneous materials. The benefits that can be obtained by combining multiple materials with different properties into a single composite material fundamentally require a different approach. The internal physical properties of an FRP act like an orthotropic material and are modeled by the rule of mixtures, while the bond between the FRP and the substrate can often best be modeled using nonlinear finite element (FE) software.

2.3.1 FRP Material Properties

Externally-bonded FRP composites consist of a fiber weave suspended within a polymer matrix. These composites have layers of fibers that produce a single dominant direction of stiffness and strength. By varying the orientation of these fiber layers, the overall properties of the element can be customized to fit the requirements of the design. Each individual layer, or lamina, can be analyzed separately, and then the macro-mechanical response of the laminate can be compiled from the component properties. Presented in the following sections are several fundamental equations describing the material response and strength characteristics of FRP composites. The complete derivations for these formulas are given by Kaw (2006).

2.3.1.1 Mechanical Properties of FRP Composites

The mechanical properties of a lamina are described by the rule of mixtures, which states that the properties of the lamina are determined by the properties of the components within the composite, proportionately. For FRP composites, these proportions are volumetric. Total volume of fibers (in a single layer of FRP) divided by the total volume of fibers and matrix (in a single layer of FRP) is called the fiber volume fraction, and is typically abbreviated as V_f. The remaining volume of matrix divided by the total volume is called the matrix volume fraction, and is typically abbreviated as V_m. Therefore, the sum of V_f and V_m necessarily equals 1, assuming no voids are present within the lamina.

Most FRP composites have a stress vs. strain relationship that behaves nearly linearly; therefore, Hooke's law can be used to accurately define these materials (that is, $\boldsymbol{\sigma = E\varepsilon}$ and $\boldsymbol{\tau = G\gamma}$). Assuming continuous composite action between the fibers and matrix,

the modulus of elasticity of the lamina in the longitudinal direction (along fiber axis) can be given as:

$$E_1 = (E_f V_f) + (E_m V_m) \quad (1)$$

In the transverse direction the fiber and matrix displacements compound sequentially; therefore, the transverse modulus of elasticity follows the relation:

$$\frac{1}{E_2} = \left(\frac{V_f}{E_f}\right) + \left(\frac{V_m}{E_m}\right) \quad (2)$$

Due to the poisson's effect within the matrix (ν_m) and the fibers (ν_f), there is an overall relationship between the longitudinal and transverse strains in the lamina:

$$\nu_{12} = (\nu_f V_f) + (\nu_m V_m) \quad (3)$$

Similar to the transverse displacement, the fiber and matrix displacements compound sequentially in shear. Therefore, the shear modulus is found to be:

$$\frac{1}{G_{12}} = \left(\frac{V_f}{G_f}\right) + \left(\frac{V_m}{G_m}\right) \quad (4)$$

2.3.1.2 Strength Properties of a Lamina

While many theories exist that can describe the macroscopic failure criteria of a laminate, failure of a single layer of lamina will occur in one of five distinct ways: (1) longitudinal tensile failure, (2) longitudinal compressive failure, (3) transverse tensile failure, (4) transverse compressive failure, or (5) in-plane shear failure.

Typically, the fibers within a lamina are substantially stiffer than the matrix material. Additionally, the strain at failure of the fibers is significantly less than that of the matrix. Once the composite reaches the ultimate strain of the fibers in the longitudinal direction, the

fibers will fail. Neglecting the capacity of the unreinforced matrix, when the fibers fail the composite also fails, as is shown in Figure 6. Therefore, the critical value necessary for predicting longitudinal tensile failure is ultimate strain of the fibers:

$$\left(\sigma_1^T\right)_{ult} = V_f\left(\sigma_f\right)_{ult} + V_m\left(\varepsilon_f\right)_{ult} E_m \quad (5)$$

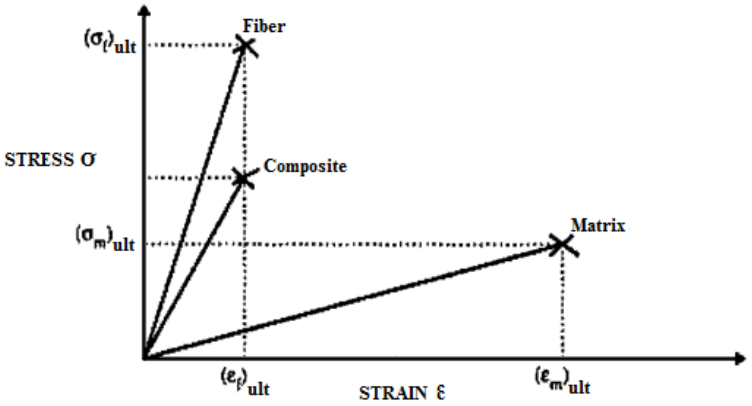

Figure 6. Stress-strain curve for unidirectional composite under uniaxial tensile load (Kaw, 2006)

Longitudinal compressive failure typically occurs in one of three forms: matrix strain failure, fiber micro-buckling, or fiber shear failure. The longitudinal compressive capacity is controlled by the minim of:

(1) Matrix strain failure mode:

$$\left(\sigma_1^T\right)_{ult} = \frac{E_1\left(\epsilon_2^T\right)_{ult}}{\nu_{12}} \quad (6)$$

where $\left(\epsilon_2^T\right)_{ult}$ can be calculated as,

$$\left(\epsilon_2^T\right)_{ult} = \left(\epsilon_m^T\right)_{ult}\left(1 - \sqrt[3]{V_f}\right) \quad (7)$$

(2) Fiber micro-buckling failure mode:

$$\left(\sigma_1^T\right)_{ult} = min\left\{2\left[V_f + \left(1 - V_f\right)\frac{E_m}{E_f}\right]\sqrt{\frac{V_f E_m E_f}{3\left(1-V_f\right)}}, \frac{G_m}{\left(1-V_f\right)}\right\} \quad (8)$$

(3) Fiber shear failure mode:

$$\left(\sigma_1^T\right)_{ult} = 2(\tau_{12})_{ult} \quad (9)$$

When determining the transverse tensile or compressive failure stresses, several key assumptions are made: under transverse loading the stress in the fiber and matrix are equal, and in this mode the failure will initially occur in the matrix before the fibers. Knowing the fiber diameter (*d*) and effective spacing (*s*) within the lamina, it can be shown that the following two equations are true for both tension and compression loading:

$$(\varepsilon_2)_{ult} = \left[\frac{d}{s}\frac{E_m}{E_f} + \left(1 - \frac{d}{s}\right)\right](\varepsilon_m)_{ult} \quad (10)$$

and

$$(\sigma_2)_{ult} = E_2(\varepsilon_2)_{ult} \quad (11)$$

Finally, to calculate the critical in-plane shear failure stress, the in-plane shear strain can be found based on the reasonable assumption that the shear strains in the fiber and matrix are equal. Following the same procedure as with the previous failure mode, it can be shown that:

$$(\gamma_{12})_{ult} = \left[\frac{d}{s}\frac{G_m}{G_f} + \left(1 - \frac{d}{s}\right)\right](\gamma_m)_{ult} \quad (12)$$

and

$$(\tau_{12})_{ult} = G_{12}(\gamma_{12})_{ult} \quad (13)$$

2.3.2 FRP Bond Modeling

A complex state of stress can exists within the bond between an FRP and the substrate material. The relationship between the shear stress and slip of the FRP is typically

used to describe the mechanics of the bond itself. The slip is the relative displacement of the FRP layer, with respect to the substrate. If sufficient bond length is present, the shear strain tapers to zero, so the total slip at the free end of the bond can be determined by integrating the strain along the length of the bonded area, parallel to the application of the shearing load. Similarly, the shear within the FRP can be found using the tensile modulus of the FRP and the ratio of axial strain to shear strain.

The total slip and shear stress at the free end of a lap can be found by:

$$\boldsymbol{\tau} = \sum \boldsymbol{E_f} \left(\frac{\boldsymbol{t_f}}{\boldsymbol{x_{i+1} - x_i}}\right) (\boldsymbol{\varepsilon_{i+1} - \varepsilon_i}) \qquad \textbf{(14)}$$

and

$$\boldsymbol{slip} = \int \boldsymbol{\varepsilon}_{(X)} \boldsymbol{dx} = \sum \left(\frac{\boldsymbol{\varepsilon_{i+1} - \varepsilon_i}}{\boldsymbol{x_{i+1} - x_i}}\right) \left(\frac{\boldsymbol{x^2}}{\boldsymbol{2}}\right) + (\boldsymbol{\varepsilon_i \cdot x}) \qquad \textbf{(15)}$$

where $\boldsymbol{\varepsilon_i}$ is the axial strain reading at the point $\boldsymbol{x_i}$, $\boldsymbol{t_f}$ is the thickness of the FRP plate, and $\boldsymbol{E_f}$ is the modulus of elasticity of the FRP (Mazzotti, et al., 2005).

The American Concrete Institute has identified several specific failure modes for FRP reinforce concrete beams. These are (1) concrete crushing before reinforcing steel yielding, (2) steel yielding followed by FRP rupture, (3) steel yielding followed by concrete crushing, (4) cover delamination, and (5) FRP debonding.

For concrete beams in particular, debonding usually occurs within a thin layer of the concrete substrate directly below the bond line. This form of failure occurs when a large deferential exists between the strains in the FRP and the concrete substrate (Gunes, et al., 2009). To avoid this, ACI enforces the following strain limit state calculations:

$$\boldsymbol{\varepsilon_{fe} = \varepsilon_{cu}\left(\frac{h-c}{c}\right) - \varepsilon_{bi} \leq \kappa_m \varepsilon_{fu}} \quad \textbf{(16)}$$

where $\boldsymbol{\kappa_m}$ is given as,

$$\boldsymbol{\kappa_m = \left.\begin{cases} \frac{1}{60\varepsilon_{fu}}\left(1 - \frac{\eta E_{FRP} t_{FRP}}{360000}\right) \leq 0.9 \quad for \quad \eta E_f t_f \leq 180000 \\ \frac{1}{60\varepsilon_{fu}}\left(1 - \frac{90000}{3\eta E_{FRP} t_{FRP}}\right) \leq 0.9 \quad for \quad \eta E_f t_f > 180000 \end{cases}\right\}_{SI\ units}} \quad \textbf{(17)}$$

and $\boldsymbol{\varepsilon_{fu}}$ is the ultimate FRP strain, $\boldsymbol{\varepsilon_{fu}}$ is the maximum allowable strain in the FRP, $\boldsymbol{\varepsilon_{cu}}$ is the ultimate strain of the concrete, $\mathbf{h}$ is the beam hight, $\mathbf{c}$ is the neutral axis depth, and $\boldsymbol{\varepsilon_{bi}}$ is the strain in the concrete substrate at time of installation. The limiting strain coefficient, $\boldsymbol{\kappa_m}$ is a function of the number of FRP layers ($\boldsymbol{\eta}$), the thickness of each layer ($\boldsymbol{t_{FRP}}$), and the modulus of elasticity of the FRP ($\boldsymbol{E_{FRP}}$) (ACI-440, 2008).

Bond-slip relationships for FRP adhered to concrete have a shape that can accurately be described by several functional forms. The most common forms include linear, bilinear, exponential, and linear-exponential relations. An example showing several of these curve shapes is presented in Figure 7.

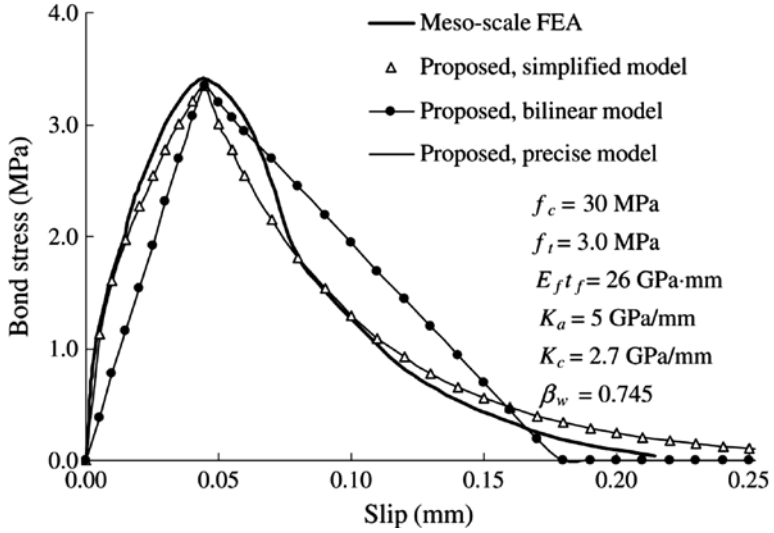

Figure 7. Common bond-slip relationship models (Lu, et al., 2005)

Less research has been conducted to explore the behavior of FRP bonded to steel or aluminum substrates. The plane of debonding failure for metallic substrata usually differs from concrete, where failure occurs within the substrate. Metals tend to produce stronger bonds that induce failure within the adhesive layer, or between the adhesive and substrate interface. This form of debonding action also tends to occur more quickly, making experimental observations difficult (Akbar, et al., 2010; Pantelides, et al., 2003). Though it also has also been shown that, when modeled properly using calibrated contact or interface elements, prediction of the bond-slip behavior can be quite accurate (Su, 2008).

2.4 Overview of Current FRP Design Guidelines

Multiple design guides and supporting documents have been created to codify a standard approach for designing externally-bonded FRP composite structures. Within the United States, ACI-440 has become the premier document on the subject, though AASHTO also has produced publications on the subject. In Europe FIB 9.3 has been adopted for use within the international EuroCode. On the whole, these guidelines pertain to FRP reinforcement of reinforced concrete structures, with little guidance available for FRP reinforcement of steel or other metals.

2.4.1 ACI-440

From 1991 onward, the American Concrete Institute (ACI) has sponsored the technical committee ACI-440 to examine FRP systems used to strengthen concrete structures. This committee produced ACI-440.2R-08: Guide for the Design and Construction of Externally-bonded FRP Systems for Strengthening Concrete Structures. This document is

based on over 20 years of research and investigation concerning FRP reinforcement of concrete structures. ACI-440 indicates that the primary area of uncertainty associated with any FRP/concrete systems is the bond interface, particularly for externally-bonded members. Additionally, as compared with more traditional systems, FRP has not been as thoroughly developed and is unproven when applied to many design situations. For these reasons, the design guidelines in ACI-440 are intended to be highly conservative.

2.4.2 AASHTO

The American Association of State Highway and Transportation Officials, AASHTO published a design guide in 2009 titled "LRFD Bridge Design Guide Specifications for GFRP-Reinforced Concrete Bridge Decks and Traffic Railings" in which several aspects of FRP reinforcement specific to bridge design were addressed. This guide offers a description of GFRP composite material properties, as well as provisions for the design and construction of concrete bridge decks and railings reinforced with GFRP reinforcing bars (AASHTO, 2009). As the title would indicate, this publication deals mostly with the use of FRP reinforcing bars and does not concentrate on externally-bonded reinforcement.

2.4.3 EuroCode

The International Federation for Structural Concrete (FIB) is a not-for-profit association housed in Switzerland that produces European guidelines for concrete structures. Many of the guidelines set by FIB have been adopted in the Eurocode. FIB sponsors task group 9.3 to examine applications of FRP Reinforcement for Concrete Structures. Similar to

the standard design approach described in other guidelines, the rule of mixtures is described in this document.

However, another procedure is also accepted within this document, where an FRP is designed based on the properties of the bare fiber alone. Here, the nominal width of the fiber mesh is used, along with the modulus and ultimate strength values of the fibers factored by a reduction value (r) to account for the matrix properties. This value is simply the empirically derived relation between the bare fiber properties and those of the composite, as shown in the equation $t_{fib}E_{fib}r = t_{frp}E_{frp}$, where t_{fib} and E_{fib} are the thickness and Young's modulus of the bare fibers, and t_{frp} and E_{frp} are the thickness and Young's modulus of the composite, respectively (FIB Bulletin 14, 2001). This simplified design approach has not been adopted by any other guides or codes.

(3) FRP REPAIR SYSTEMS

Within this study damaged steel and aluminum poles are repaired with various externally-bonded FRP systems. An FRP repair system consists of a reinforcing fiber type (or types), a matrix material, and an adhesive or filler material. The steel or aluminum that comprises the pole is referred to as the substrate material.

3.1 Fiber Selection

There are many fiber types available for infrastructure repair. Currently the most common types used for structural applications are carbon and E- or S-glass fibers. Aramid and basalt fibers have also been shown to have properties suitable for structural applications. Some typical values for the mechanical properties of these fiber types are shown in Table 1.

Table 1. Typical tensile properties of fibers used in FRP systems (Rizkalla & Busel, 2002)

Fiber Type	Elastic Modulus		Ultimate Strength		Rupture Strain (%)
	10^3 ksi	(GPa)	ksi	(MPa)	
General Carbon	32 to 34	(220 to 240)	300 to 500	(2050 to 3790)	1.2
E-Glass	10 to 10.5	(69 to 72)	270 to 390	(1860 to 2680)	4.5
S-Glass	12.5 to 13	(86 to 90)	500 to 700	(3440 to 4140)	5.4
General Aramid	10 to 12	(69 to 83)	500 to 600	(3440 to 4140)	2.5
General Basalt	-	(90 to 95) [a]	-	(2900 to 3200) [a]	-

[a] Indicates a value taken from manufacturer specifications (Kamenny Vek)

Carbon fibers are generally considered the strongest fibers available on the market today; however, as previously stated, carbon has the potential to cause galvanic corrosion when placed in contact with other reactive materials such as steel or aluminum. To prevent galvanic interaction, contact between the CFRP and substrate should be prevented. To

achieve this, a layer of glass fiber was used to insulate the carbon from the substrata for the tests described in the following chapter.

Aramid fibers have a similar drawback. Aramid is known to be susceptible to degradation when exposed to ultraviolet light. This makes it less than ideal for placement on utility poles that will be continuously exposed to direct sunlight. For this reason, aramid fibers were not investigated within this study.

3.2 System Selection

Many private companies produce FRP systems designed for use as externally-bonded reinforcement. However, few of these products are designed specifically to adhere to metallic substrates, and even fewer are intended for repair of impact-damaged metallic utility poles.

Initially, two FRP systems were examined for effectiveness. One was a GFRP system produced by Fyfe Co. using Tyfo® resin, while the other used Sikadur® epoxy and a Hexcel carbon fiber weave. Both of these were paired with a filler material sold by 3M. The properties of these commercial systems were then compared to a different set of FRP repair systems produced by matching bi-directional woven fiber sheets with other commercially available matrix material and structural adhesives.

To simplify the installation process, these bi-directional fiber sheets use a balanced weave (one with equal fiber reinforcement in two orthogonal directions). Additionally, two weave densities were examined for each of the bi-directional fibers. The fibers selected are described in Table 2. For simplicity, two-letter abbreviations are used when referring to weave styles and are shown parenthetically next to each styles listing in Table 2.

Table 2. Reinforcing fabric weave densities

Fiber Type	High-Density Weaves			Low-Density Weaves		
	($^{oz}/_{yd^2}$)	Weave Style		($^{oz}/_{yd^2}$)	Weave Style	
Unidirectional Glass Weave	27	Unidirectional Sheet	(UG)		- -	
Unidirectional Carbon Weave	15	Unidirectional Sheet	(UC)		- -	
Bi-Directional Basalt Weave	24	Balanced Plain Weave	(BH)	11	Balanced Plain Weave	(BL)
Bi-Directional Glass Weave	24	Balanced Plain Weave	(GH)	11	Balanced Woven Tape	(GL)
Bi-Directional Carbon Weave	12	Balanced Plain Weave	(CH)	6	Balanced Plain Weave	(CL)

3.2.1 Fiber Orientation

The Tyfo® and Sikadur® resins were used with unidirectional fiber weaves. This produces a product with very high tensile strength and stiffness in the longitudinal fiber direction, but much lower capacity in the transverse direction (see Figure 8). To reinforce both the axial and circumferential directions of the structure, multiple layers with varying fiber orientation were used. Conversely, repair system using a balanced bi-directional fiber weave produces uniform reinforcement in both the axial and circumferential directions within a single layer (see Figure 9).

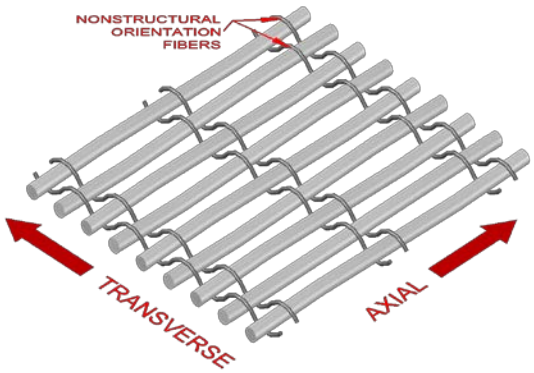

Figure 8. Unidirectional fiber weave

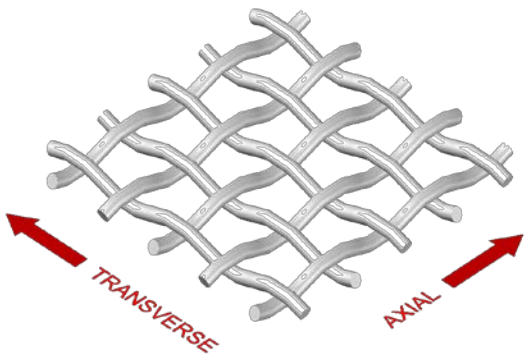

Figure 9. Bi-directional fiber weave

3.2.2 Matrix Properties

The Tyfo® and Sikadur® repair systems use structural epoxy (EP) saturating resins to impregnate the fibers. One polyurethane (PU) and two other EP resins were selected for pairing with the bi-directional fibers listed previously. The first of these epoxy resins is QuakeBond™J300SR Saturating Resin produced by QuakeWrap Inc. The second epoxy resin is CarbonBond™300, an epoxy produced by CarbonWrap Solutions LLC. The PU resin is a pre-impregnated product called "XT" that is produced by Neptune Research Inc.

The three saturating systems produced by QuakeWrap Inc., CarbonWrap Solutions LLC., and Neptune Research Inc. come pared with structural adhesives used to bond the impregnated FRP sheets to the substrate. These adhesives are QuakeBond™J201TC, CarbonBond™200P, and Syntho-SubseaLV and are matched with resins from QuakeWrap Inc., CarbonWrap Solutions LLC, and Neptune Research Inc., respectively. The Fyfe and Sikadur systems were not paired with separate adhesives.

The manufacturer properties for all of these resins are provided in Table 3. Values based on observations during application were used whenever a specific property was not provided by the manufacturer. For simplicity, two-letter abbreviations are used when referring to several of the systems. These abbreviations are shown parenthetically next to the resin designation in Table 3.

Table 3. Manufacturer specifications for saturating resins and adhesives

Resin Designation	Resin Type	Pot Life	Cure Time	Viscosity (cps)
Tyfo® SEH-51	2-part **EP** saturating resin	6-7 hrs	14-16 hrs	600-700
3M Bondo® Ultimate	**EP** automotive filler paste	-	1-3 hrs [a]	156 $_{x10^3}$
Sikadur® 330 US	2-part **EP** saturating resin	57 min	4-5 hrs	500
QuakeBond™ J300SR **(QB)**	2-part **EP** saturating resin	3-4 hrs	48 hrs	1500-1600
QuakeBond™ J201TC	2-part **EP** structural adhesive	90 min	48 hrs	"high tack"
CarbonBond™ 300 **(CB)**	2-part **EP** saturating resin	60 min [a]	2-4 hrs [a]	-
CarbonBond™ 200P	2-part **EP** structural adhesive	-	6-8 hrs [a]	"high tack"
NRi " XT " **(XT)**	H_2O-activated **PU** prepreg resin	30 min	2 hrs	-
Syntho-SubseaLV	2-part **EP** structural adhesive	-	6-8 hrs [a]	"high tack"

[a] Indicates a value based on observations, not supplied by manufacturer

(4) EXPERIMENTAL TESTING

To determine the failure modes present when dealing with reinforced metallic poles, a series of tests were conducted at the Florida Department of Transportation (FDOT) Marcus H. Ansley Structures Research Center in Tallahassee, FL. These tests used both steel and aluminum poles reinforced with the Tyfo® and Sikadur® reinforcing systems described previously. An inventory of the sections used is given in Table 4. With the exception of the first steel pipe section, all of the sections used were obtained from field use. The steel poles sections taper at a slope of $0.014\ \frac{\text{in}-\emptyset}{\text{ft}-\text{length}}\left(1.07\frac{\text{mm}-\emptyset}{\text{m}-\text{length}}\right)$, and the aluminum pole sections taper at a slope of $0.064\ \frac{\text{in}-\emptyset}{\text{ft}-\text{length}}\left(5.33\frac{\text{mm}-\emptyset}{\text{m}-\text{length}}\right)$ from the base.

Table 4. Inventory of test section

Designation	Original Length	Base Diameter	Wall Thickness	Testing Configuration	Fiber Orientation
PIPE	8’ – 0.0”	5.000”	0.125”	3-Point Loading	G0/G0/G90
S1	25’ – 0.0”	9.375”	0.250”	4-Point Loading	G0/C0/G90 C0/C0/G90
S2	34’ – 0.0”	10.00”	0.250”	3-Point Loading	G0/C0/C90
S3	24’ – 10.5”	13.00”	0.250”	3-Point Loading	G0/C0/C90
A1	27’ – 0.0”	8.000”	0.188”	3-Point Loading	G0/C0/C90
S4	17’ – 0.0”	15.50”	0.250”	Cantilever Loading	G0/G90/C0/C90/ C0/C90/C0/C90
A2	17’ – 0.0”	8.000”	0.188”	Cantilever Loading	G0/C0/C90 C0/C90

0 indicate axial fiber orientations, **90** indicate transverse fiber orientations,
G indicates a glass fiber layer, **C** indicates a carbon fiber layer

The configuration and results are presented for each test in this chapter. Results are presented in terms of moment capacity versus demand, load-displacement, and load-strain for each of the poles individually. Due to the various testing configurations, all of the moment

plots were normalized by converting the applied load to a ratio of the moment demand induced to the moment capacity (defined in terms of material yield) at that same location.

4.1 Application of Load

During normal field conditions, the largest forces acting on a utility pole are caused by lateral wind loads. This produces a distributed load acting along the length of the pole. Therefore, the structure acts as a vertical cantilever to resist the wind forces (see Figure 10). To achieve a similar bending stress resultant within the structure, several simulated load configurations are possible, including 3-point, 4-point, and cantilever configurations. Diagrams showing the flexural stress resultants of these loadings, as well as the moment distribution normalized by the moment capacity (defined in terms of material yield) are given in Figure 10 through Figure 13.

For large-scale testing it is easier to implement the three-point and four-point configurations. However, the relevant loading area (region of the pole where the bending stress most closely resembles the wind load case) is shifted away from the base for these configurations. For the most accurate resultant stresses near the base of the pole, a cantilever loading configuration is preferred.

The first two tests described in this chapter (involving the Pipe and S1 sections) used three-point and four-point loading configurations. These were intended to examine the response of undamaged and moderately damaged structures. The next three tests (sections S2, S3, and A1) used a modified three-point loading configuration in an attempt to shift the relevant loading area toward the base. The result of these three tests (though somewhat unintentional) demonstrated the failure modes associated with under-reinforced poles. The

final two tests (sections S4 and A2) used a true cantilever configuration and involved a damage condition and location that most closely resembled vehicle impact damage.

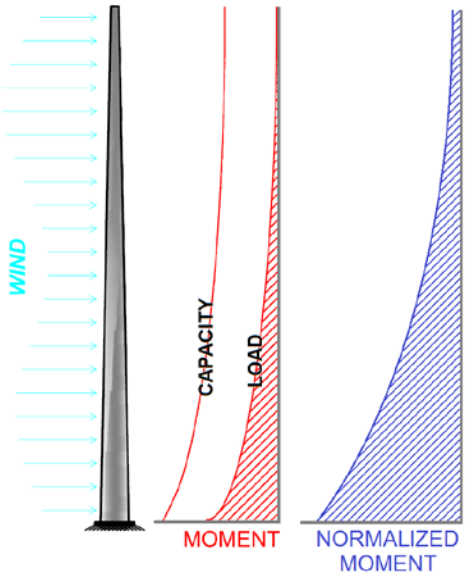

Figure 10. Wind induced bending stresses

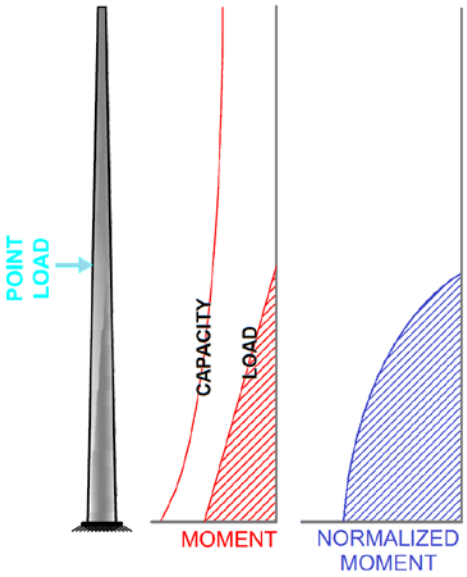

Figure 11. Cantilever induced bending stresses

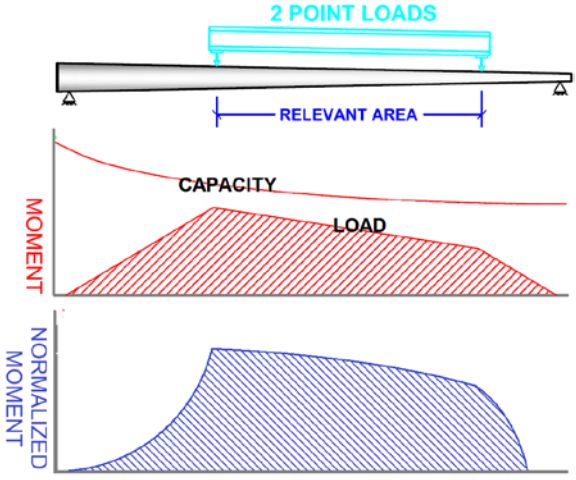

Figure 12. Four-point induced bending stresses

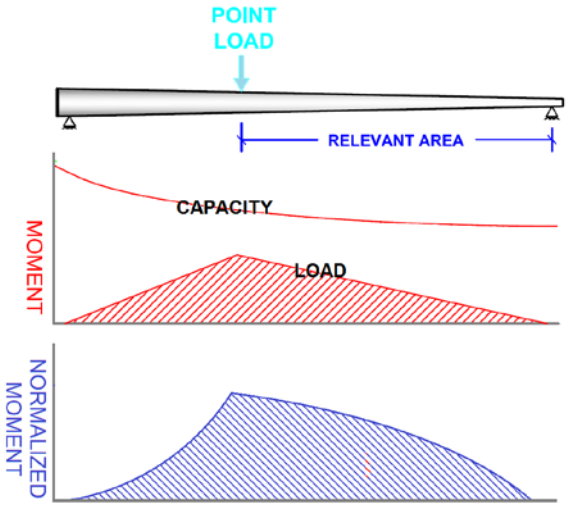

Figure 13. Three-point induced bending stresses

4.2 Three-Point Bending Test: Pipe Section

4.2.1 Testing Configuration

An 8ft (2.44m) steel pipe section with 5.0in (127mm) outer diameter and 0.125in (3.2mm) wall thickness was used as an initial concept test. This specimen was tested in a 3-point configuration. The span lengths between the supports was 7ft-9in (2.36m), and the load was applied at 3ft-8in (1.12m) from the East end, as shown in Figure 14. The pipe section was undamaged and a 20in (508mm) section was wrapped with three layers of the Tyfo® GFRP reinforcement system, as can be seen in Figure 16. The two inner FRP layers had an axial fiber orientation (0º), while the outer layer was oriented transversely (90º) as shown in Figure 15. The FRP was applied with the pipe section in a horizontal position, and allowed to cure in place before testing.

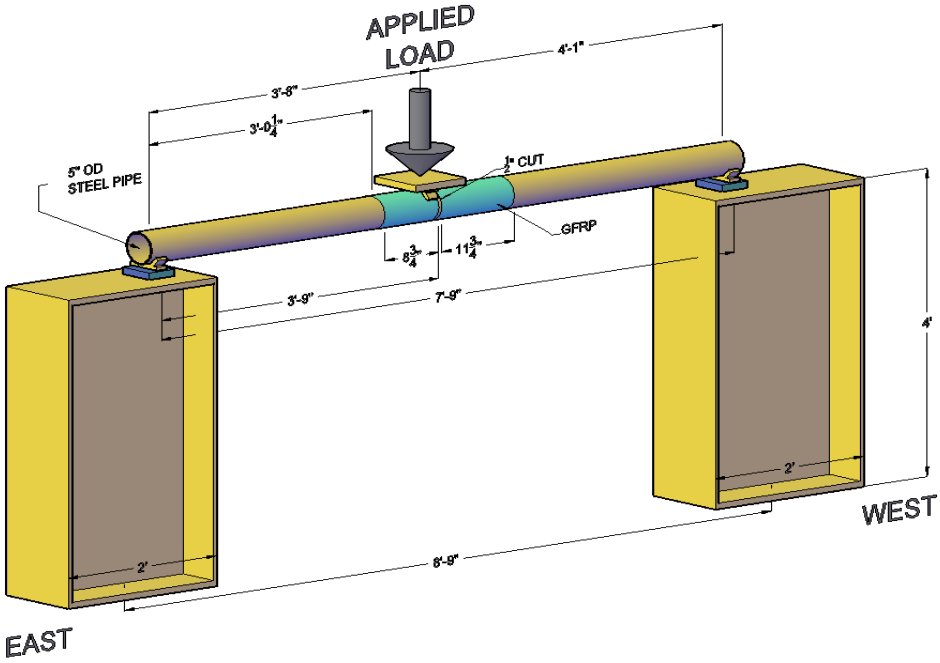

Figure 14. Three-point testing configuration for pipe section test

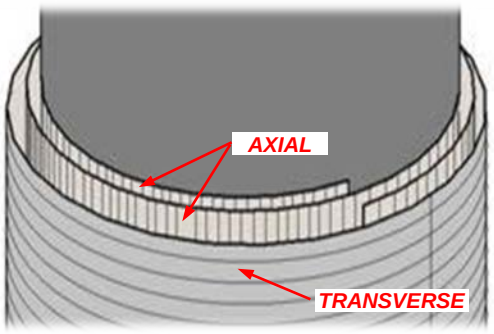

Figure 15. Pipe wrap orientation schematic

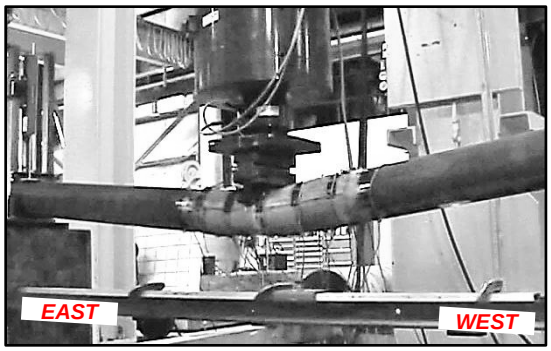

Figure 16. Pipe deformed shape under loading

Prior to testing, a 0.5in (12.7mm) cut was made through the FRP composite around the circumference of the pipe 3ft-9in (1.14m) from the East end. This produced two separate FRP-reinforced regions: a smaller region, where the load was applied, and a longer region to the West of the load that simulates the relevant portion of a pole (region where stress most closely resembles the wind load case). Curved saddle supports were fabricated to support the ends of the pole, but prevent rotation about the pole's axis and translation perpendicular to the pole's axis. The load was applied at approximately 0.1 $^{in}/_{min}$ (2.54$^{mm}/_{min}$) with an Enerpac 120kip hydraulic actuator, and a similar saddle was connected to the actuator and used at the load point.

To monitor the structure during loading, 24 foil-backed uniaxial strain gauges were adhered to the outer layer of FRP and steel substrate. Seven of these gauges were applied to the top/compressive face, seven were applied opposite the first ones on the bottom/tension face, and ten were applied in the transverse direction at the midpoint of the pole vertically (five gauges on each side, North and South). Additionally, three laser displacement gauges were located beneath the pole to measure deflection, and an LVDT was set at each reaction point. The gauge setup and numbering is shown in Figure 17.

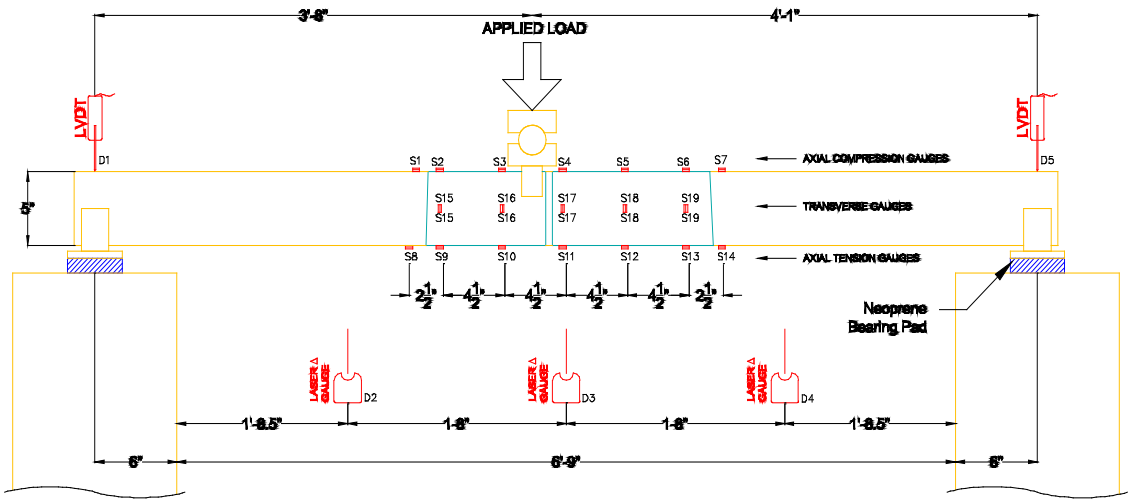

Figure 17. Gauge configuration, pipe section

4.2.2 Test Results

The normalized moment demand acting on the member is plotted with respect to the length of the section. As expected, the moment resisted by the undamaged pipe section exceeded the theoretical unreinforced capacity. Additionally, the displacements measured from D2, D3, and D4 along the length of the section are plotted against load in Figure 19, and the tension, compression, and transverse strain gauge readings are given in Figure 20, Figure 21, and Figure 22 respectively.

Yielding occurred in the substrate at approximately 118% of the theoretical capacity of the member (a load of 7.2kip or 32kN) and a plastic hinge formed at the cut between the two FRP sections. At this point the measured compressive strains began to reduce toward zero and the transverse strains began to quickly increase. These small compressive and large

transverse strains indicate that the circumferential fiber provide additional stiffness after the development of a plastic hinge.

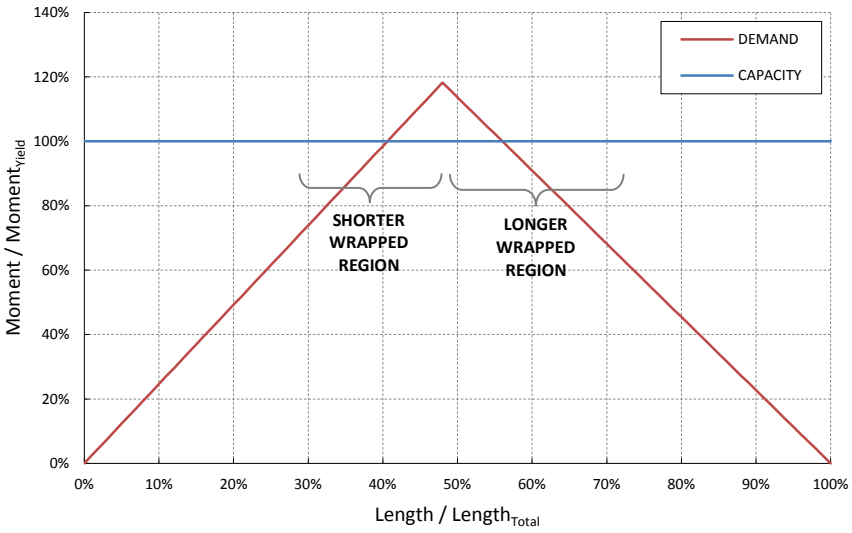

Figure 18. Normalized moment demand and capacity, pipe section

After the load reached 4 kips (18kN) debonding between the FRP and steel was observed, initiating on the tension face beneath the applied load and spreading circumferentially toward the compressive face and axially toward the reaction supports. The effects of debonding are visible in the tensile strain gauge S11, where the strains are consistently lower than surrounding gauges (Figure 20). Gauge S11 was located at the point of initial debonding.

Opposite S11 on the compressive face, gauge S4 strain values were also lower than surrounding gauges; however, this was primarily due to local deformations caused by the applied point load. These local deformations produced localized buckling of the pipe section that skewed the strain S4 readings from compression toward tension (Figure 21). Ultimately,

this section failed due to excessive deformations caused by yielding of the steel substrate within the cut between the two FRP reinforcing sections, and not within the FRP itself.

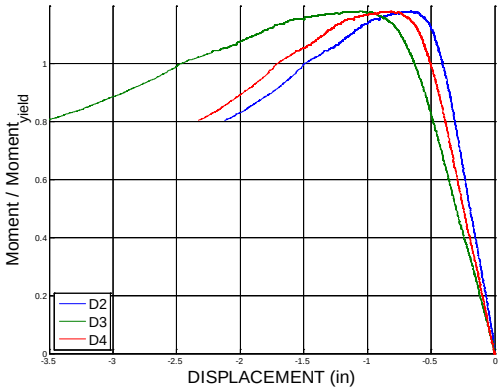

Figure 19. Displacement readings, pipe section

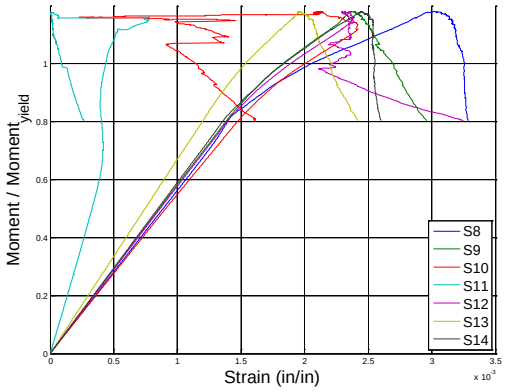

Figure 20. Tensile strain readings, pipe section

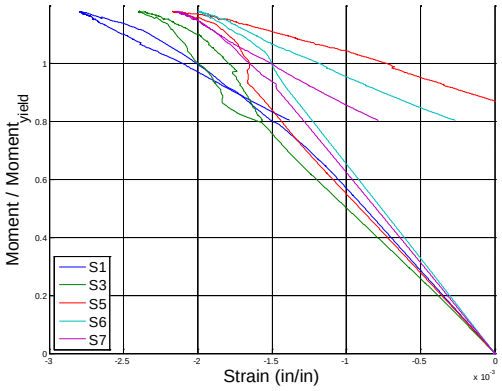

Figure 21. Compressive strain readings, pipe section

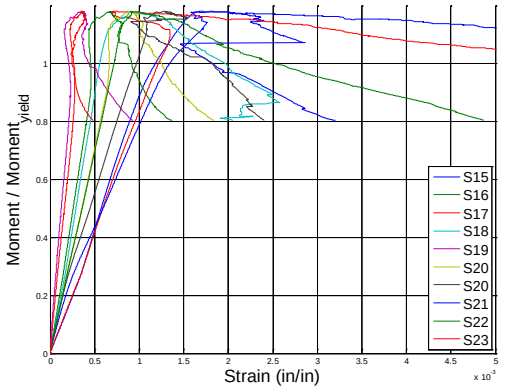

Figure 22. Transverse strain readings, pipe section

4.3 Four-Point Bending Test: Pole S1

4.3.1 Testing Configuration

This test involved a 25ft (7.6m) long steel pole that was artificially dented to $^{11}/_{16}$in (17.5mm) deep. This was the first test involving a damaged section, and was primarily used

as a feasibility test of the retrofit procedure. Therefore, along with the minimal dent depth, the FRP retrofit scheme was also selected to be overly conservative. Both the Sikadur® andTyfo® unidirectional carbon and glass fiber repair systems were used for reinforcement, with multiple layers of each fiber in both the axial (0º) and transverse (90º) orientations as described in Table 4. Like the pipe section, the FRP was applied horizontally, and permitted to cure in place before testing (see Figure 25).

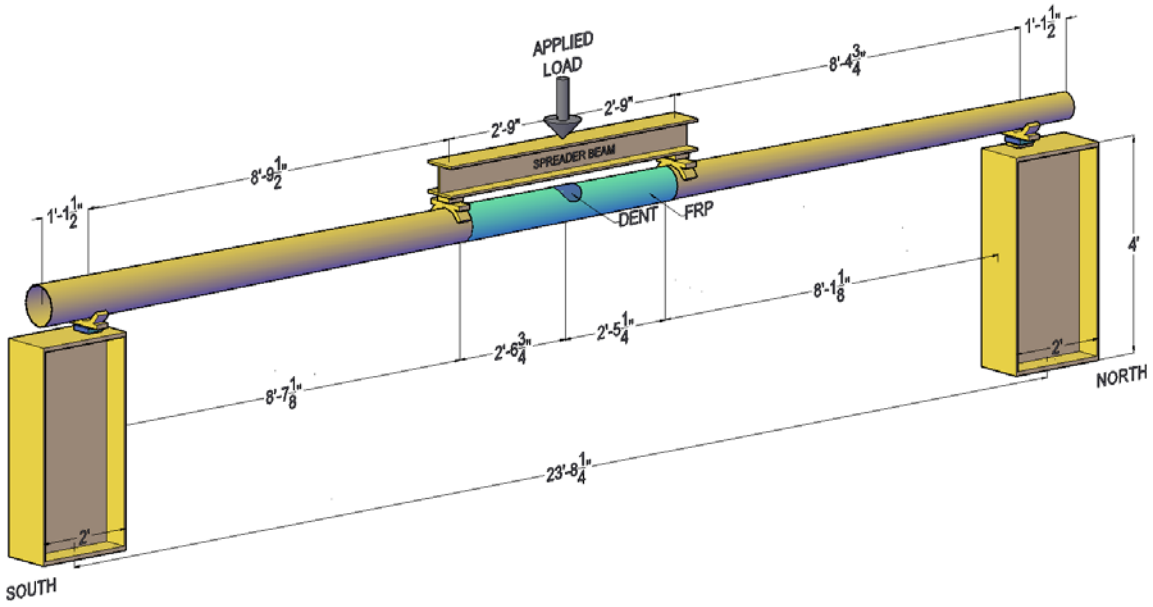

Figure 23. Four-point testing configuration

Figure 24. layup of inner CFRP layer, S1

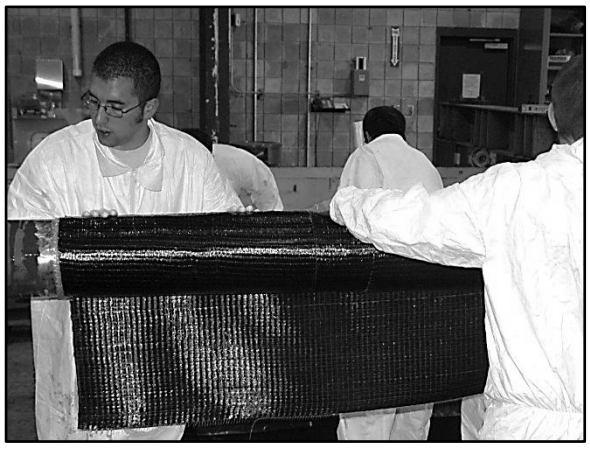

Figure 25. layup of outter CFRP layer, S1

Nine displacement transducers manufactured by TML were used to monitor the displacement of the bottom face of the pole with respect to a reference frame, and two additional LVDT displacement gauges were mounted at the centerline of the dent, one attached to each side of the pole (labeled midE and midW). The deflected shape of the section under loading can be seen in Figure 28.

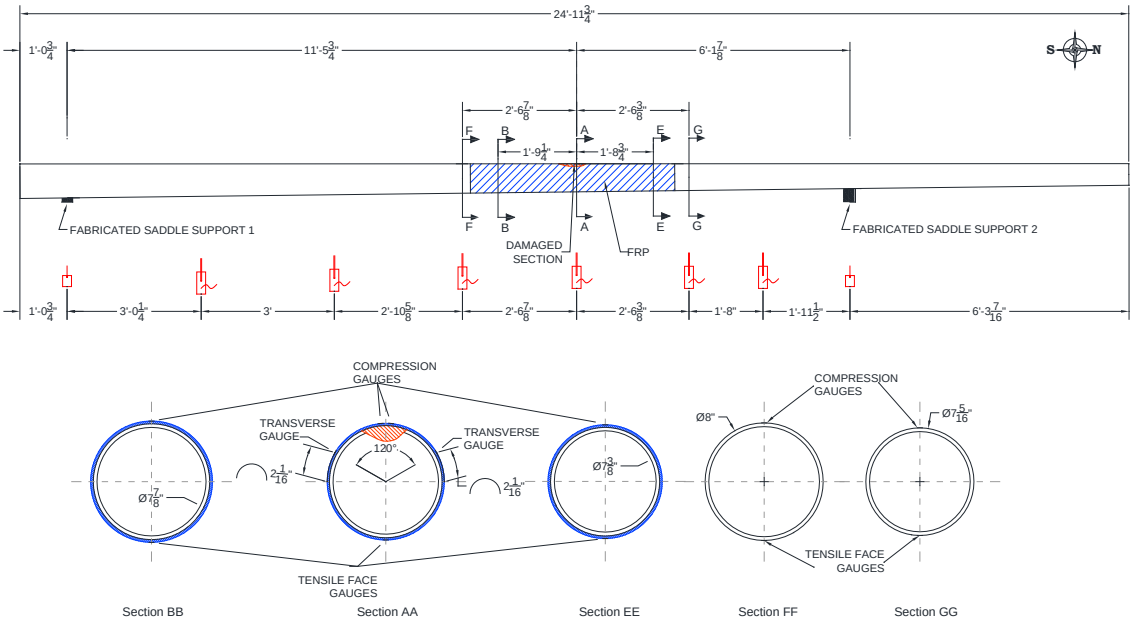

Figure 26. Four-point section gauge configuration, S1

Ten foil-backed uniaxial strain gauges were applied to the tension and compression faces of the pole at the five locations shown in Figure 26. These were adhered to the steel substrate (5mm 120Ω) immediately outside of the wrapped region, and to the top layer of CFRP (6mm 350Ω) at the left, center, and right of the wrapped region. In addition, two transversely oriented strain gauges were attached to the CFRP at 60º below vertical on either side of the dented region. The load was applied using the same Enerpac hydraulic actuator as with the previous test. Load control was used to ensure equal distribution of force to the two

load points separated by a W-section spreader beam. This testing configuration can be seen in Figure 23.

4.3.2 Test Results

Due to the overly conservative retrofit applied to section S1, the ultimate capacity of the pole within the dented region exceeded the theoretical capacity of the undamaged pole (Figure 29). As expected, a plastic hinge formed in the pole at the larger diameter end of the wrapped region. No debonding of the FRP on the tension face was observed, and only minor warping of the compressive FRP occurred.

The relationship between the applied load and the displacement measured at the left, middle (east and west), and right of the wrapped region is shown in Figure 30. The tension and compression strain gauge readings for both the FRP and the substrate are presented in Figure 31 and Figure 32 respectively, while the transverse readings are shown in Figure 33. Similar to the previous test, the dominant failure mode observed involved excessive deformations resulting from yielding of the steel substrate outside of the reinforced region.

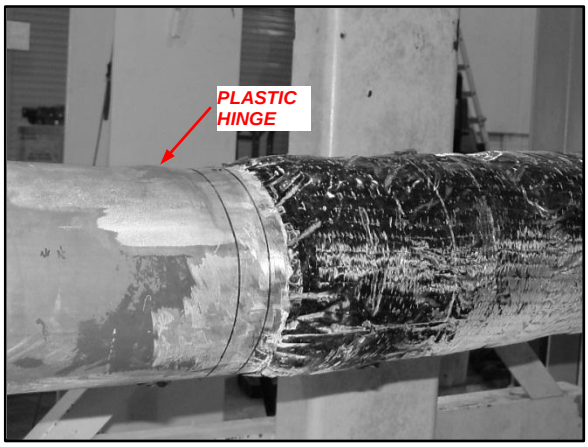

Figure 27. Deformed shape under loading, S1

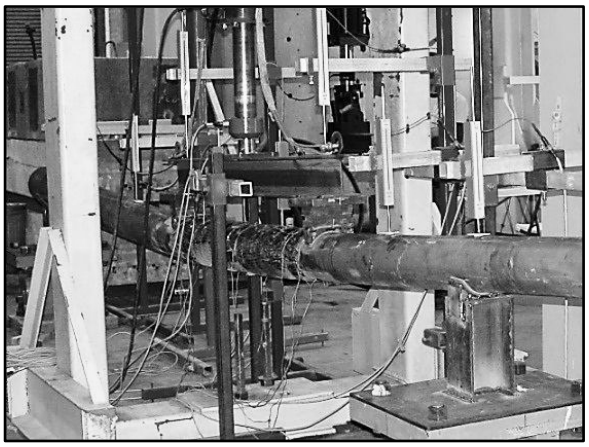

Figure 28. Deformed shape under loading, S1

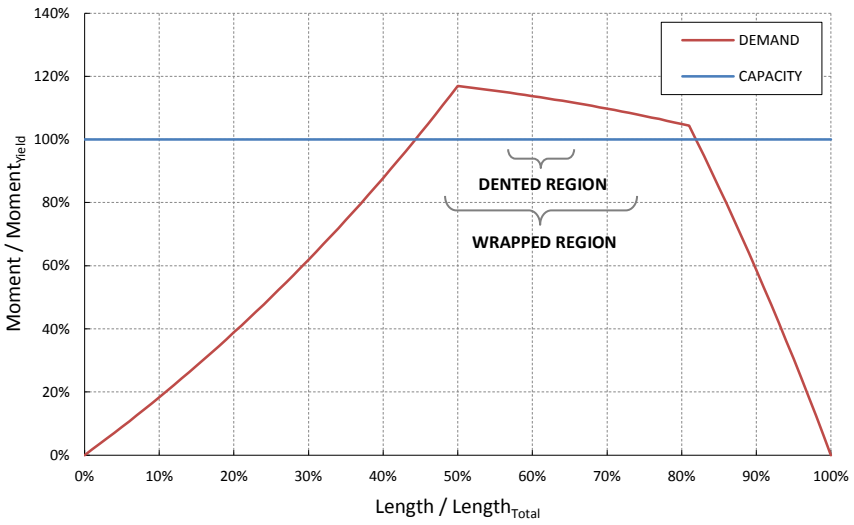

Figure 29. Normalized moment demand and capacity, S1

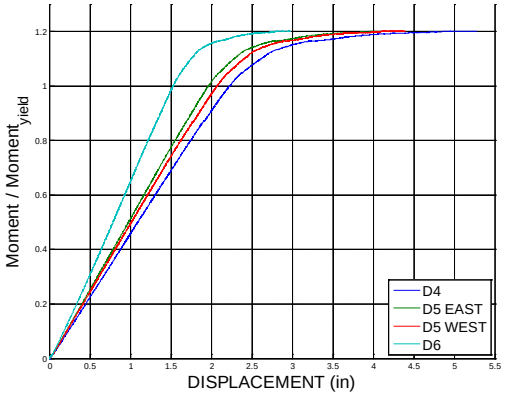

Figure 30. Displacement readings, S1

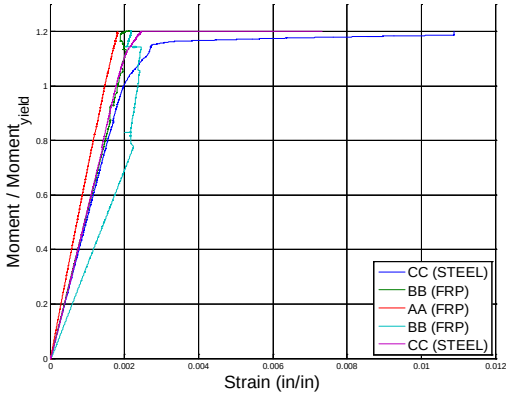

Figure 31. Tensile strain readings, S1

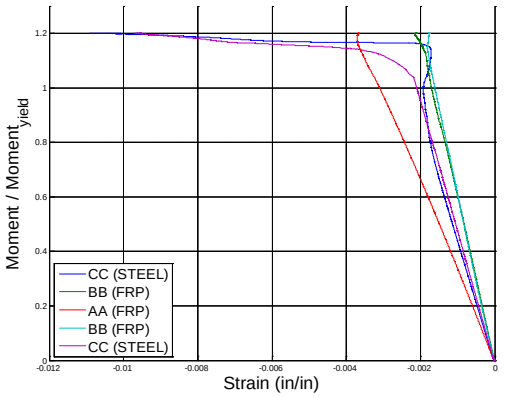

Figure 32. Compressive strain readings, S1

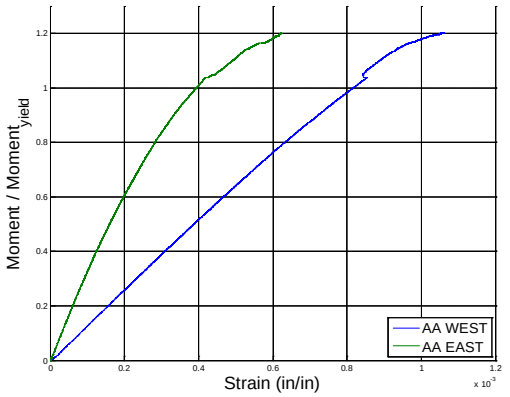

Figure 33. Transverse strain readings, S1

4.4 Modified Three-Point Bending Tests: Poles S2, S3, A1

Two tapered steel poles (S2, S3) and one tapered aluminum pole (A1) were tested in a modified 3-point bending configuration designed to mimic a cantilever loading on the pole section. This was accomplished by attaching an HP section to the base of each pole and applying a point load at the connection as shown in Figure 34.

4.4.1 Testing Configurations

A stiffened 1in (25mm) thick steel plate was welded to the end of an HP14x89 wide flange section by 3/8" fillet welds all around, and the baseplate of the S1 pole section was attached to this plate. For both poles S3 and A1, a 2in (51mm) thick plate was used instead. The clear span of the HP section was maintained at 13'-3 13/32" (4.05m) for each test, while the clear span of the poles varied as listed in Table 4.

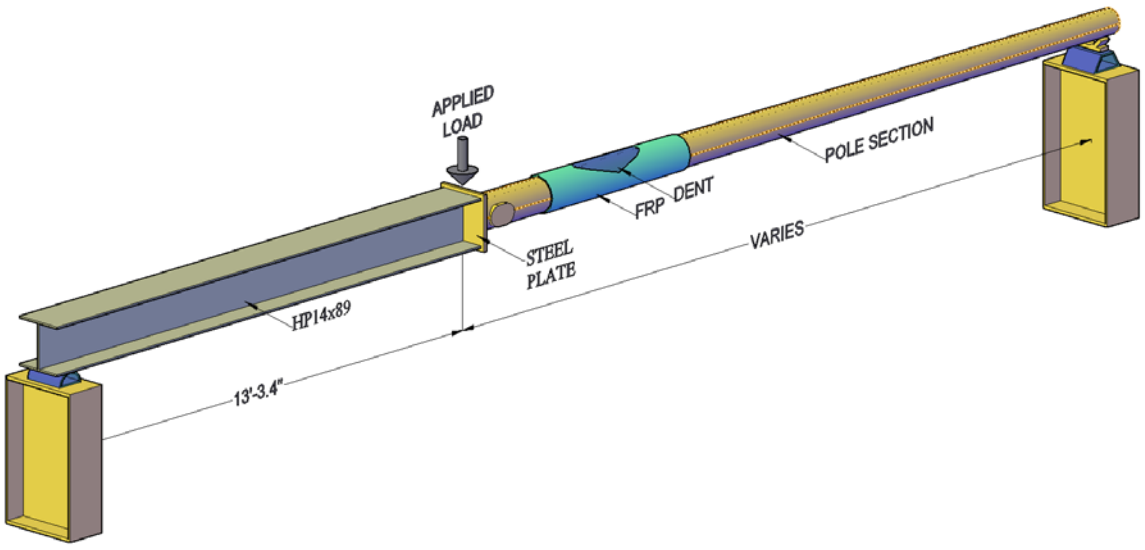

Figure 34. Modified three-point bending testing configuration

During testing, the load was applied directly to the steel plate using a pin joint at the interface of the pole and the HP section with the same Enerpac hydraulic actuator as with the previous tests. The self-weight of the HP section added to the demand acting on the pole. Therefore, the actuator generated demand and the total demand (including self-weight) are shown separately in the figures. The instrumentation plan for each of these poles was similar to S1, with five laser displacement gauges placed along the length of the pole in addition to the actuator displacement readings. Multiple strain gauges were also applied as shown in Figure 35 to monitor tensile, compressive, and transverse strains across the section.

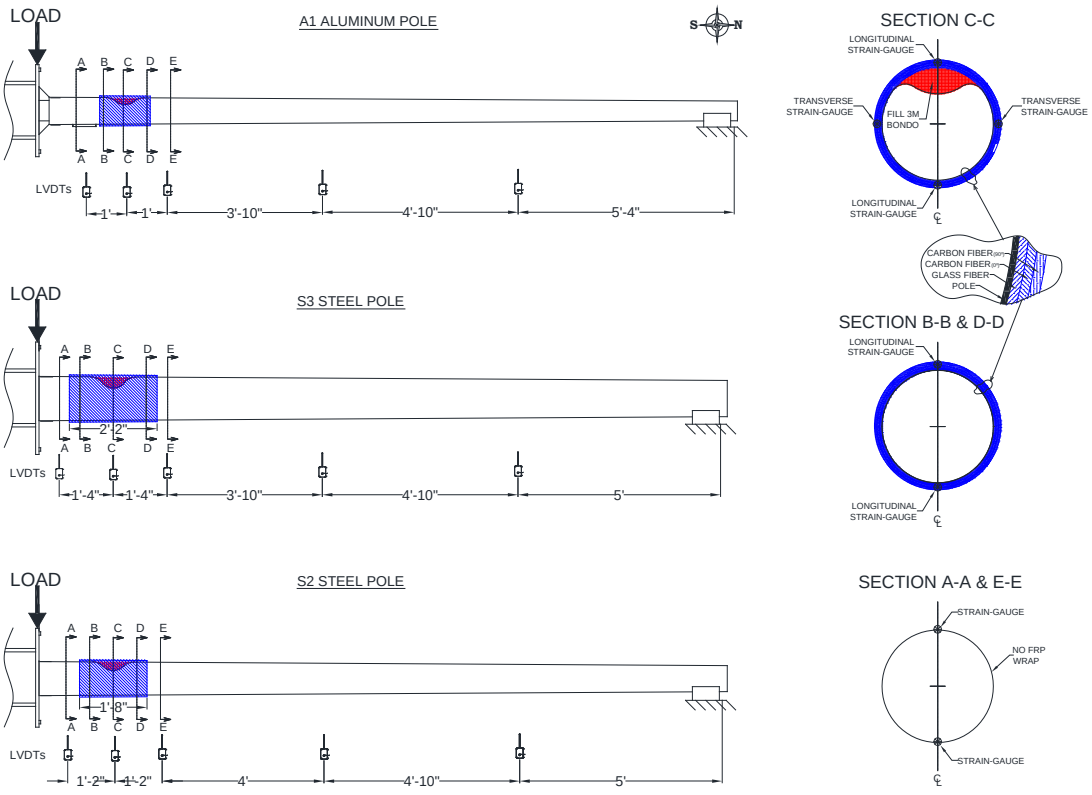

Figure 35. Sensor layout diagram for A1, S2, and S3 test specimens

The sections were each dented near the base of the poles to represent damage from vehicle collision. The dents were induced by a hydraulic actuator fitted with a reinforced steel cylinder centered at 22in (229mm) from the base plate (see Figure 36 and Figure 37). This distance was chosen because it represents the average height of a typical SUV bumper. Both the Sikadur® and Tyfo® repair systems were then used in the axial and transverse directions to repair the dented region. The orientation and fiber type of each composite layer are listed in Table 4.

Figure 36. Application of dent to S2

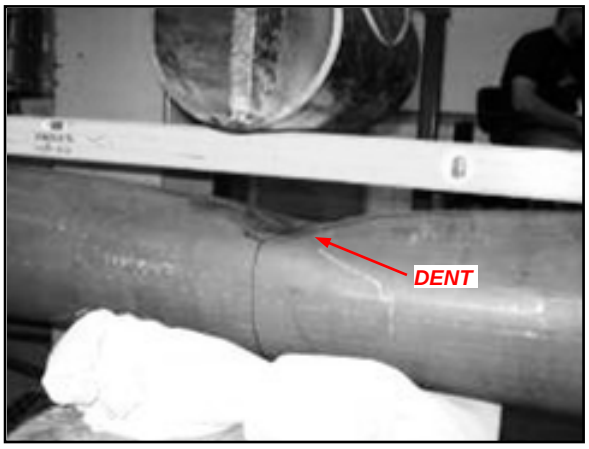

Figure 37. Extent of dent on S3

4.4.2 Pole S2 Results

Pole S2 was a tapered steel mast arm, similar to pole S1. However, S2 was dented to a depth of approximately 25% of the diameter of the section, 2.5in (64mm), and was repaired with a less conservative amount of FRP than pole S1. The dented region was filled with 3M Bondo® and the surface was prepared for better FRP adhesion by removing the topmost layer of galvanization from the steel with an angle grinder.

The deeper denting procedure produced a lateral distortion of the cross section at the centerline of the dent location, resulting in large plastic deformations in the steel at that location. Consequently, the extent of the dent axially along the pole, coupled with the kinematic rotation of the pole cross section at the centerline of the wrapped region, led to a different failure mechanism than observed during the testing of pole S1. The force-displacement response for the five displacement gauges and the actuator displacement are given in Figure 41 and the deformed shape is shown in Figure 38. The displacement presented is as measured.

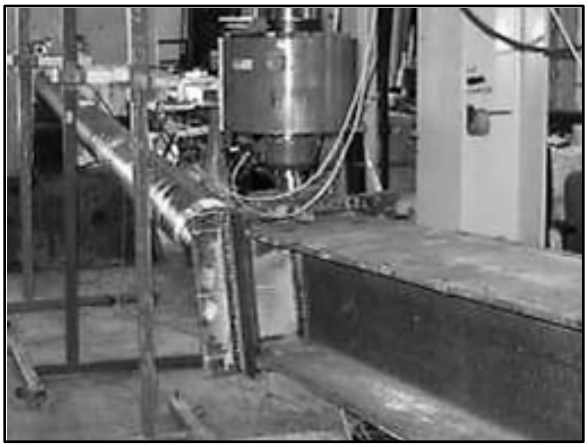

Figure 38. Deformed shape of S2

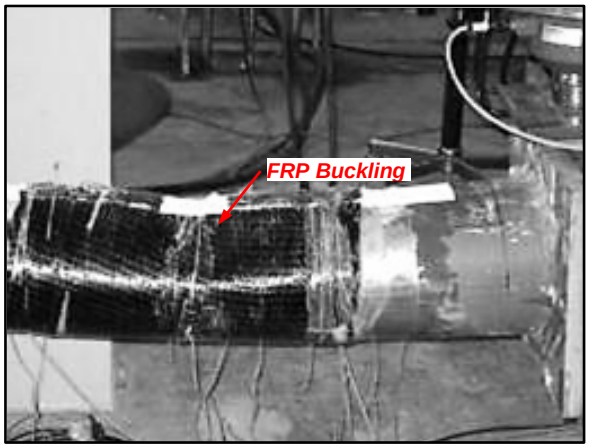

Figure 39. Failure of S2

As evident from the moment capacity versus demand plot (Figure 40), the theoretical capacity of the undamaged cross section was not achieved. However, from the strains measured on the FRP and steel, it is apparent that the steel yielded on the tension face of the pole (Figure 42). This suggests the capacity of the repaired section was diminished due to buckling of the fibers on the compressive face and subsequent movement of the neutral axis.

The first yielding of the system occurred at 85% of the theoretical capacity of the undamaged pole and was accompanied by a slight load drop at the instant when the compressive fibers first buckled. This phenomenon is clearly visible in Figure 43. The system regained some strength due to mobilization of the FRP on the tension face, but ultimately softening occurred due to the excessive rotation and corresponding folding of the FRP on the compression face (Figure 39). Also evident from the data is substantial engagement of the transverse layer of FRP (Figure 44). The transverse strains ultimately reached nearly 3000με due primarily to the initial distortion of the cross section during denting and subsequent expansion during flexure.

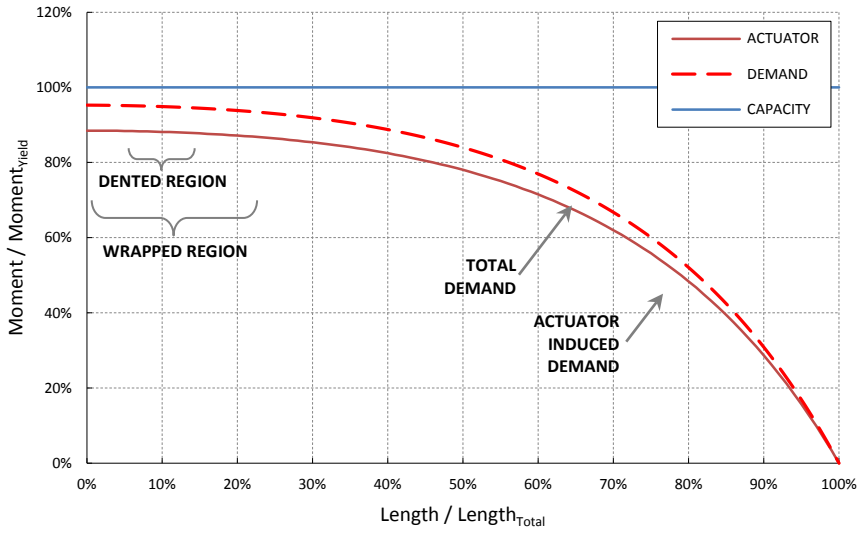

Figure 40. Normalized moment demand and capacity, S2

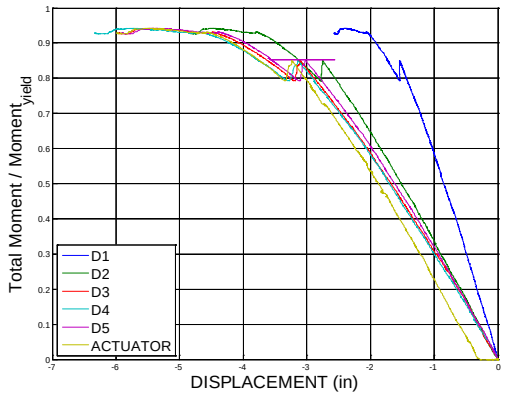

Figure 41. Displacement readings, S2

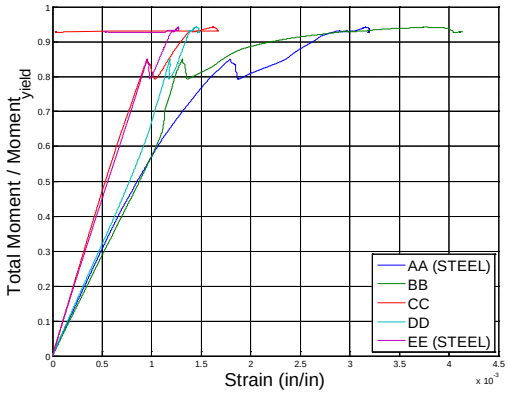

Figure 42. Tensile strain readings, S2

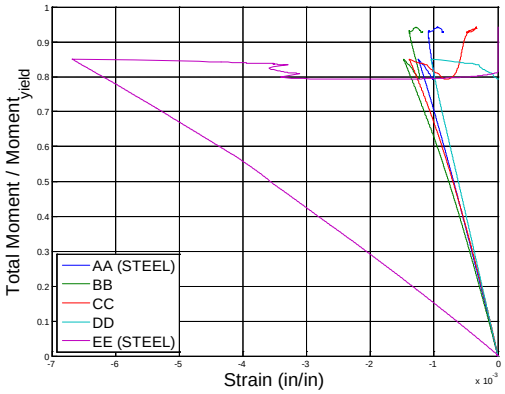

Figure 43. Compressive strain readings, S2

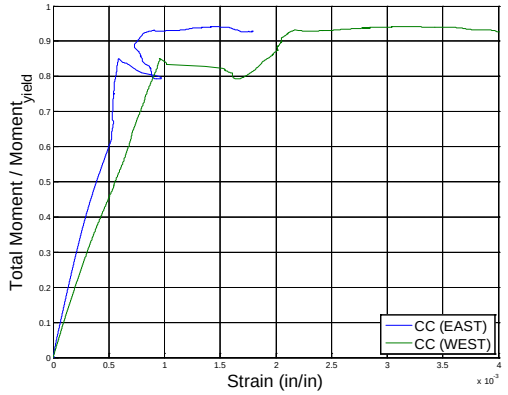

Figure 44. Transverse strain readings, S2

4.4.3 Pole S3 Results

Pole S3 was a tapered steel mast arm with a similar wrap scheme and testing configuration as pole S2. The base diameter of S3 was slightly larger than S2, so the dent depth was increased to 3.25in (83mm) to maintain a 25% dent ratio. As with S2, the dented region was filled with 3M Bondo® and the surface was cleaned and sanded with an angle grinder. The severity of the damage induced (spread of the dented region along the pole axis) was visibly greater in S3 than S2. A comparison of the extents of the two dents is given in Figure 47 and Figure 48.

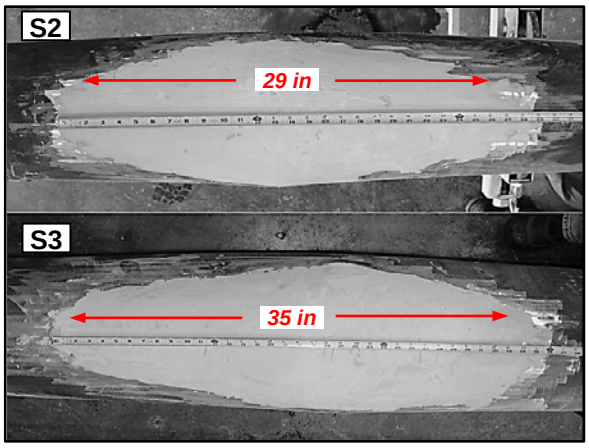

Figure 45. Axial damaged induced on S2 and S3

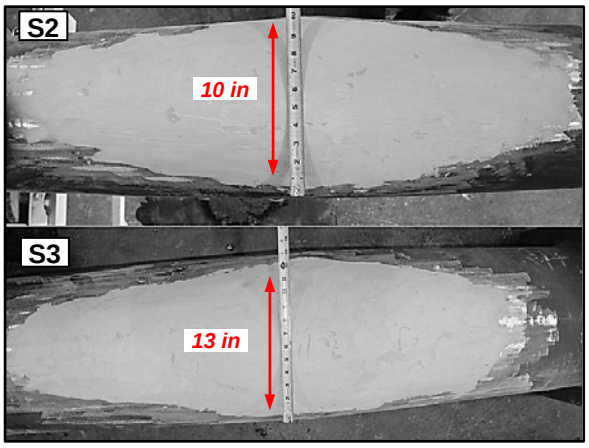

Figure 46. Lateral damaged induced on S2 and S3

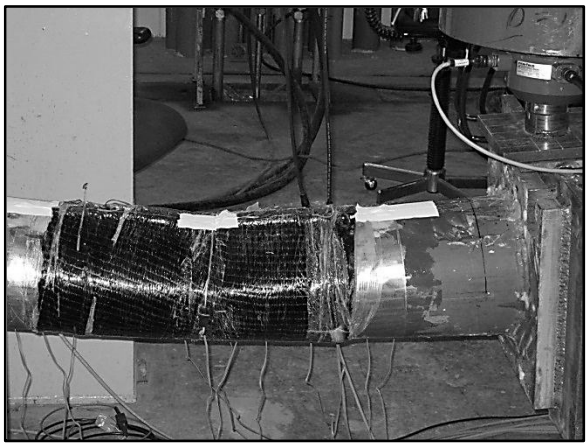

Figure 47. Failure of S3

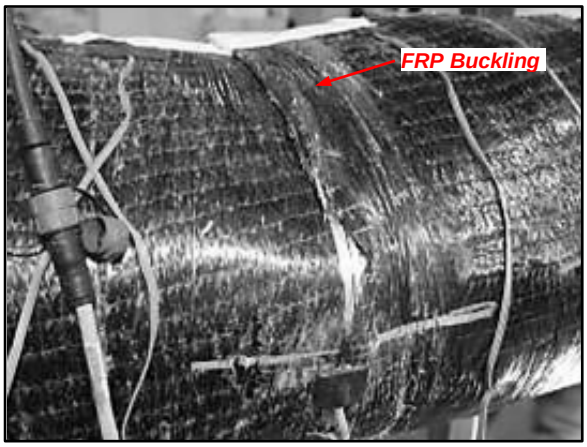

Figure 48. Compresive FRP on S3

During testing of S3 the ultimate load reached approximately 15.5 kip (69kN) after initial compressive fiber buckling, or approximately 93% of the theoretical capacity of the undamaged section. For pole S3, only a small amount of additional strength was mobilized beyond this point before softening occurred. The force-displacement and moment capacity versus demand for S3 are presented in Figure 48 and Figure 47, respectively. These indicate that S3 behaved similar to S2 (see Figure 53 and Figure 56) even though the severity of the damage induced was greater.

Additionally, the strain data shown in Figure 51 through Figure 53 helps to confirm that the capacity was diminished due to compressive fiber buckling and shifting of the neutral axis towards the tension face. As with S2, the tension steel yielded in the dented region. This indicates that, while the theoretical capacity was not reached, the pole had substantial capacity due to the repair. The transverse FRP strains further indicate that the distortion of the cross section for S3 was more severe than S2, and that the fibers within the transverse FRP layer were near rupture at the ultimate failure strains.

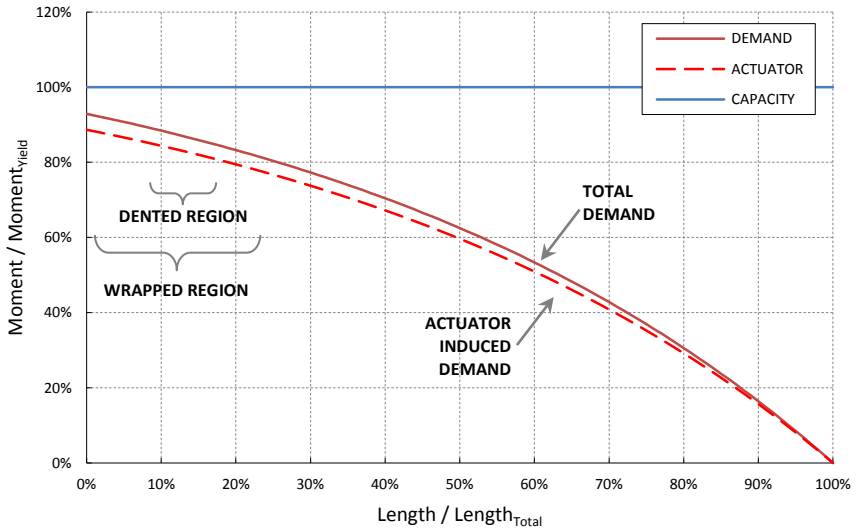

Figure 49. Normalized moment demand and capacity, S3

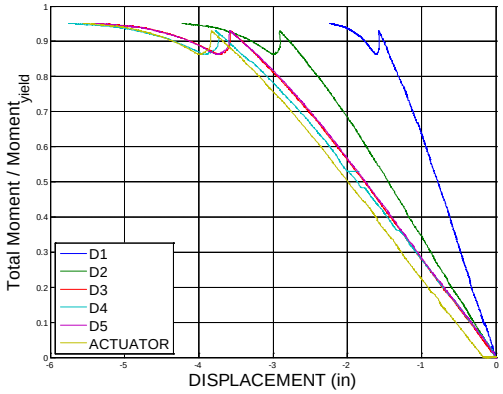

Figure 50. Displacement readings, S3

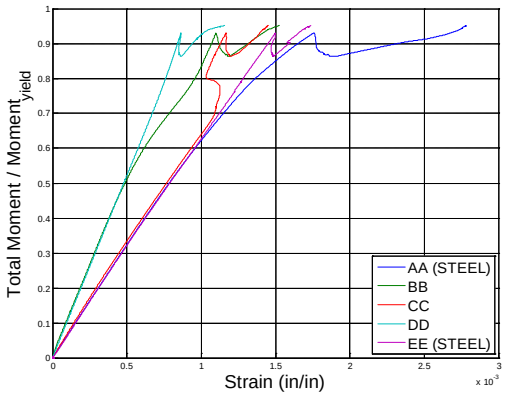

Figure 51. Tensile strain readings, S3

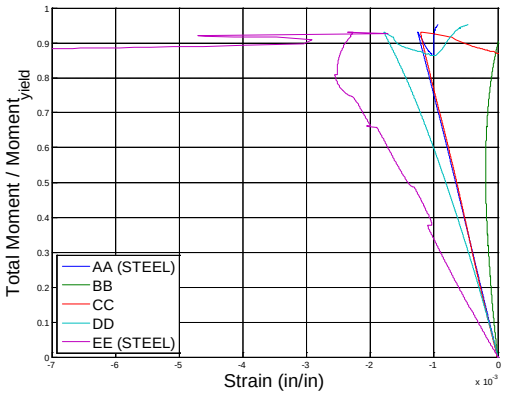

Figure 52. Compressive strain readings, S3

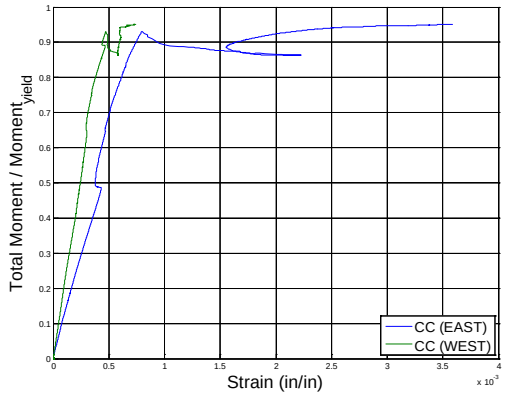

Figure 53. Transverse strain readings, S3

4.4.4 Pole A1 Results

This was the first attempt involving an aluminum pole. As with Poles S2 and S3, A1 was dented to a depth 0.25 times the diameter of the section (2in, or 51mm) resulting in a significant portion of the pole with reduced cross section. The wrap preparation and application were similar to S2 and S3.

A1 differed from the steel poles in the testing phase due to some problems encountered with the three-point setup. The weight of the larger HP14x89 wide flange

section that was attached to the base of A1 caused large displacements and strains (when released, before a measured load could be applied). Chains were then attached to the pole and a crane was used to support and lift the deflected portion of the setup back to a level position. The chains were then released and displacement and strain data was recorded. At this point the weight of the HP section caused the pole to deflect to its previous position without an increase in loading, shown in Figure 57. This is also visible in Figure 58 through Figure 59, where the initial strains are shown to increase without the addition of an applied load.

Additional load was then applied from the actuator, ultimately causing a crack to form in the aluminum and propagate through the access port (see Figure 54). Simultaneously FRP buckling occurred on the compressive face (see Figure 55). Therefore, little valuable data was gained from this test.

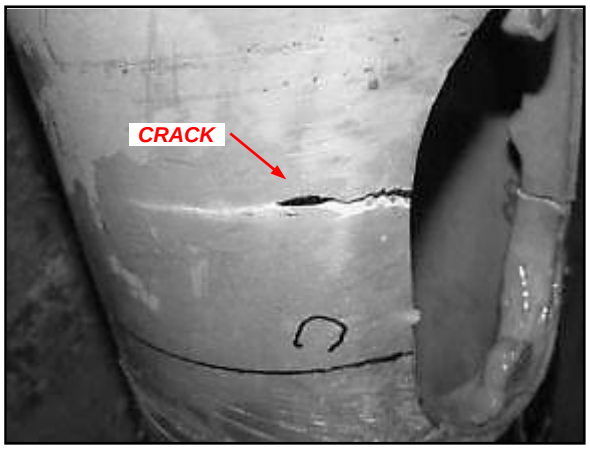

Figure 54. Cracking of aluminum in A1

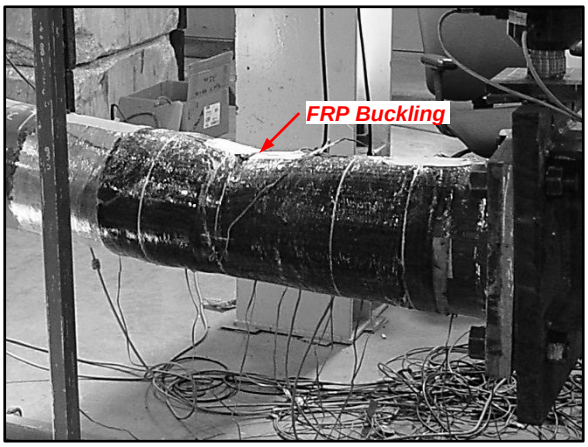

Figure 55. Failure of A1

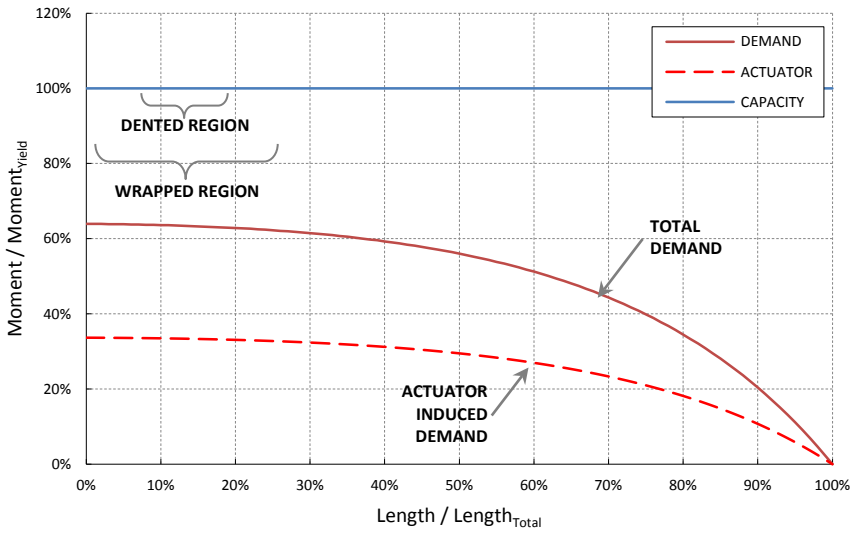

Figure 56. Normalized moment demand and capacity, A1

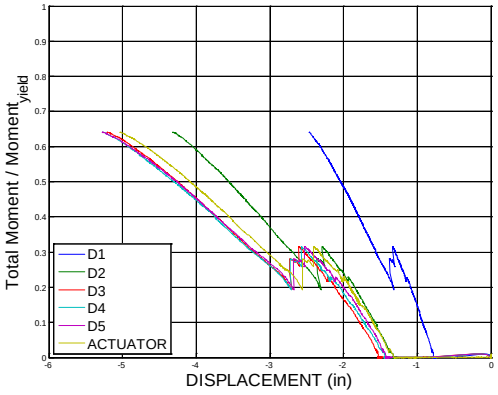

Figure 57. Displacement readings, A1

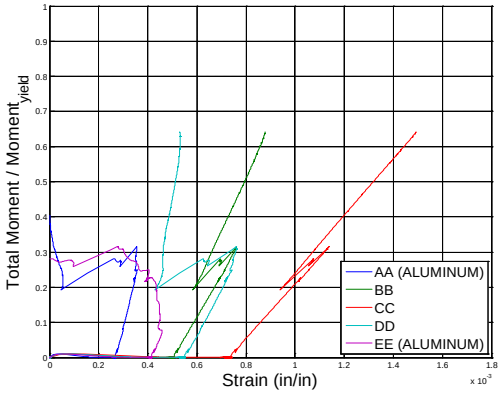

Figure 58. Tensile strain readings, A1

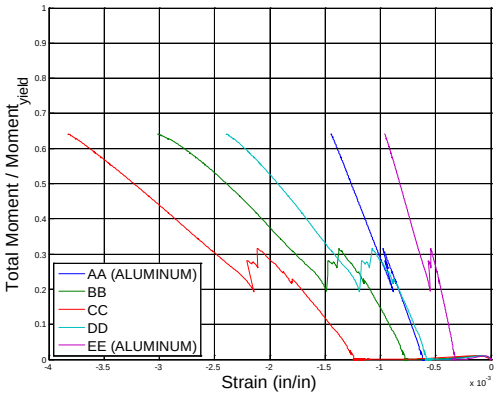

Figure 59. Compressive strain readings, A1

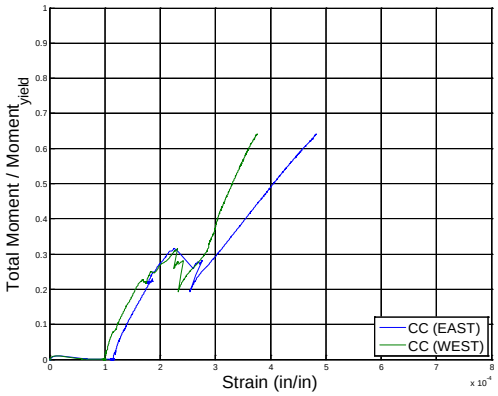

Figure 60. Transverse strain readings, A1

4.5 Cantilever Bending Tests: Poles S4 & A2

Two tapered poles, one steel (S4) and one aluminum (A2), were tested in a true cantilever bending configuration. As with the previous tests, these poles were dented near the base to simulate impact damage and then repaired with several layers of the Tyfo® and Sikadur® repair systems.

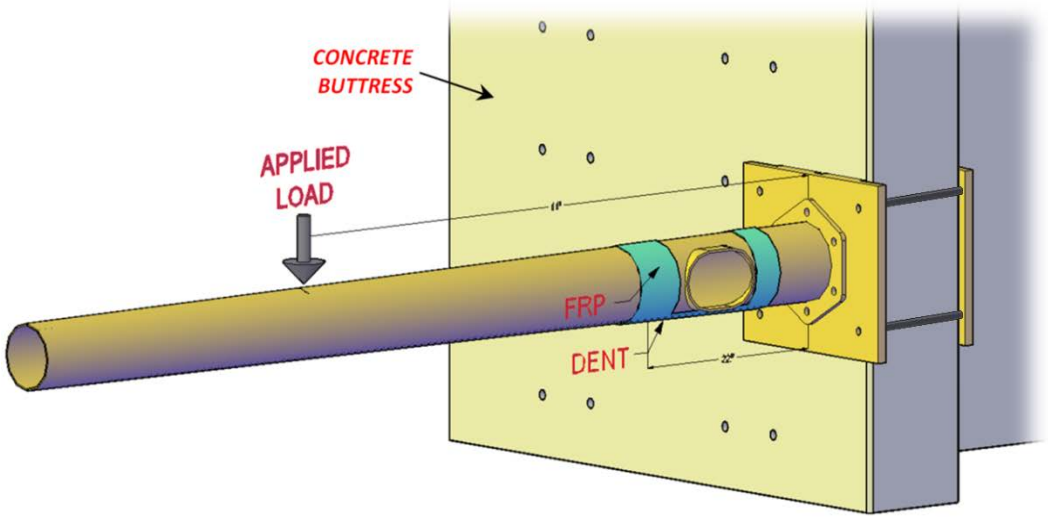

Figure 61. Cantilever testing configuration (pole S4 is shown)

4.5.1 Testing Configurations

The base plates of poles S4 and A2 were attached to a steel bearing plate, which was in turn anchored to a concrete buttress in a cantilever configuration as shown in Figure 61. The dented region was orientated toward the bottom of the pole, with a load applied vertically downward at a distance of approximately 11’ from the baseplate. Both poles had access ports located 90º to one side of the dented region. This posed a challenge for wrapping S4, because the location of the port coincided with a large portion of the dented section. The wrap scheme chosen to account for this is detailed in Figure 62 and Figure 63 and shown in Figure 67.

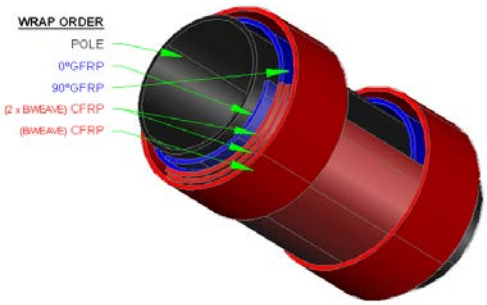

Figure 62. FRP wrapping schematic for S4

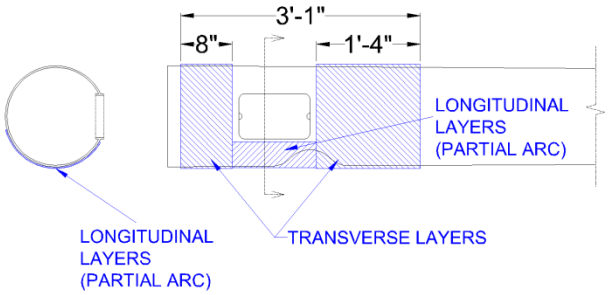

Figure 63. FRP wrapping diagram for S4

Three displacement gauges were placed along the length of the pole along with the actuator displacement. Additional LVDTs were placed on the baseplate to record slip and rotation at that point. Finally, multiple strain gauges were installed along the length of the wrapped region and just beyond, as shown in Figure 82.

Both poles S4 and A2 were dented to depths of approximately 20% the base diameter of the section. Additionally, the dents were applied with a displacement-controlled step-loading by a hydraulic actuator fitted with a hemispherical tip attachment (see Figure 64 and Figure 65). This resulted in plastic deformations that more closely represent those found in the field. The dent taper lengths achieved for S4 and A2 were approximately 25in (635mm) and 15in (381mm) of longitudinal spread, respectively. Three-dimensional point cloud scans were taken for these poles and are shown in the introduction, Figure 1 and Figure 2.

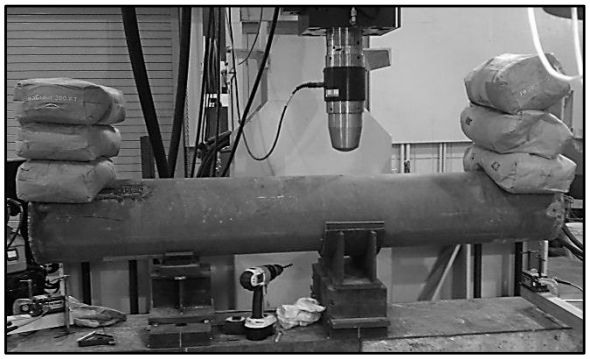

Figure 64. Denting test, before denting

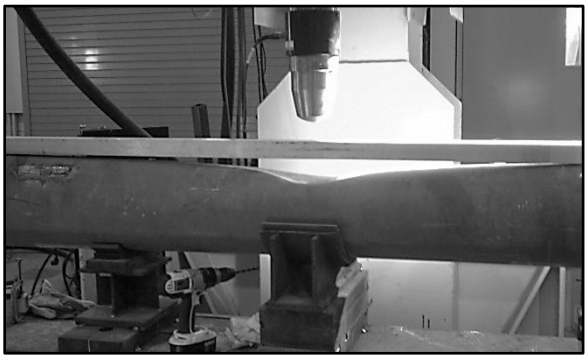

Figure 65. Denting test, after denting

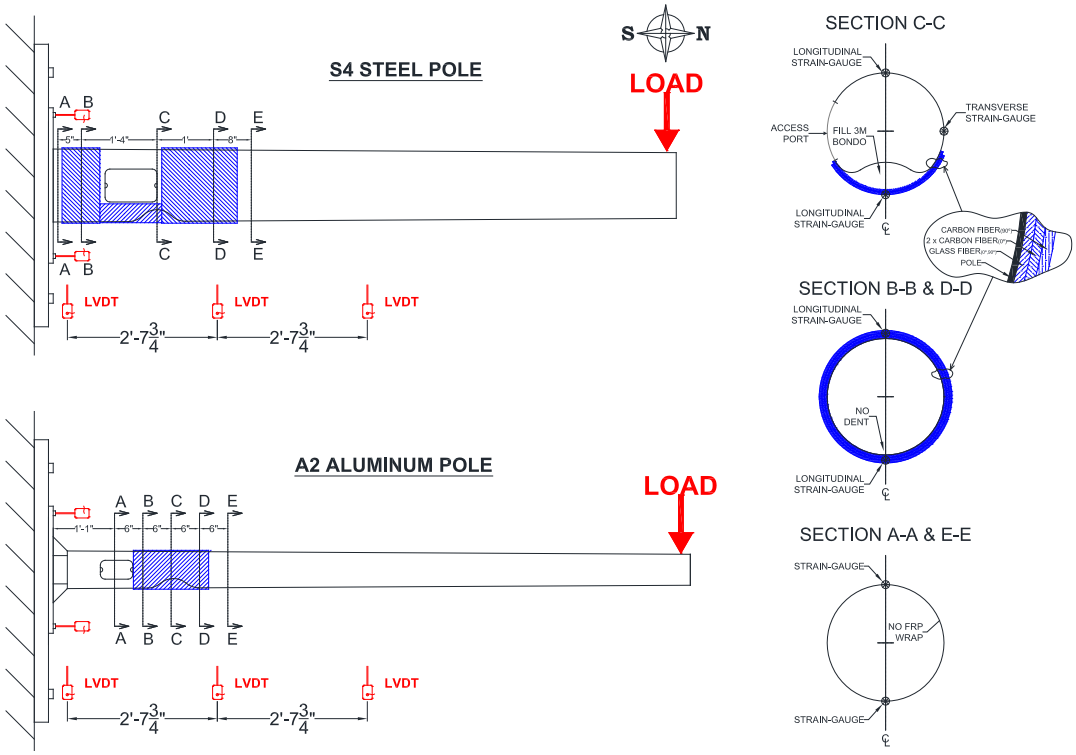

Figure 66. Sensor layout diagram for poles S4 and A2

4.5.2 Pole S4 Results

After denting, the region of reduced cross section was prepared as previously described. The force-displacement response for the three displacement gauges nearest the cantilever tip of S4 is shown in Figure 69. The displacements were adjusted to show the cantilever deflections, taking into account the displacement due to rotation in the bearing plate at the fixed end.

Based on the ultimate failure load, it can be seen in Figure 70 that for an undamaged pole subjected to this load, a plastic hinge is expected to form approximately 44in (1.1m) out from the fixed end of the pole. Actual hinging occurred at an observed “hump” that formed within the pole, beneath the FRP wrap, just past the deepest portion of the dent, shown in

Figure 67. This indicates improved moment capacity within the repaired region beyond that of an undamaged pole.

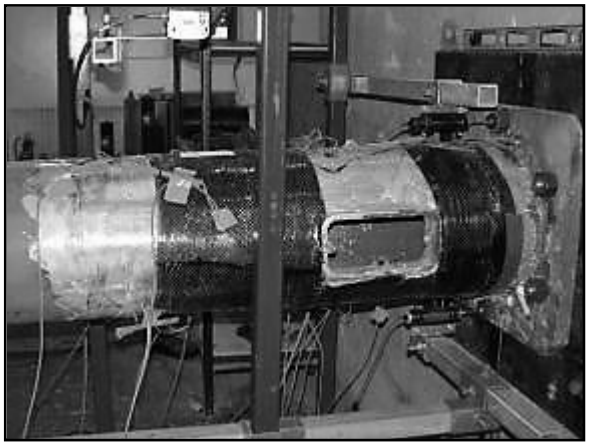

Figure 67. Wrapped portion of pole S4

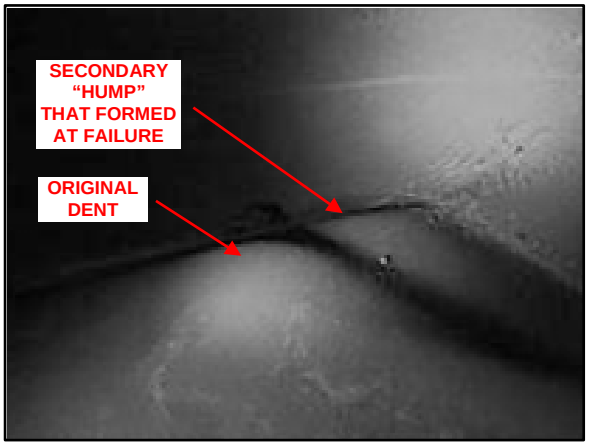

Figure 68. Local deformation within pole S4

Other failure modes were also observed. Debonding of the top, tensile layers of FRP opposite the dented portion of the pole was noted, along with minor buckling of the fibers on the bottom, compressive layers. The wrap was removed after failure and the 3M Bondo® was exposed and seen to have separated from the steel substrate and slightly crushed. As with the three-point tests, there was substantial engagement of the transverse FRP layers, indicating that the confinement helped to prevent lateral deformation of the pole within the plastic hinge, as well as restrict out-of-plane buckling of the compressive fibers. Therefore, the transverse fibers seem to plays a key role in returning the pole to its original capacity and stiffness.

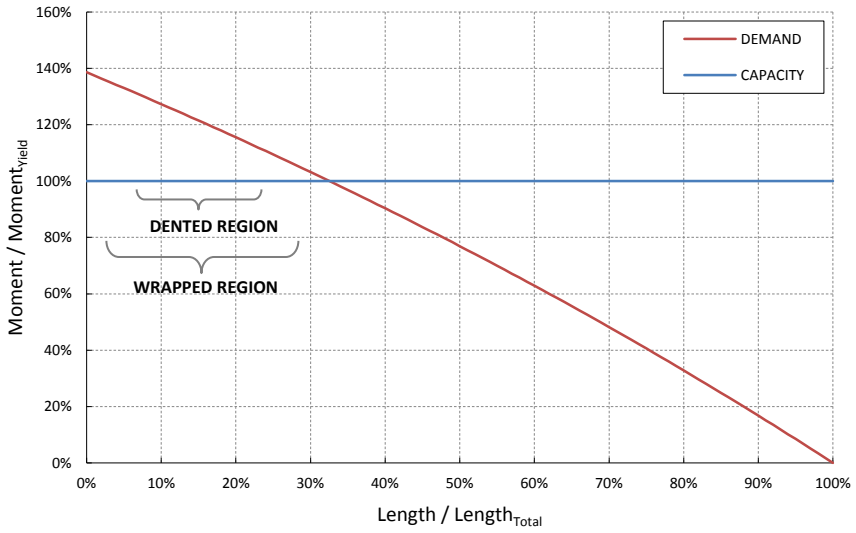

Figure 69. Normalized moment demand and capacity, S4

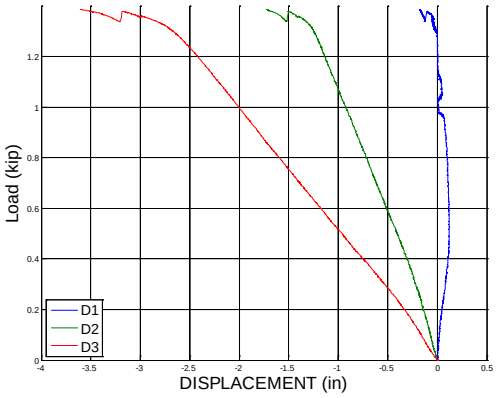

Figure 70. Displacement readings, S4

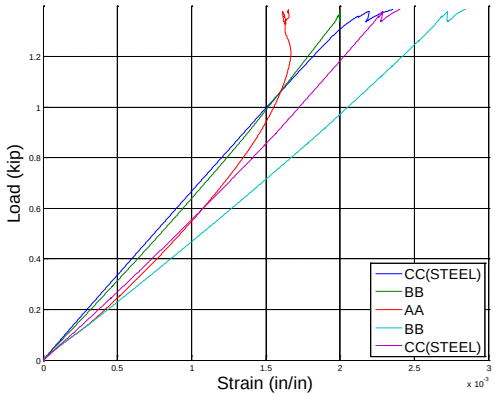

Figure 71. Tensile strain readings, S4

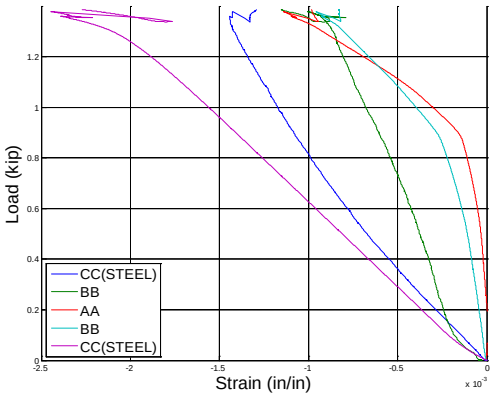

Figure 72. Compressive strain readings, S4

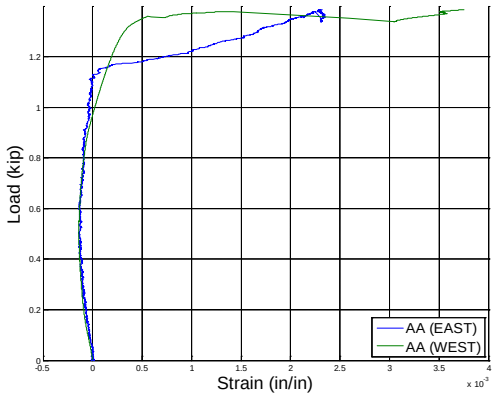

Figure 73. Transverse strain readings, S4

4.5.3 Pole A2 Results

Pole A2 was the second attempt involving an aluminum pole. Substantial yielding occurred in the structure as the load approached 2.45kips, so the test was stopped before failure occurred (the total displacement was limited by the stroke of the actuator). This can be seen in the ultimate deflections reached by the three displacement gauges nearest the cantilever tip (Figure 77). Based on the normalized moment distribution shown in Figure 76, it can be determined that a plastic hinge was expected to initiate in the pole within the wrapped region, similar to S4.

The results of the A2 test confirmed that, in addition to being more representative of field loading, the cantilever testing configuration was successful in demonstrating success of the FRP repair. Along with the large displacements that occurred due to the aluminum pole being substantially more flexible than the steel poles, several signs of FRP debonding were seen including bunching and splitting of the fibers. These indications of failure are shown in Figure 74 and Figure 75, and further supported by the strain measurements shown in Figure 78 through Figure 80.

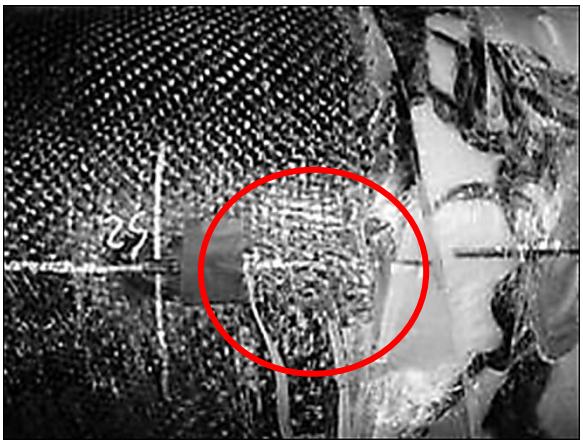

Figure 74. Bunching of FRP on pole A2

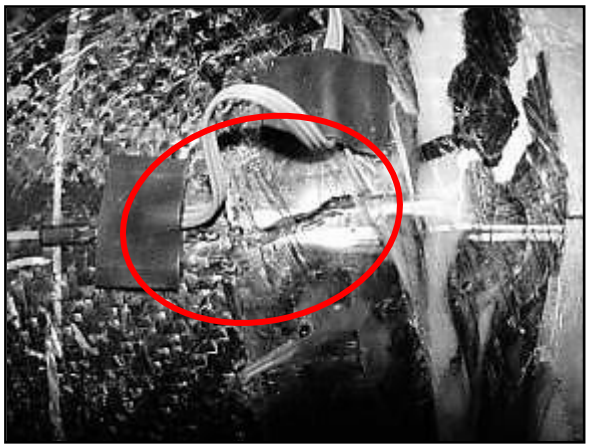

Figure 75. Ruptured FRP on pole A2

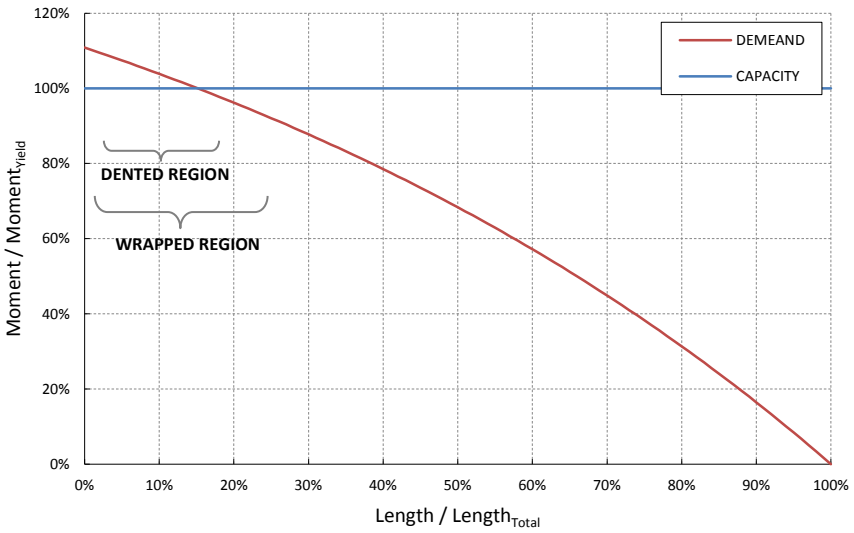

Figure 76. Normalized moment demand and capacity, A2

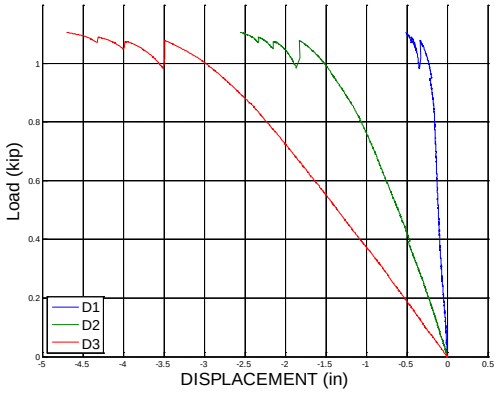

Figure 77. Displacement readings, A2

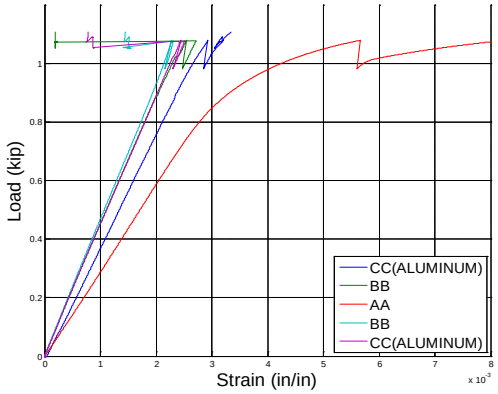

Figure 78. Tensile strain readings, A2

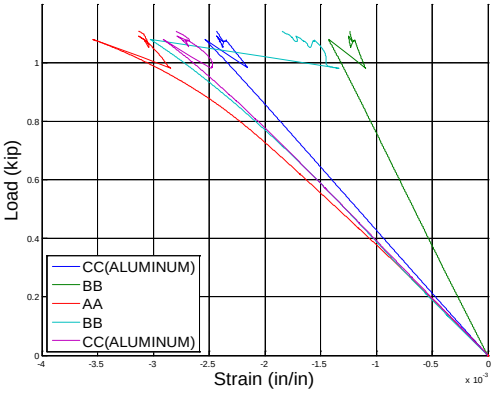

Figure 79. Compressive strain readings, A2

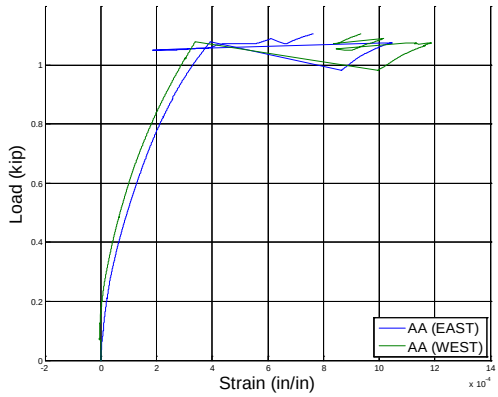

Figure 80. Transverse strain readings, A2

(5) FAILURE MODES

The failure modes observed during the full-scale experimental tests listed in the previous chapter included yielding of the unreinforced substrate, tensile rupture of the FRP, compressive buckling of the FRP, and debonding of the FRP from the substrate. Due to the wrap configurations, debonding of the FRP from the filler material or substrate in and of itself did not lead to global failure, but instead allowed out-of-plane deformations to occur in the compressive FRP leading to compressive buckling of the composite.

Each of these failure modes are discussed in the rest of this chapter in terms of the component material properties that primarily dictate failure. These material properties were incorporated into a nonlinear finite element model of the bond-slip behavior. The results of this model are compared with the experimental results for verification.

5.1 Substrate Yielding

The substrate material properties were experimentally determined at the University of Central Florida's Structural Research Lab following ASTM E8 / E8M testing standards. Dogbone coupons were cut from steel and aluminum pole sections donated for testing from FDOT regional maintenance offices. Figure 81 and Figure 82 show images of tested steel and aluminum dogbone coupons.

The stress-strain curves for these coupon tests are shown in Figure 83 and Figure 84. The linear slope of the elastic region was found for each test and the average value was taken to be the modulus of elasticity for that material. A plot of this average elastic curve is also shown on each figure. The elastic moduli were found to be 29,600ksi (204.1GPa) and

8,250ksi (56.9MPa), while the average yield stresses were 53.8ksi (371MPa) and 33.0ksi (228MPa) for the steel and aluminum, respectively.

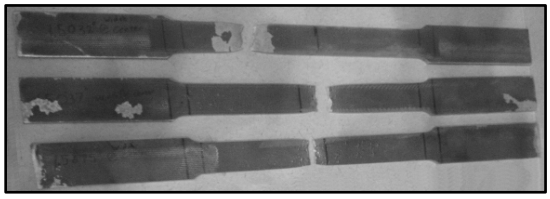

Figure 81. Tested steel tensile coupons

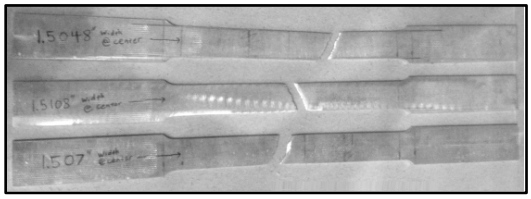

Figure 82. Tested aluminum tensile coupons

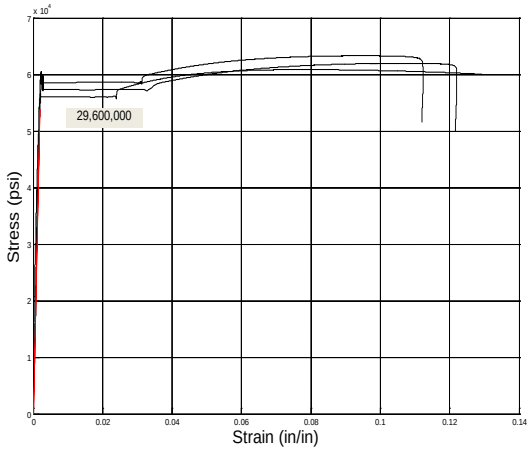

Figure 83. Steel tensile coupon data

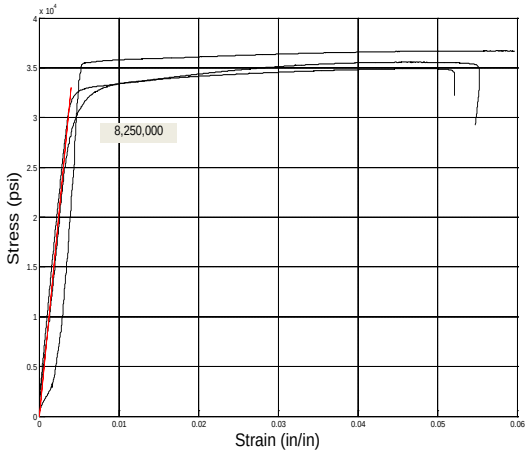

Figure 84. Aluminum tensile coupon data

A piecewise linear model of the stress-strain relationship of each material was produced. A trilinear model reasonably approximates the elastic, yield, and strain hardening of the steel, while a bilinear model was found to accurately describe the aluminum response. These relations are presented in Figure 85 and Figure 86. The approximate ultimate failure stress and strain values were found by averaging the peak stresses and strains from multiple coupon tests. For the steel relationship an additional point was found at the transition from pure yielding to the onset of strain hardening.

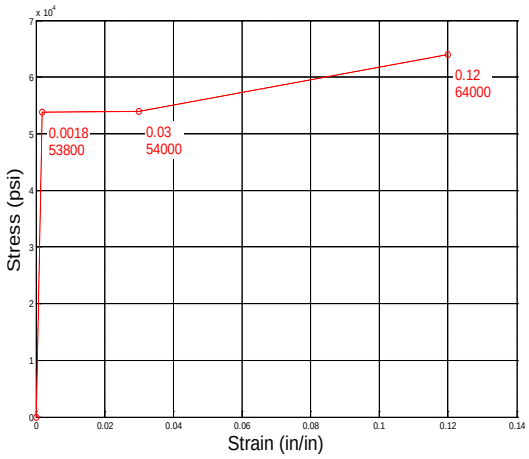

Figure 85. Trilinear tensile model of steel

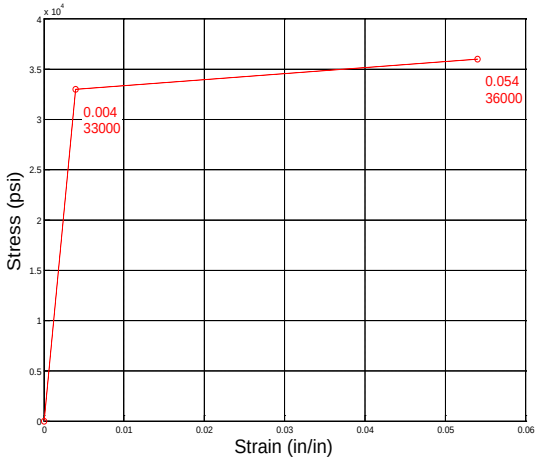

Figure 86. Bilinear tensile model of aluminum

5.2 Composite Tensile Rupture

Similar to the substrate tests, FRP tensile tests were conducted at the University of Central Florida Structural Research Lab in Orlando Florida. Coupons were produced from 12” x 12” (304.8mm x 304.8mm) plates formed for each system consisting of two layers of ether unidirectional or bi-directional woven fibers impregnated by one of the saturating resins listed previously. These plates were allowed to cure for a minimum of 48 hours and then trimmed to form several approximately 10” x 1” (254.0mm x 25.4mm) coupons for each set.

The fibers were orientated axially for the unidirectional weaves and in the 0º/90º directions for the bi-axial weaves, with respect to the coupon geometry. These coupons were then tested in an Instron/SATEC 200 kip universal testing machine (UTM) following ASTM D3039 testing standards (Figure 87). Typical coupon failures are shown in Figure 88 through Figure 90.

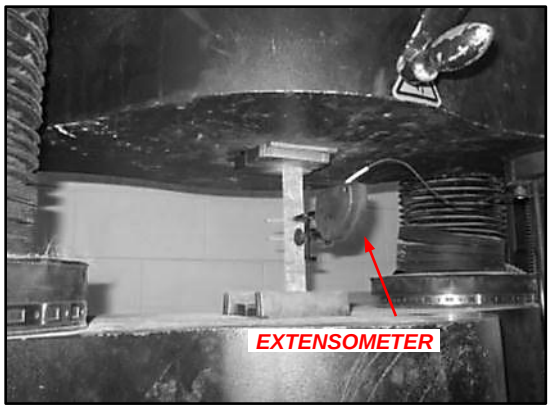

Figure 87. Tensile coupon being tested in UTM

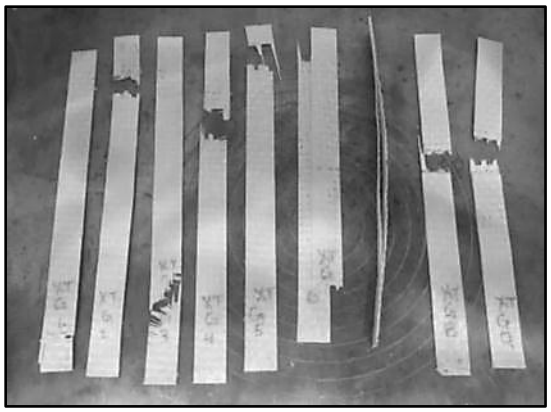

Figure 88. Tested high-density glass XT coupons

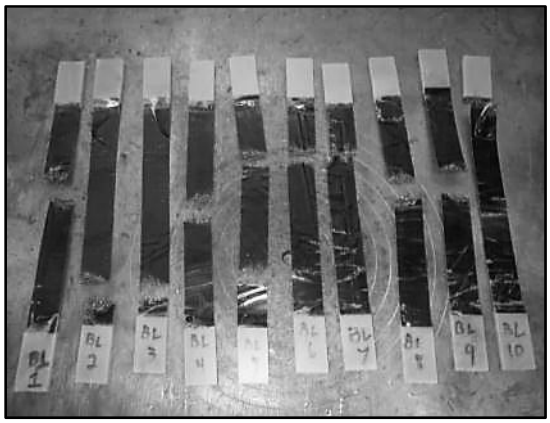

Figure 89. Tested low-density basalt QB coupons

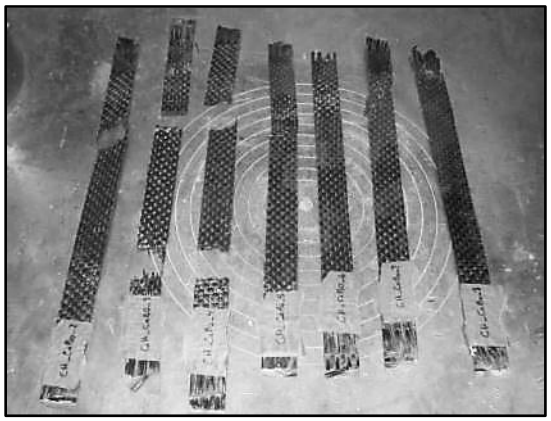

Figure 90. Tested high-density carbon CB coupons

Stress, strain, and load measurements were taken during testing. An Instron extensometer was used to measure strain. So as to prevent damage to the equipment, the extensometer was removed and the strain readings were discontinued prior to the failure of each coupon. After testing, the elastic modulus of each specimen was calculated from a linearization of the stress-strain readings taken, up to the removal of the extensometer. This value, along with the recorded stress at failure, was used to determine the equivalent strains at failure.

Averages of all three of these values for each sample set are presented in Table 5. Due to a manufacturer defect, the pre-impregnated low-density carbon fiber coupons were unable to be tested; therefore, no tensile data is shown for that sample set. The linearized stress-strain data for each sample set of coupons are shown in Figure 91 through Figure 95. Also shown on these graphs is an average-value curve based on the mean failure stress and elastic modulus of the tested coupons.

The average linear plots are reasonable approximations of the stress-strain response of the various FRP systems through tensile rupture. It should be noted that these graphs exclude data derived from any coupons that ruptured within the griped region of the UTM, so as to display a more accurate representation of composite response.

Table 5. Average tensile properties for each sample set

Sample Set		Weight ($^{oz}/_{yd^2}$)	Elastic Modulus (ksi)	Failure Stress (ksi)	Failure Strain (%)
Resin	**Fiber**				
Tyfo® SCH-51	Unidirectional Glass Weave	27	2,755	37.6	1
Sikadur® 300	Unidirectional Carbon Weave	15	9,999	127.3	1.27
CarbonBond™ 300	High-Density Bi-Directional Basalt Weave	24	2,063	31.6	1.53
QuakeBond™ J300SR			1,841	38.6	2.09
NRi XT Polyurethane			1,230	19.6	1.59
CarbonBond™ 300	Low-Density Bi-Directional Basalt Weave	11	2,111	31.9	1.51
QuakeBond™ J300SR			1,757	41.6	2.37
NRi XT Polyurethane			2,472	28.0	1.13
CarbonBond™ 300	High-Density Bi-Directional Glass Weave	24	1,041	34.6	3.32
QuakeBond™ J300SR			1,407	44.9	3.20
NRi XT Polyurethane			2,395	32.1	1.34
CarbonBond™ 300	Low-Density Bi-Directional Glass Weave	11	1,253	20.2	1.62
QuakeBond™ J300SR			1,318	20.2	1.53
NRi XT Polyurethane			1,920	23.2	1.21
CarbonBond™ 300	High-Density Bi-Directional Carbon Weave	12	2,600	62.9	2.42
QuakeBond™ J300SR			2,137	55.8	2.61
NRi XT Polyurethane			5,743	53.8	0.94
CarbonBond™ 300	Low-Density Bi-Directional Carbon Weave	6	4,680	56.8	1.21
QuakeBond™ J300SR			3,109	55.9	1.80
NRi XT Polyurethane			--	--	--

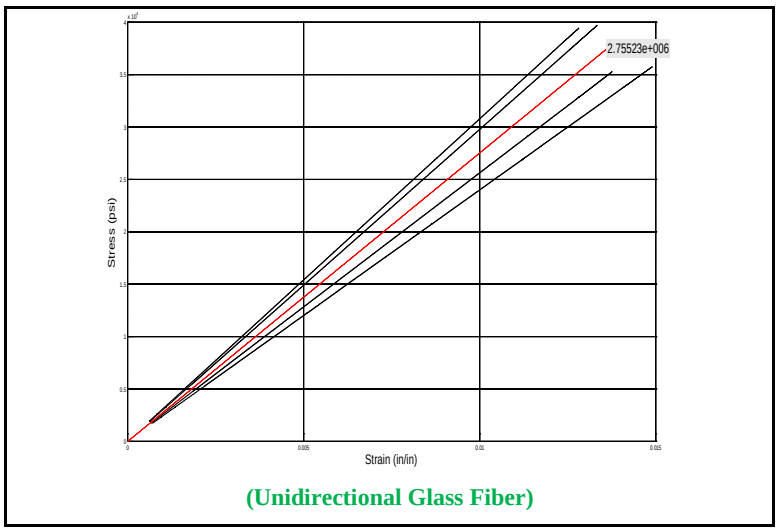

Figure 91. Tyfo® GFRP composite tensile coupon data

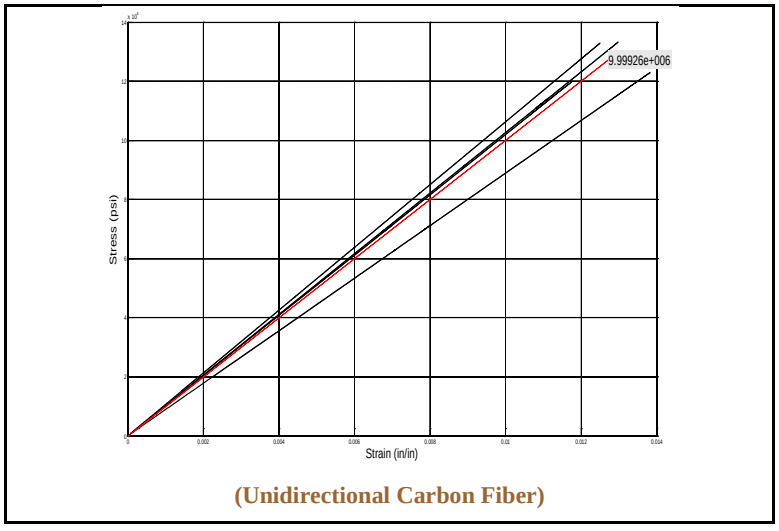

Figure 92. Sikadur® composite tensile coupon data

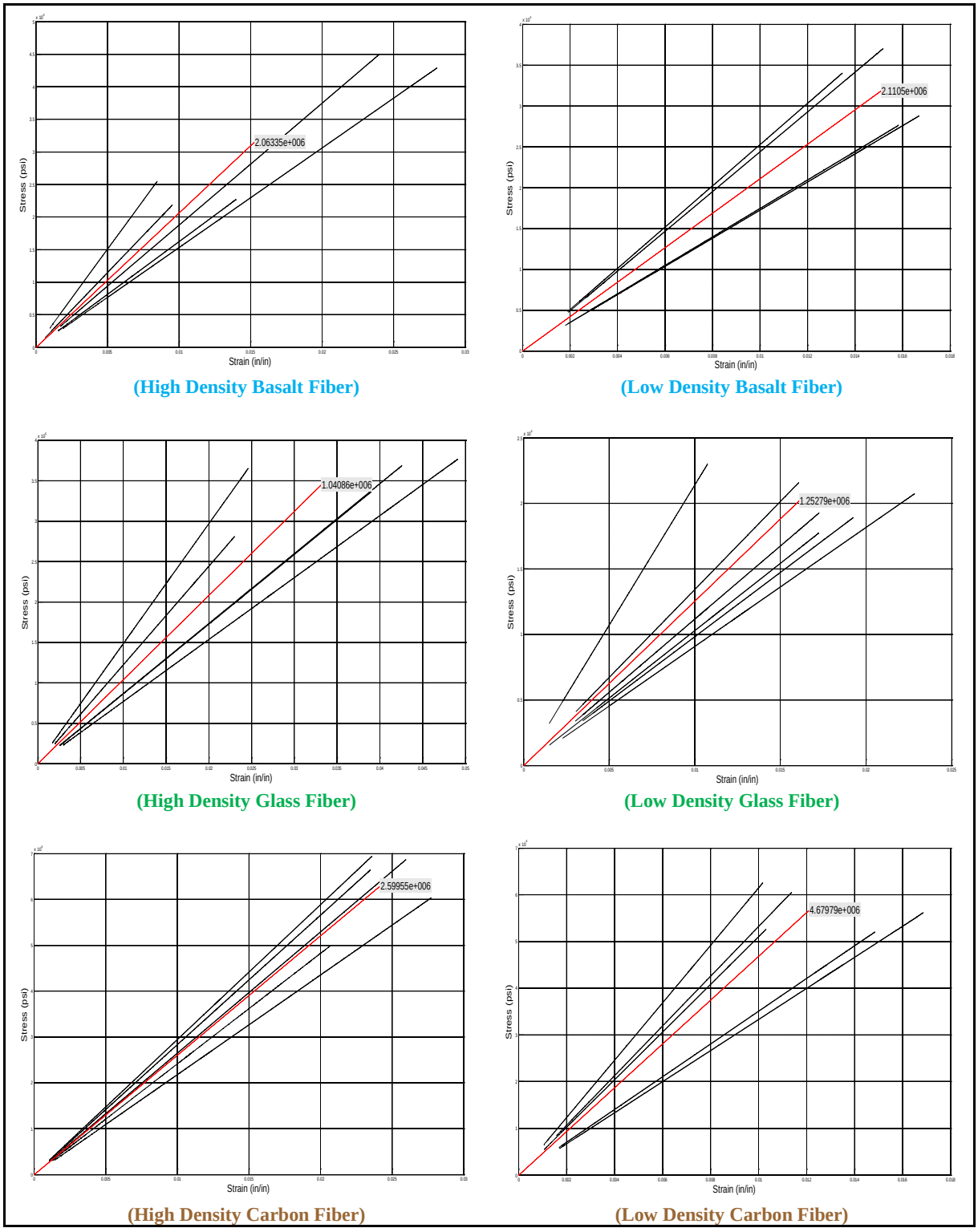

Figure 93. CarbonBond™ 300 composite tensile coupon data

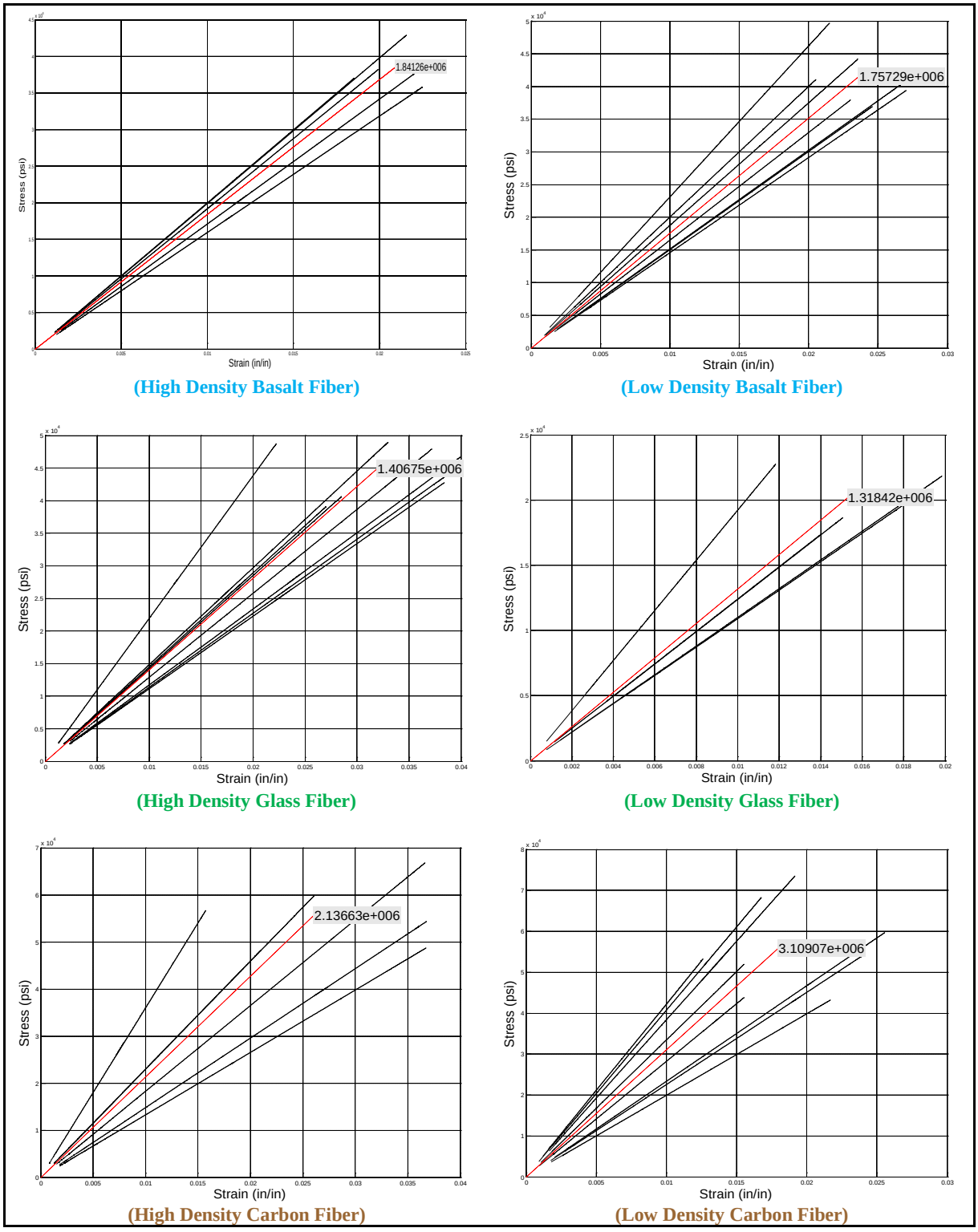

Figure 94. QuakeBond™ J300SR composite tensile coupon data

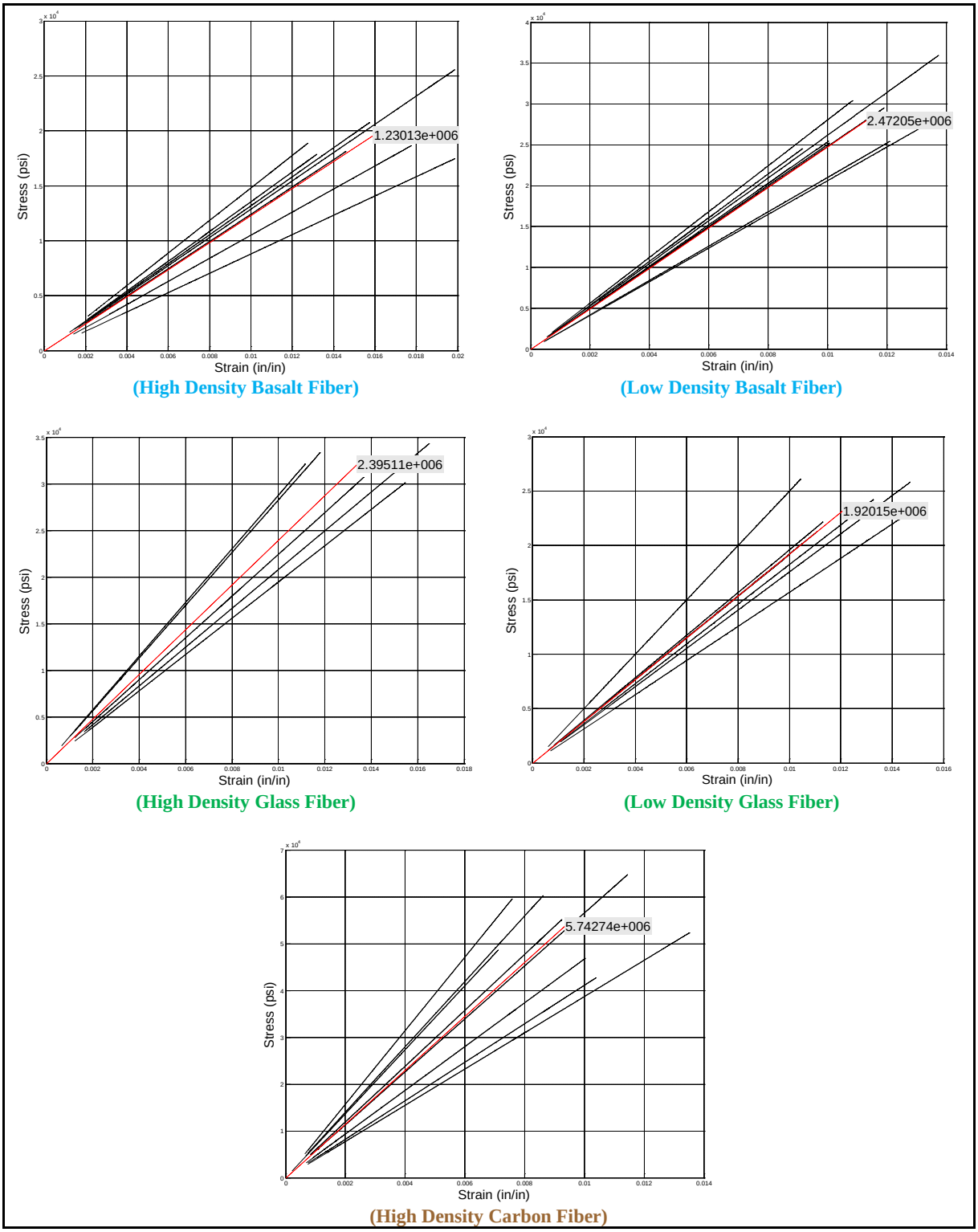

Figure 95. NRi XT composite tensile coupon data

Several observations can be made from the FRP tensile data. As compared with the bi-directional fiber systems, the small scatter associated with the Fyfe Co. and Sika Corp. coupon data indicates that unidirectional FRP systems behave more consistently in tension then do bi-directional weaves. Additionally, the unidirectional glass and carbon systems had higher stiffness then the bi-directional systems tested. Specifically for the bi-directional EP systems, QB tended to outperform the equivalent glass and basalt CB systems; though the carbon fiber CB systems had the highest stiffness and ultimate rupture strength. Finally, the pre-impregnated polyurethane composites tended to behave more uniformly then the equivalent bi-directional EP systems.

5.3 Composite Compressive Failure

To determine the response of the FRP systems under an axial compressive lodging, a set of compressive tests was conducted for the QB and XT repair systems using high-density bi-directional basalt and glass fiber weaves (BH and GH). The testing procedure followed was a variant of ASTM D5467 where an FRP plate is bonded to the top flange of a small aluminum beam and placed in four-point bending. A diagram of the testing configuration per the ASTM standard is given in Figure 96.

Due to the relatively low stiffness and expected high strength of the composites, the procedures were slightly modified for these systems. A 12in long (305mm) square aluminum pipe section with 1in (25mm) outer diameter and 0.625in (1.58mm) wall thickness was used as the core beam section. To prevent local buckling of the pipe, the load points were reinforced by placing two small pieces of discontinuous #8 rebar within the pipe.

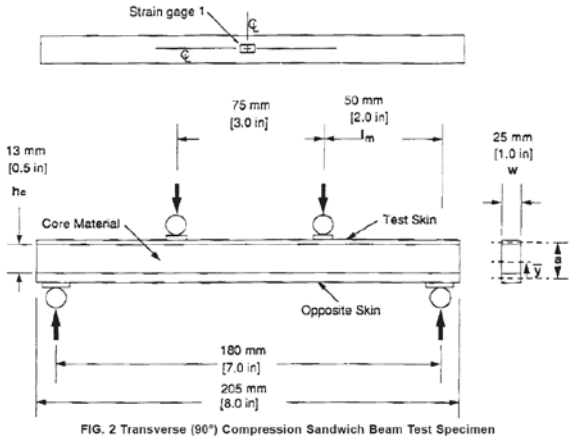

Figure 96. FRP compressive test diagram (ASTM D5467)

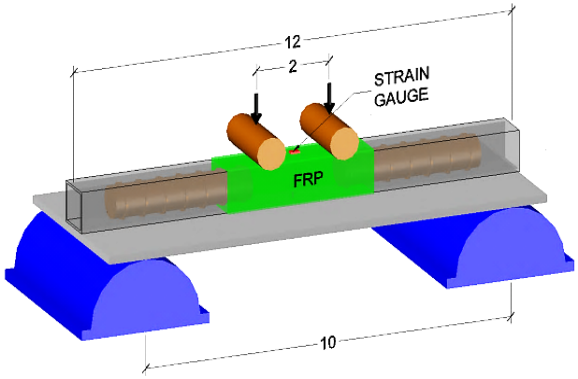

Figure 97. FRP compressive test variation setup

The FRP was installed as a circumferential wrap around the aluminum pipe section to help resist debonding and out-of-plane movement during testing. Finally, to induce sufficient strain within the FRP a 0.188 in (4.8mm) thick aluminum plate was attached to the tension face of the pipe section with a single threaded bolt at the midpoint of the constant moment region. The width of this plate was cut to 5in (127mm) and7 in (178mm) for the XT and QB systems, respectively. A schematic of this setup is given in Figure 97.

Testing took place at the University of Central Florida Structural Research Lab in Orlando Florida using an Instron/SATEC 200 kip UTM. The load was applied at 0.1in/min (0.04mm/s) in a four-point bending configuration as shown in Figure 98 and Figure 99. The top point loads were spaced at 2in (51mm) on center, and the clear span was set to 10in (254mm). A single 6mm 120-Ω foil strain gauge was adhered in the axial direction to the top of the FRP within the constant moment region. The load and strain reading were recorded for each test.

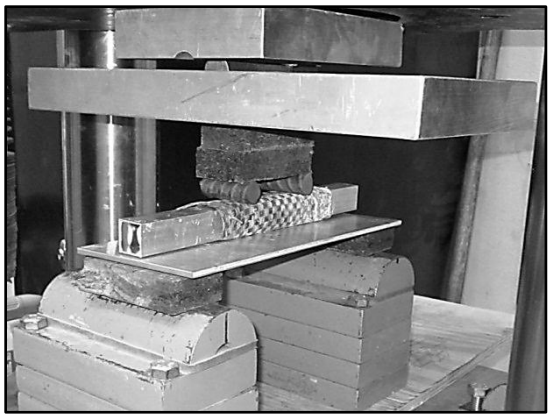

Figure 98. FRP compressive test, unloaded

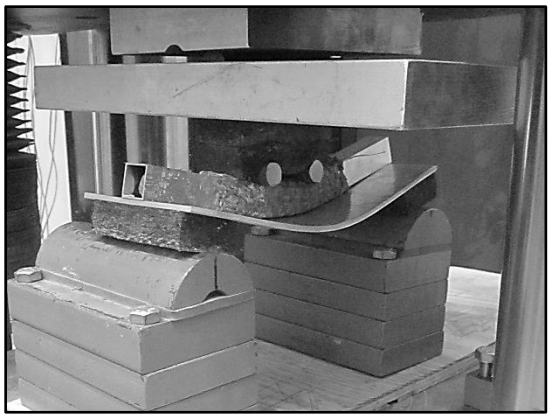

Figure 99. FRP compressive test, under loading

The compressive stress acting on the FRP was calculated per ASTM specifications and is plotted for each test in Figure 100 and Figure 101 with respect to the strain readings. The compressive modulus can then be determined from a linear fit of this data. ASTM permits the use of both linear and bilinear compressive moduli; therefore, a two part bilinear relationship was found for each FRP system tested. These relationships are also shown in each figure.

The compressive modulus is defined as the slope of the first segment of the bilinear relationship. These values were derived and are presented in Table 6 and Table 7 for the QB and XT systems, respectively. The stress and strain values at the transition point and at ultimate failure are also given in this table.

Table 6. Bilinear compressive properties for FRP impregnated with QuakeBond™ J300SR resin

Fiber Type	Compressive Modulus (ksi)	Transition Stress (ksi)	Transition Strain (%)	Failure Stress (ksi)	Failure Strain (%)
High-Density Bi-Directional Basalt	8,050	3.828	0.05	7.657	0.20
High-Density Bi-Directional Glass	7,694	4.247	0.06	8.494	0.22

Table 7. Bilinear compressive properties for FRP impregnated with NRi XT polyurethane resin

Fiber Type	Compressive Modulus (ksi)	Transition Stress (ksi)	Transition Strain (%)	Failure Stress (ksi)	Failure Strain (%)
High-Density Bi-Directional Basalt	4,295	5.235	0.12	10.471	0.93
High-Density Bi-Directional Glass	8,789	6.167	0.07	12.333	0.64

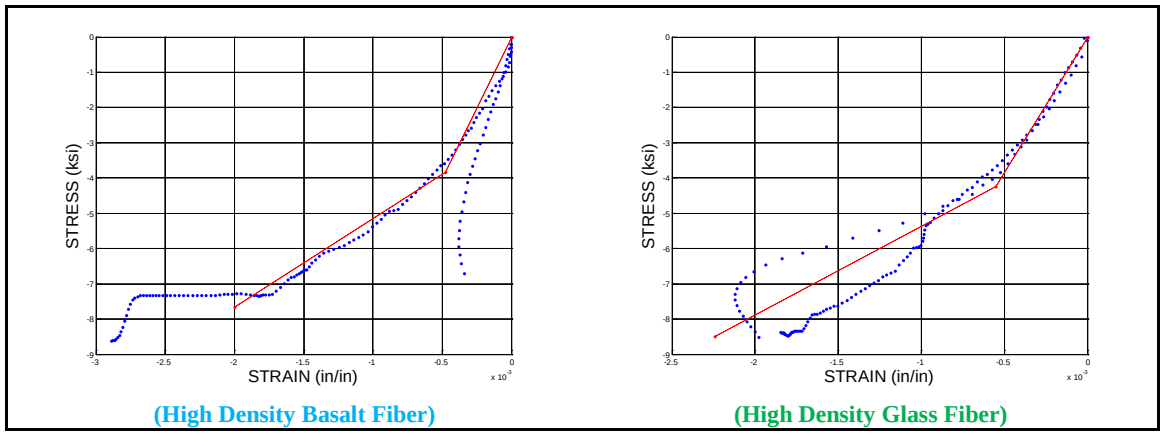

Figure 100. QuakeBond™ J300SR composite compressive coupon data

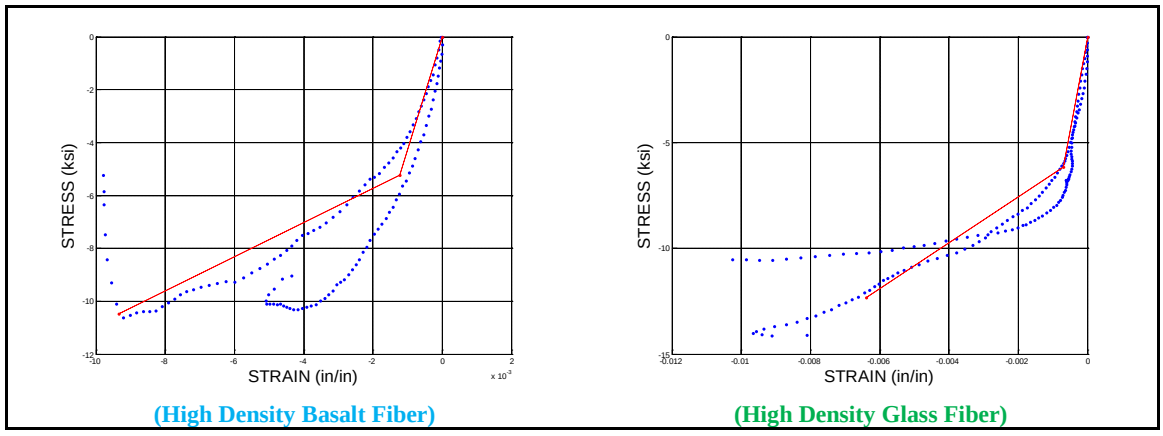

Figure 101. NRi XT polyurethane composite compressive coupon data

Inducing true compressive failure proved to be difficult. Often the failure occurred when the aluminum substrate hinged beneath the FRP, inducing debonding, and ultimately, folding of the compressive fibers. This form of failure can be seen in Figure 102, Figure 103,

and Figure 104. Additionally, both high-density BFRP tests involving XT polyurethane resin failed when the aluminum substrate ruptured beneath the tension FRP, causing the tensile FRP to also rupture (see Figure 105). For this reason, the ultimate failure values shown should be taken as a lower limit, and not necessarily as the compressive failure capacity.

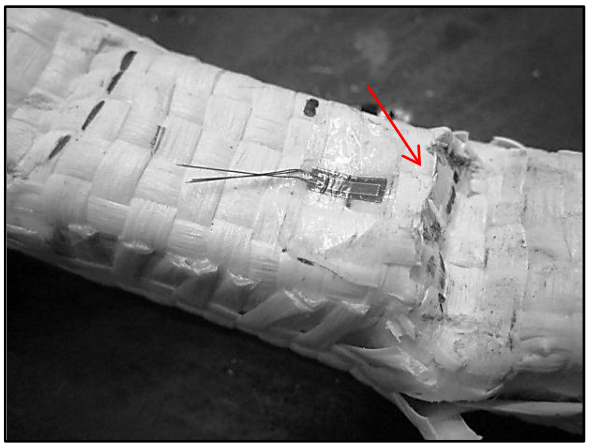

Figure 102. GFRP filament folding failure

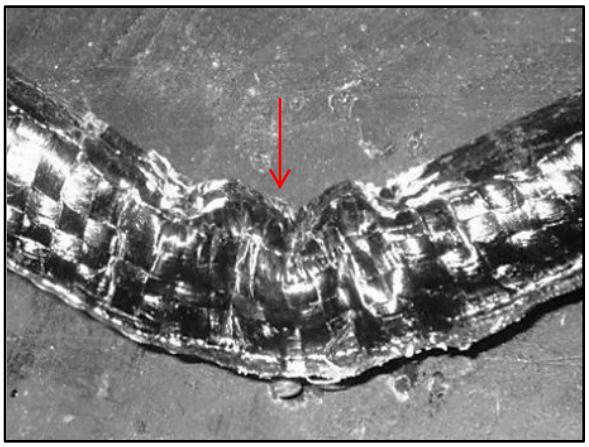

Figure 103. BFRP wrinkling failure

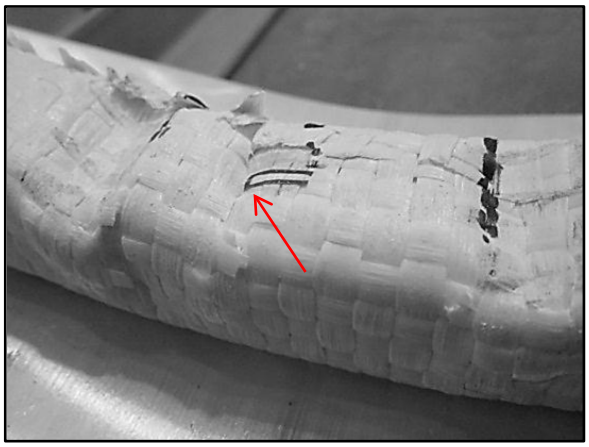

Figure 104. GFRP wrinkling failure

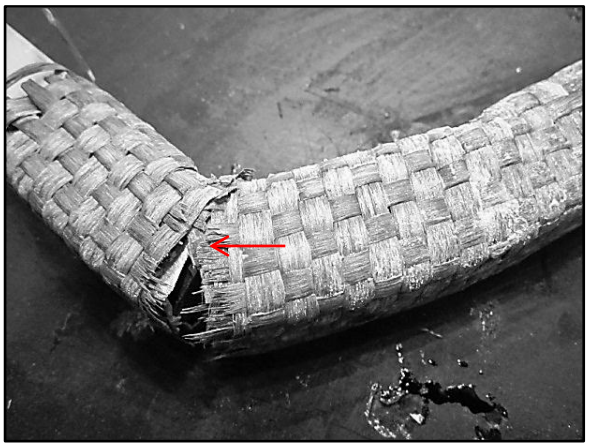

Figure 105. Substrate and FRP rupture

5.4 Debonding

The interface between a bonded FRP composite and the substrate can involve a complex state of stress. Shear and normal stresses, as well as peeling effects can all play a role in determining how a bond failure might occur. For this reason, few simple models accurately describe composite debonding. However, average peak bond stresses acting over a relatively small area will be used to make an initial comparison of the various systems. A more detailed understanding of the debonding phenomena can then be found through more extensive experimental bond-slip modeling.

5.4.1 Average Peak Bond Strength

Three small-scale tests were performed to examine the bond strength of the various FRP systems. The first of these tests involved circumferentially laminated steel pole sections placed in tension to investigate the effects of curvature on shear bond strength. The second set of tests used a single-lap setup to find average peak shear stress values for each FRP system. The third test used an adhesion tester to find the peak normal bond stress.

5.4.1.1 Circumferential Bond Test

The first of the small-scale bond strength tests involved the use of a small pole section taken from one of the tested steel poles, approximately 18” in length. The section tapered 8.437” to 8.625” (214mm to 219mm) in diameter. This section was split through their circumferences and then the two pieces were stacked and laminated together with a single layer of the Tyfo® SHE-51 GFRP composite lapped around the exterior as shown in Figure 106.

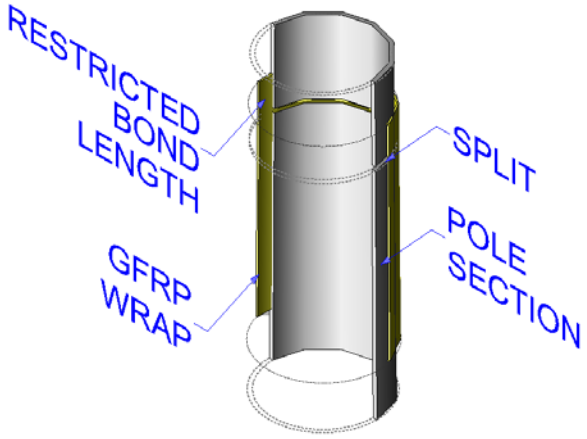

Figure 106. Circumferential bond test schematic

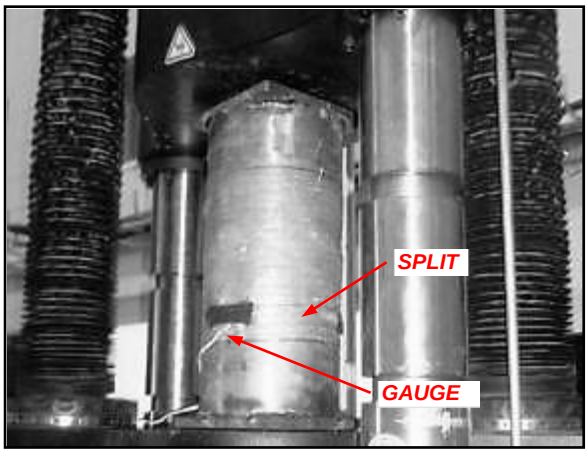

Figure 107. Picture of circumferential bond test

The GFRP was then cut a distance away from one side of the split in the pole sections to restrict the GFRP bond length. The bond length on the opposite side ranged from three to four times the restricted length to ensure that debonding would occur on the intended side. An 8" x 8" x ¾" (203mm x 203mm x 19mm) steel plate was attached to both ends of the pole sections with ½" fillet welds around the perimeter. High strength threaded rods were bolted through these plates and anchored to the UTM as shown in Figure 107.

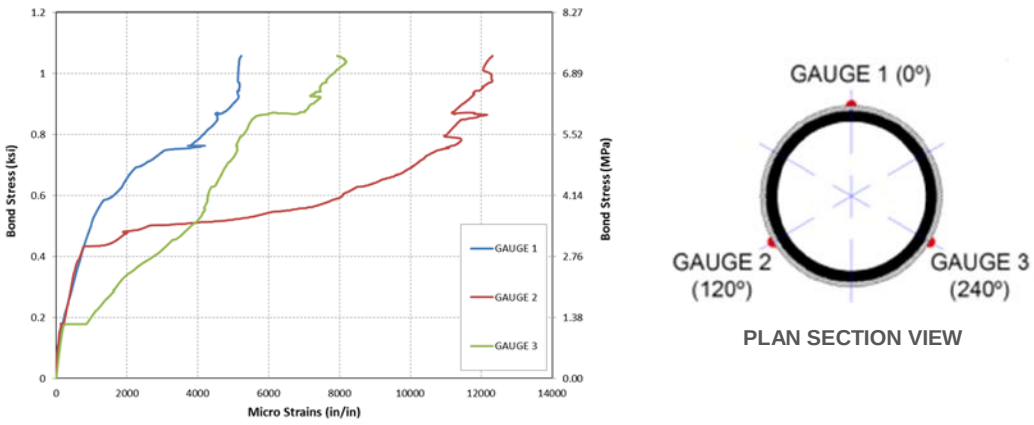

Figure 108. Load vs longitudinal strains readings during circumferential bond test

A tension force was applied to these specimens until the GFRP debonded from the steel and caused the two pieces of the pole to separate. The specimen was tested three times with minimal bond lengths of 2.25 in, 1.75 in, and 1.25 in (57mm, 44.5mm, and 32mm) resulting in ultimate loads of 34.5 kips, 29.0 kips, and 25.4 kips (153kN, 129kN, and 113kN), respectively. Strain data was collected from three axial 120Ω strain gauges spaced evenly around the circumference of the pole at the midpoint of the restricted bond area for the third test (shown in Figure 108).

It was observed during these tests that debonding did not occur uniformly around the circumference of the specimens. Instead, the debonded region spread in the axial direction locally before spreading circumferentially. This observation is confirmed in Figure 108, as the strain gauges show large increases in local strain (due to local debonding of the GFRP from the substrate) at different points during the loading. Additionally, the rate at which the debonding occurred was not uniform for each test, happening most rapidly for the 1.75 in (44.5mm) length and most gradually for the 2.25 in (57mm) bond length.

5.4.1.2 Single-Lap Bond Test - Tyfo®

The second of the small-scale bond strength tests involved single-lap tension testing of several metal coupons. Initially, dogbone coupons identical to those used for the substrate material classification were used. These were first cut across the 1.5 in (38mm) portion and then laminated back together with a single layer of Tyfo® SHE-51 GFRP on the side which corresponded to the exterior surface of the pole, as shown in Figure 109.

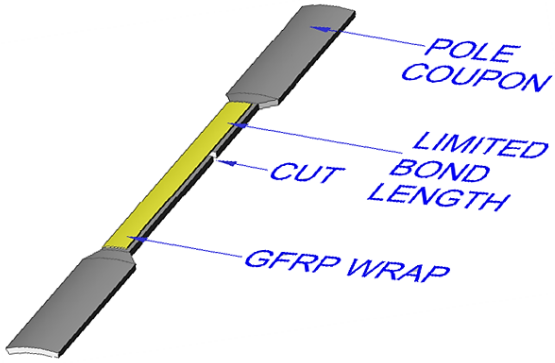

Figure 109. Lap-shear bond test schematic (1)

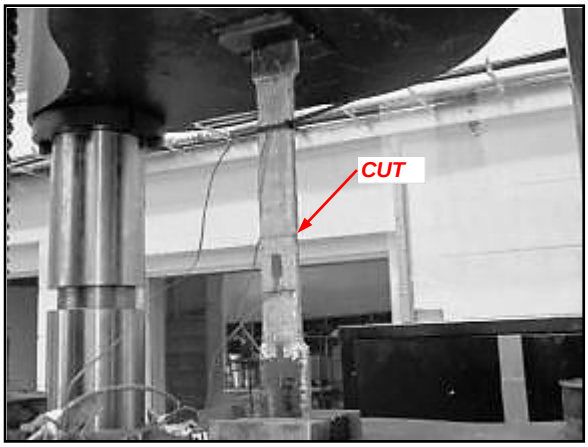

Figure 110. Picture of lap-shear bond test (1)

The bonds were limited along one side of the cut and then tested. Aluminum coupons were also tested in this configuration. The maximum load achieved before failure averaged over the bonded area is taken as the average ultimate bond stress. The results of each of these tests are presented in Table 8.

A graph of bond-length verses average failure stress is shown in Figure 111, with similar values from the circumferentially laminated bond tests shown for comparison. The data shows that as the bond length increases, the stress becomes more evenly distributed along this length, causing the average bond strength to approach a constant value.

Table 8. Average ultimate bond stress achieved (psi) - Tyfo®

Substrate Material	Restricted Bond Length (in)						
	0.5	1.0	1.5	2.0	2.5	3.0	3.5
Steel	1257	820	703	600	751	459	517
Aluminum	- -	- -	1433	1182	467	365	- -

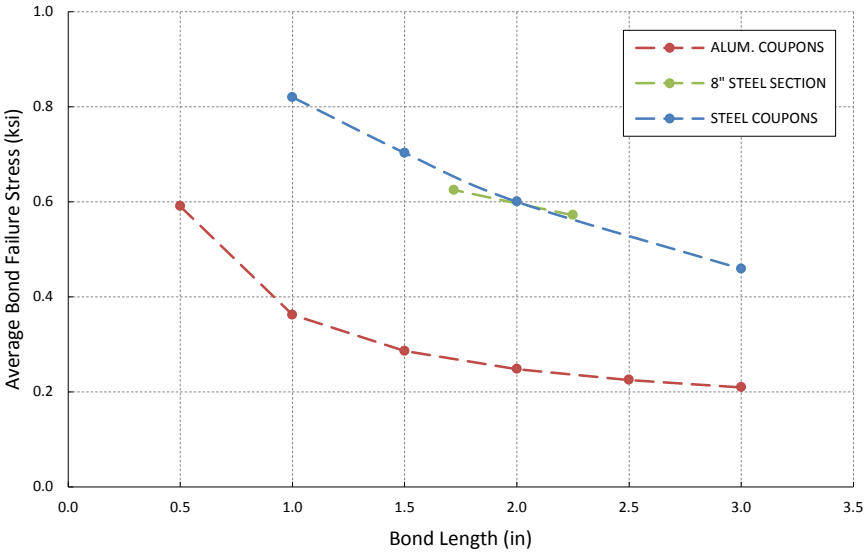

Figure 111. Bond-length vs average failure stress: single-lap and circumferential bond tests

It can also be seen from this figure that a trend is formed by the coupon tests, and that the failure of the circumferentially laminated pole section falls along this line. The relationship between these sets of data indicates that single-lap bond testing reasonably describes the shear bond strength around the circular geometry of a pole sections.

5.4.1.3 Single-Lap Bond Test - CB, QB, and XT

Further lap-shear tests were conducted using the CB, QB, and XT reinforcement systems and each of the high-density bi-directional fibers listed in Table 2. These tests used flat rectangular aluminum or galvanized steel sections that were all approximately 12in (305mm) long and 1.5in (38mm) wide. The steel and aluminum plates were 0.25in (6mm) and 0.188in (5mm) thick, respectively, and the same grade as poles taken from the field.

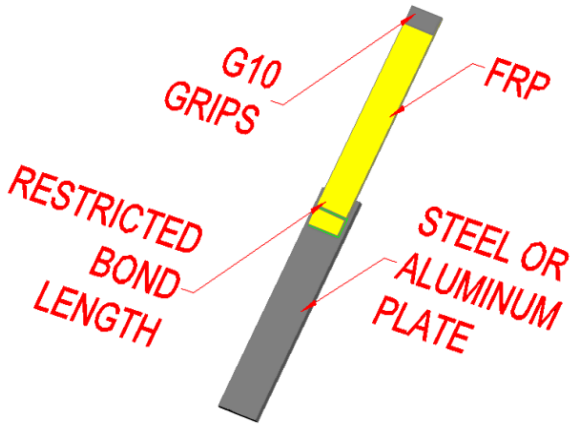

Figure 112. Lap-shear bond test schematic (2)

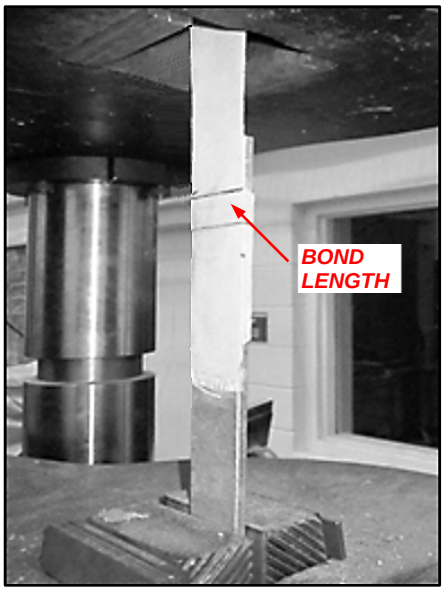

Figure 113. Picture of lap-shear bond test (2)

The FRP was bonded to the plates with approximately 0.5in (13mm) of overlap and 4in to 8in (102mm to 204mm) of FRP overhanging the plate (see Figure 112). G10 fiberglass grips were adhered to the ends of the FRP to prevent crushing. The metal plate and FRP were loaded directly into the UTM for testing as shown in Figure 113. The results of these lap shear bond tests are given in Table 9.

Table 9. Average ultimate bond stress achieved (psi) - CB, QB, and XT

Adhesive	Matrix Material	Substrate Material	Average Lap-Shear Bond Stress		
			High-Density Basalt Fiber	High-Density Carbon Fiber	High-Density Glass Fiber
QuakeBond™ J201TC	QuakeBond™ J300SR	Aluminum	911.78	654.29	711.36
		Steel	777.08	636.36	466.16
CarbonBond™ 200P	CarbonBond™ 300	Aluminum	451.52	1,194.13	1,079.80
		Steel	383.75	784.51	616.52
Syntho-SubseaLV	NRi XT Polyurethane	Aluminum	515.66	663.30	308.33
		Steel	440.45	349.24 psi	266.41

5.4.1.4 Normal Pull-Off Bond Test

Along with the shear stress tests described previously, a series of tests to determine the maximum normal bond stresses were conducted for each system. These tests were conducted using 20mm aluminum dollies and a PosiTest© Manual Adhesion Tester sold by DeFelsko following ASTM D4541, the Standard Test Method for Pull-Off Strength of Coatings Using Portable Adhesion Testers (Type A5). This document states that this test method maximizes tensile stress as compared to the shear stress applied by other methods; therefore, the results may not be directly comparable.

Each high-density FRP system described previously was bonded to steel and aluminum plates using the paired adhesives listed in Table 9. Multiple 20mm aluminum dollies were then adhered to the top of the FRP layer. A circular groove was etched around the base of these dollies through the FRP, but leaving the substrate intact (see Figure 115). Finally, the Manual Adhesion Tester was used to apply a normal uplift force to the aluminum dollies until debonding occurred, and the peak debonding stress was electronically recorded. The testing configuration is shown in Figure 114.

Due to the variability of the results, many repetitions were necessary to produce data that reasonably describes the normal bond stress. Often, the dollies would debond from the FRP before the FRP would debond from the substrate. When this occurred a normal bond stress data point was not collected.

The results of the normal pull-off tests are plotted against the results of the single-lap bond tests for each system tested. These are given in Figure 116 through Figure 118. It can be seen from this data that the highest variability occurred with the high density carbon fiber systems. Additionally, the QuakeBond™ (QB) system tended to outpreform the

CarbonBond™ (CB) and NRI polyurathain (XT) systems when dealing with high density Glass and Basalt fibers. For these two fiber types, the NRI system was the most consistant, but also demostrated the lowest peak bond stresses.

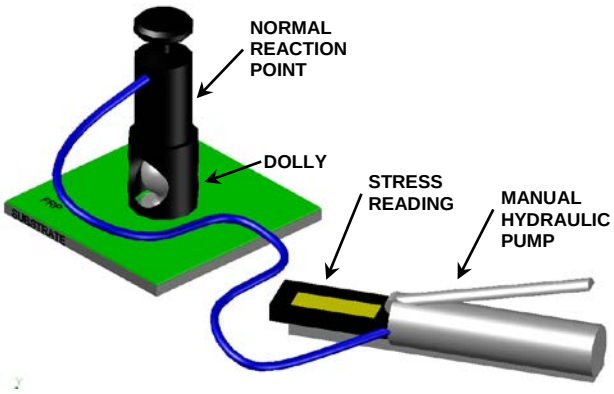

Figure 114. PosiTest© manual adhesion tester schematic

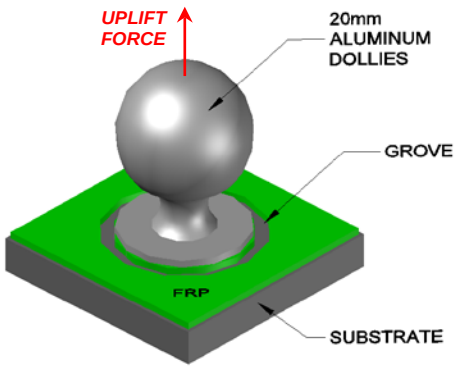

Figure 115. Aluminum dolly schematic

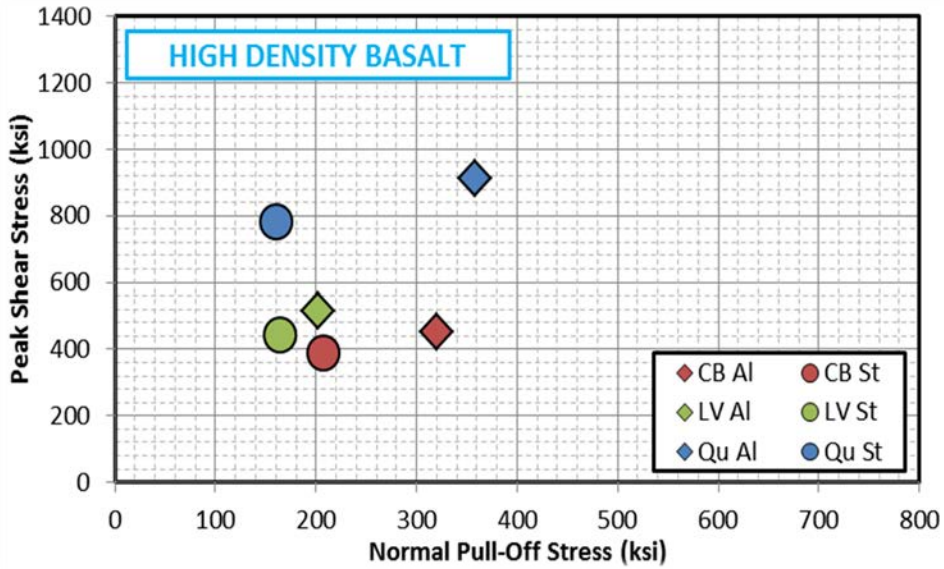

Figure 116. Shear bond vs normal bond strength of high-density BFRP systems

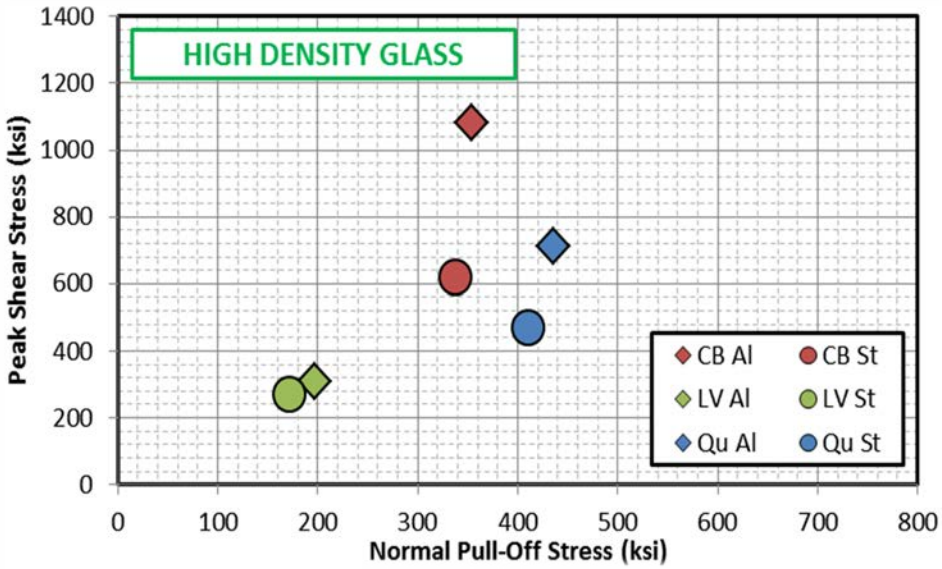

Figure 117. Shear bond vs normal bond strength of high-density GFRP systems

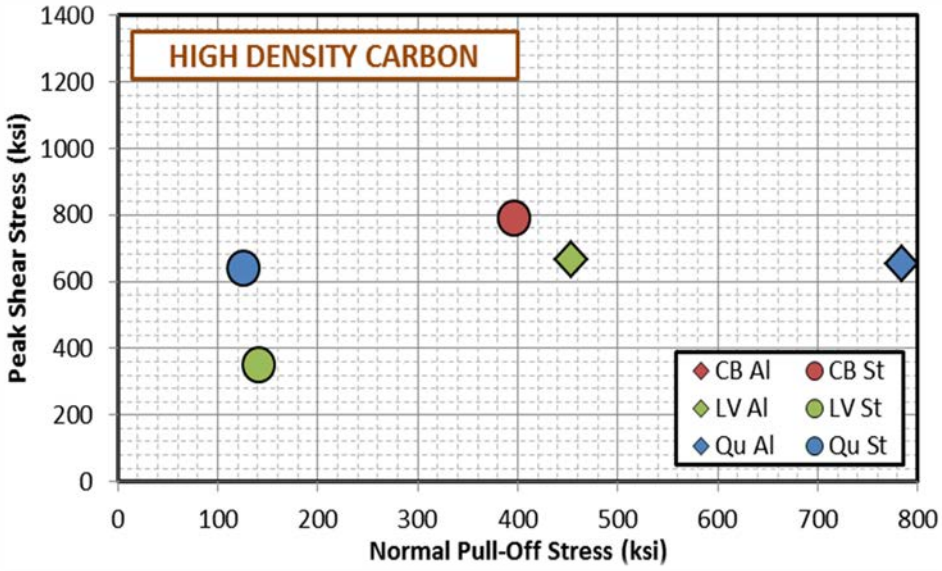

Figure 118. Shear bond vs normal bond strength of high-density CFRP systems

Both the normal and shear bonds of each FRP system were higher for aluminum then steel substrates. Additionally, the FRP systems with the largest strains at failure (QB for BH, CB for GH, and QB for CH) seemd to also have higher average bond stresses at failure. This indicates that softer materials can more eveny distribute the bond stresses, thus achieve

higher average bond strengths. Conversly, the polyurathain composits consistantly produced the lowest strains at failure, as well as the lowest average shear and normal bond strengths.

5.4.2 Bond-Slip Characterization

An initial comparison of the average peak bond stresses described previously indicates that among the EP systems tested, the QB system outperformed the CB systems for bond between basalt or glass fiber composites to both steel and aluminum. Therefore, the QB repair system was selected for additional investigation. For comparison purposes, bond-slip modeling was also performed for the basalt and glass fiber polyurethane systems. The testing procedures and results of these tests are presented in the following subsections.

5.4.2.1 Experimental Configuration

The specimens used for these tests involved 1.5in (38mm) wide aluminum or galvanized steel plates with a single 1.0in (25mm) wide double-layer plate of FRP lap-bonded to one side. The plates were made from 0.25in (6.35mm) thick galvanized A572 steel and 0.188in (4.78mm) thick AA6063 aluminum, similar to that used in FDOT standard utility poles and mast-arms. The bond areas were 1in (25mm) wide and initially 2.0in (51mm) in length for each specimen, and then extended to 3.0in (76mm) in length for the aluminum tests so as to better observe the entire bond development length. QuakeBond™ J201TC EP adhesive was used to bond the FRP to the substrate for each test.

Four 3mm 120-Ω strain gauges were adhered to the outer layer of FRP along the 2.0in (51mm) bond lengths, and five gauges were used along the 3.0in (76mm) bond length to map the strain gradient. The 2in and 3in gauge layouts are schematically shown in Figure

119. These specimens were then tested in a tension-loading configuration with a displacement controlled loading rate of $0.03\frac{in}{min}$ ($0.0125\frac{mm}{s}$). The grips of the UTM were adjusted to achieve vertical alignment of both the FRP coupon and metal plate with minimal induced moment. The testing configuration can be seen in Figure 120. To prevent damage occurring to the fibers from the UTM during loading, G10 fiberglass plates were adhered to the gripped portion of the polyurethane FRP coupons.

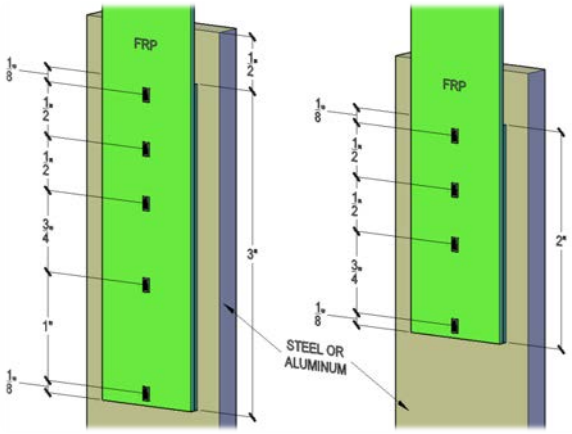

Figure 119. Bond-slip gauge configuration

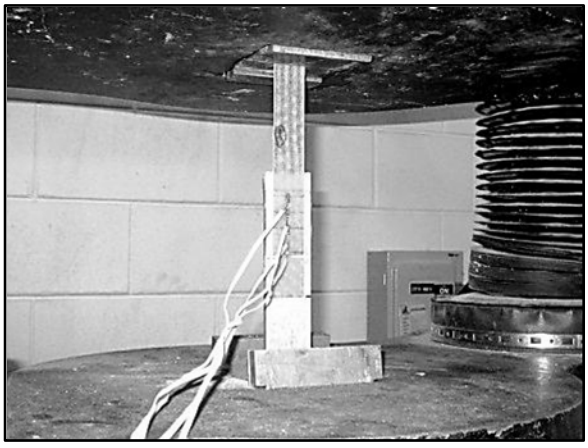

Figure 120. Picture of bond-slip test specimen

5.4.2.2 Experimental Results

The results of the bond-slip experimental modeling are given in this section. Four specimens were prepared and tested for each permutation of BH and GH fibers impregnated with QB and XT repair systems and adhered to aluminum and galvanized steel substrate. The total shear and total slip at the free end of the bond were found at multiple load steps for each specimen using equations 14 and 15 presented in chapter 2.

The strain gauges were carefully adhered in the direction of loading, with an attempt being made to place the gauges completely on fibers oriented in the axial direction. However, on several occasions one or more of the gauges appeared to be recording inaccurate values. When this occurred, the results were considered erroneous and were discarded. Therefore, only two sets of data are presented for each set of specimens tested. This data is given in Figure 121 through Figure 124 for each fiber type, FRP system, and substrate.

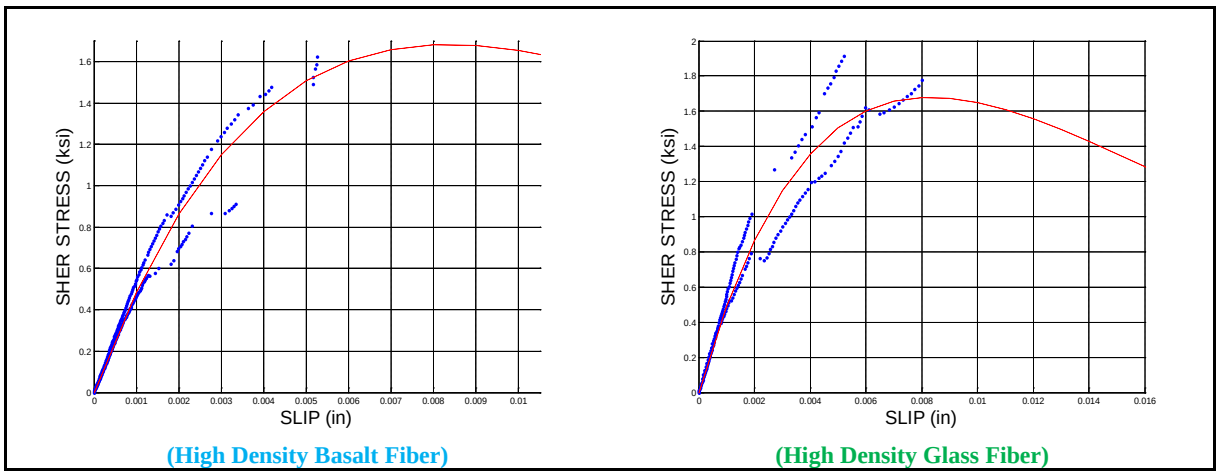

Figure 121. QuakeBond™ J300SR impregnated FRP bonded to steel substrate

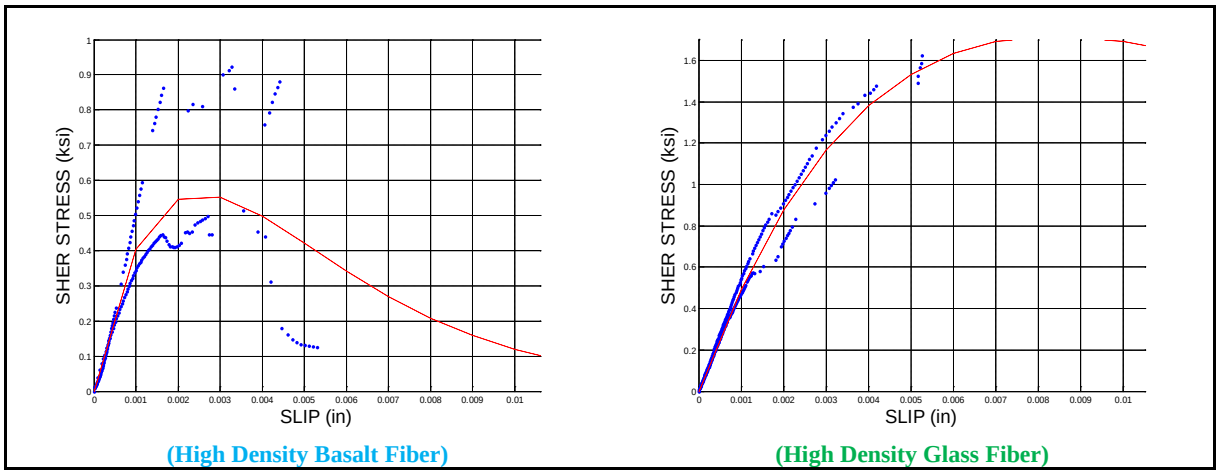

Figure 122. NRi XT impregnated FRP bonded to steel substrate

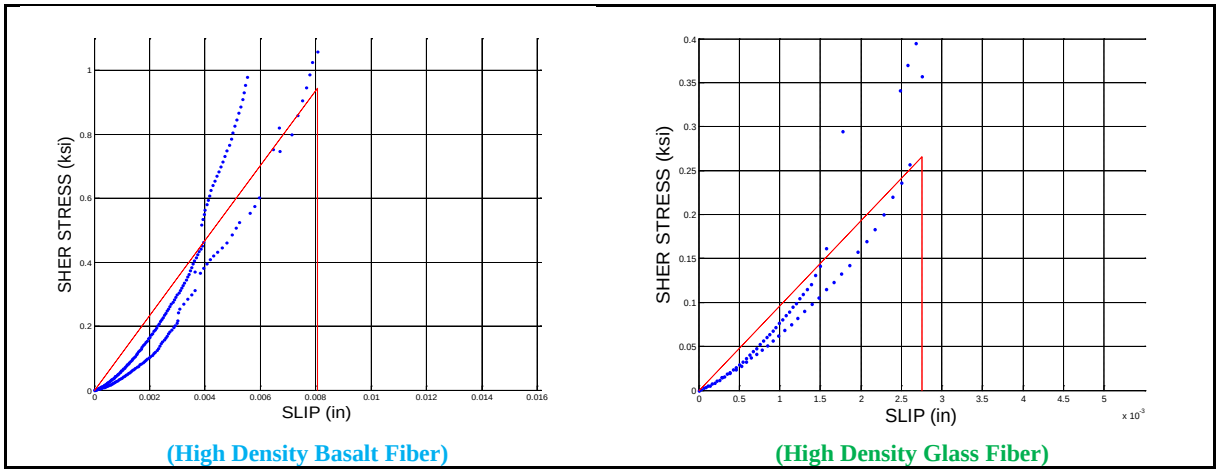

Figure 123. QuakeBond™ J300SR impregnated FRP bonded to aluminum substrate

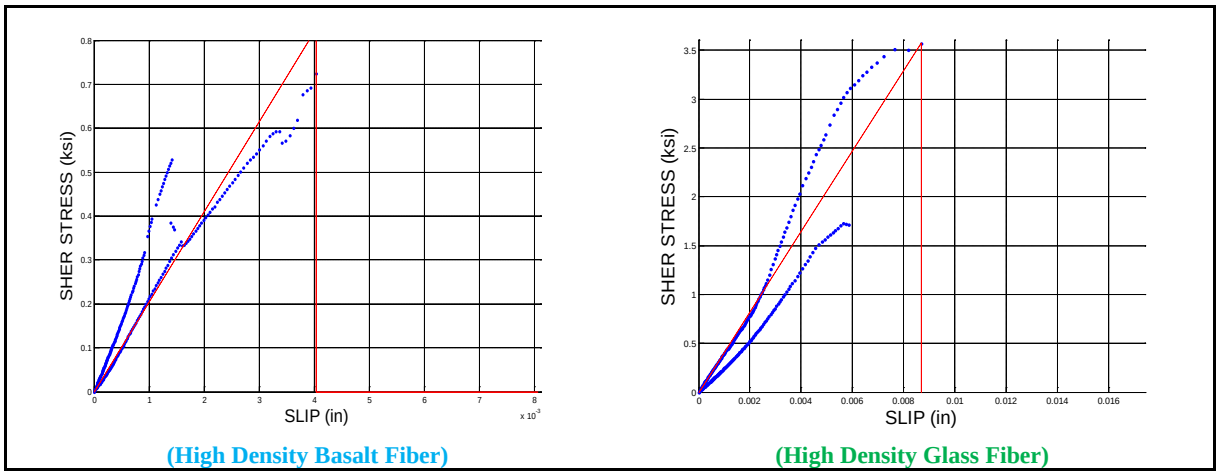

Figure 124. NRi XT impregnated FRP bonded to aluminum substrate

As mentioned in chapter two, several functional forms are commonly used to describe the bond-slip relationship of FRP. Two of these forms were fitted to each set of data using a standard nonlinear regression tool within the MatLab software program (implementing the Levenberg-Marquardt algorithm of nonlinear least squares). Exponential and bilinear models were selected due the ease with which they can be incorporated into the MSC.Marc nonlinear finite element program. These bond-slip models are defined by the functions:

$$\tau(s)_{\text{exponential}} = G_C\left(\frac{s}{V_C{}^2}\right)e^{-s/V_C} \quad (18)$$

and

$$\tau(s)_{\text{bilinear}} = 2\left(\frac{G_C}{V_C}\right)\left(\frac{s}{V_C}\right) \quad (19)$$

where $\tau(s)$ is the total shear defined as a function of slip, S is the total slip, and V_C and G_C are parametric constants that relate to the slip at peek shear and overall scale of the function, respectively. By defining the V_C and G_C values that best fit the experimental data, an expected shear stress can be found for any given slip increment.

Additionally, the mean squared error (mse) for both of these fitted functions was calculated for each set of tests. The accuracy of each fit is defined as $(1 - mse)(100\%)$. These parameters, as well as the fit accuracy value for both functions are presented in Table 10 and Table 11. The model with the best fit value for each test is also shown with the test data in Figure 121 through Figure 124.

Table 10. Bond-slip model properties for FRP systems adhered to steel substrate

Matrix Material	Fiber Type	Exponential Model			Bilinear Model		
		G_C	V_C	fit	G_C	V_C	fit
QuakeBond™ J300SR	High Density Basalt	**0.0380**	**0.0083**	**98.57%**	0.0008	0.0024	94.49%
	High Density Glass	**0.0381**	**0.0083**	**99.50%**	0.0010	0.0023	98.49%
NRi XT Polyurethane	High Density Basalt	**0.0392**	**0.0084**	**99.69%**	0.9892	0.0023	98.66%
	High Density Glass	**0.0039**	**0.0026**	**98.12%**	0.5905	0.0027	94.15%

Best fit model parameters are shown in **bold**

Table 11. Bond-slip model properties for FRP systems adhered to aluminum substrate

Matrix Material	Fiber Type	Exponential Model			Bilinear Model		
		G_C	V_C	fit	G_C	V_C	fit
QuakeBond™ J300SR	High Density Basalt	604.47	2.5017	99.86%	**0.0004**	**0.0030**	**99.86%**
	High Density Glass	0.0025	4.5838	99.03%	**0.0005**	**0.0029**	**99.03%**
NRi XT Polyurethane	High Density Basalt	0.0052	3.5714	93.22%	**0.0010**	**0.0022**	**93.23%**
	High Density Glass	0.0101	0.0056	99.74%	**0.0007**	**0.0026**	**99.48%**

Best fit model parameters are shown in **bold**

5.5 Finite Element Modeling

The material relations derived thus far are most useful when applied to a numerical model capable of predicting system response. Due to the complex states of stress that can exist, the potential for large deformations to occur under loading, and the material nonlinearities present, a nonlinear finite element approach would be best suited for analysis of FRP reinforced poles. MSC.Marc is a versatile, general-purpose, nonlinear finite element program with several intrinsic features that make it well suited for modeling these structures.

To evaluate the accuracy of the program, a set of nonlinear finite element models was created to reproduce the bond-slip characterization experiments. The results of this analysis are presented in the remainder of this chapter. A comparison is made between the experimentally derived values, and those produced from finite element analysis.

5.5.1 Finite Element Model Parameters

Eight finite element models were produced in MSC.Marc attempting to recreate the results of the FRP lap-shear tests described previously. The metallic substrate and FRP components were modeled using for-node quadrilateral (Q4) shell elements, and the bond

was modeled with three-dimensional eight-node hexagonal interface elements. The nonlinear material properties of the substrate elements are described by the bilinear or trilinear relations presented in section 5.1. Similarly, the tensile material response of the FRP elements are described by the linear relationships found in section 5.2. The bond between these elements is controlled by the interface elements and is described by the exponential or bilinear relationships determined previously.

The geometry of the model represents one half of a bond-slip experimental specimen similar to those shown in Figure 119, divided symmetrically down the middle in the longitudinal direction. The specimens were oriented where the axial direction coincides with the X-axis and the transverse direction lies along the Y-axis. The boundary conditions were selected to mimic the loading applied by the UTM (see Figure 125).

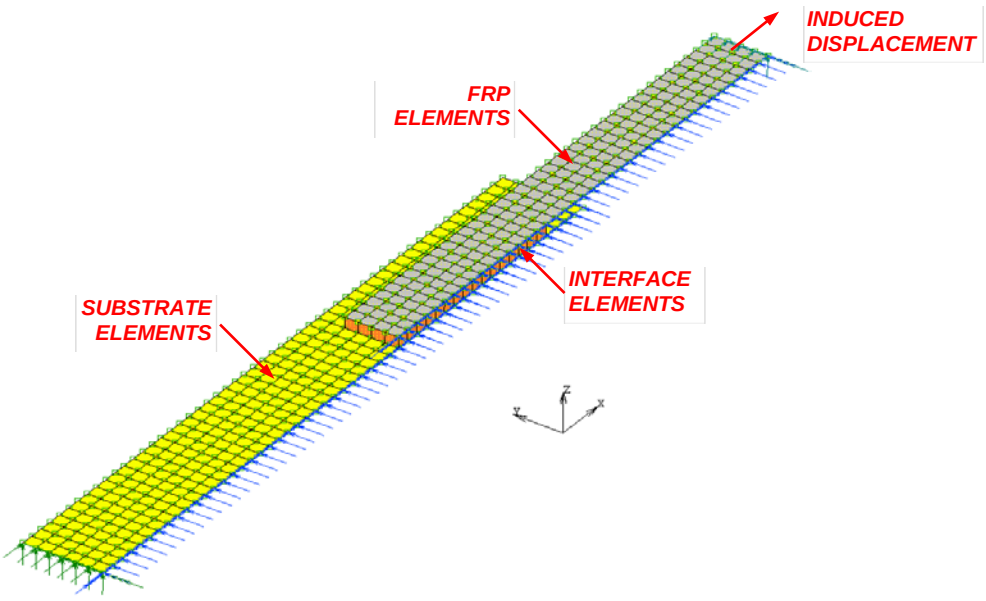

Figure 125. Lap-shear FEM geometry, MSC.Marc

The nodes along the end face of the substrate elements were restrained against displacement in the Y and Z directions and rotation along the X-axis. Each node along the plane of symmetry was restrained from displacements in the Y direction and rotation along the X-axis. Finally, the nodes along the end face of the FRP elements were restrained against displacements in the Z directions and rotations along the X-axis. Additionally, imposed on these nodes was a time-dependent displacement in the X direction. This displacement progressed linearly from zero to 0.2in (5mm) inducing a "displacement controlled" axial tension force in the system. A multi-stepping algorithm within MSC.Marc was used to subdivide the applied displacement into multiple time step increments for analysis.

5.5.2 Finite Element Model Results

The total strain in the axial direction was found for each time step at four points along the top of the FRP. The location of these points relates to the center-point location of the foil strain gauges installed on the experimental test specimens. The equivalent applied loading at each time step was found by summing the internal reaction forces acting on the nodes where displacement had been induced.

The strain values at each strain location determined from the finite element analysis were then plotted against the equivalent applied load at each time step. These plots are shown against the strain data measured during experimental testing and are given in Figure 126 through Figure 129. It can be seen that good agreement exists between the theoretical strain values calculated in MSC.Marc and the measured experimental strain values. This indicates that the two bond-slip forms selected (exponential model for steel and bilinear model for aluminum) reasonably describe the response of the test specimen.

Typical strain distribution contours for the FRP sheets boned to steel and aluminum plates are shown in Figure 130 and Figure 131, respectively. The location of the strain readings that relate to the experimental strain gauge placement are also noted in these figures. It can be seen that the strain remain nearly uniform across the width of the section (Y direction) and tapers axially from a maximum value in the FRP to a minimum value in the substrate through the bonded region.

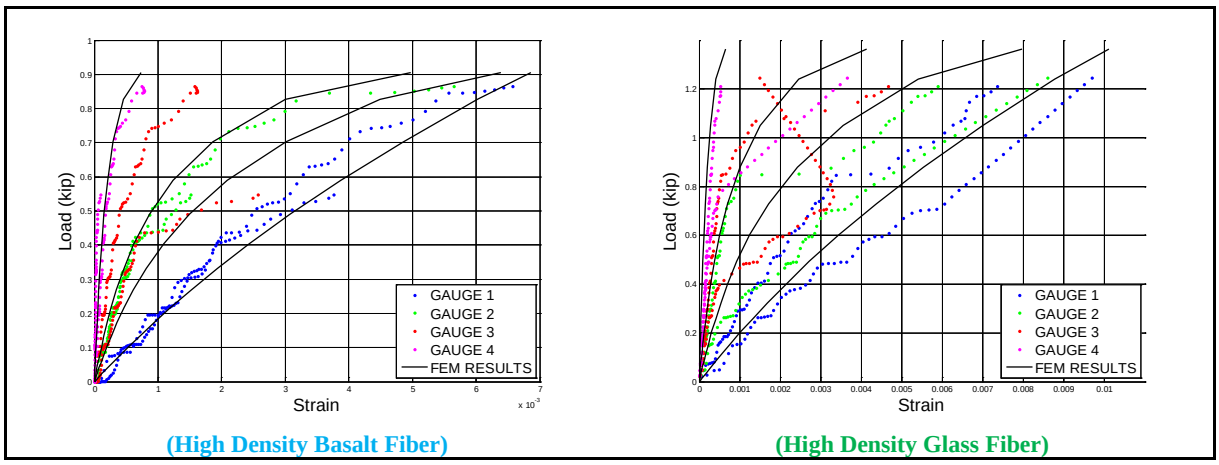

Figure 126. FEM strain comparison of QuakeBond™ J300SR impregnated FRP bonded to steel

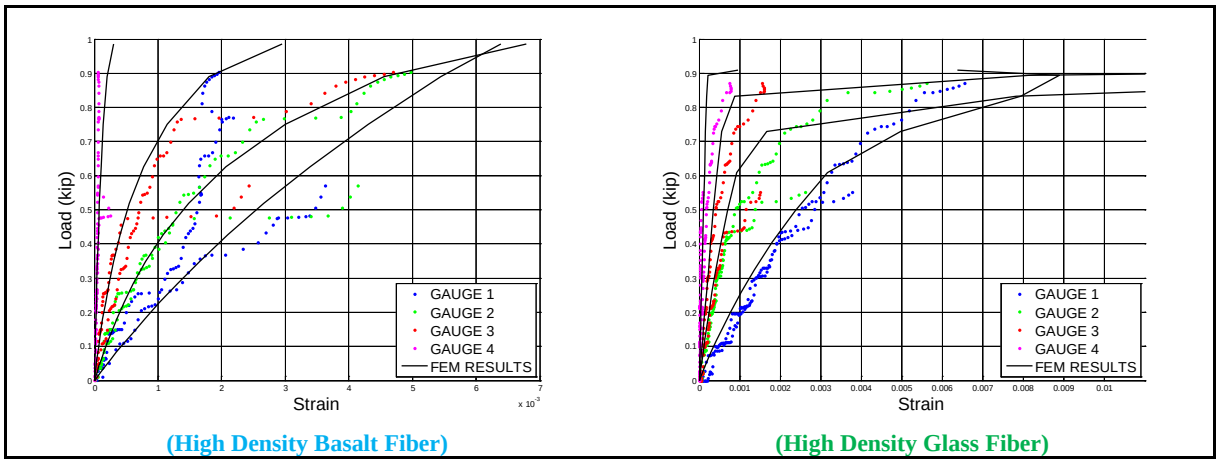

Figure 127. FEM strain comparison of NRi XT impregnated FRP bonded to steel substrate

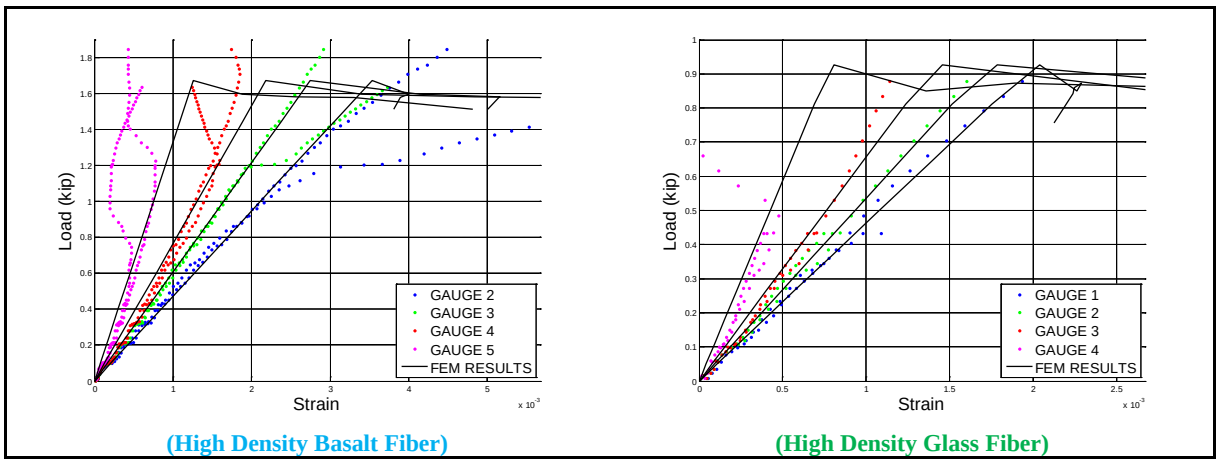

Figure 128. FEM strain comparison of QuakeBond™ J300SR impregnated FRP bonded to aluminum

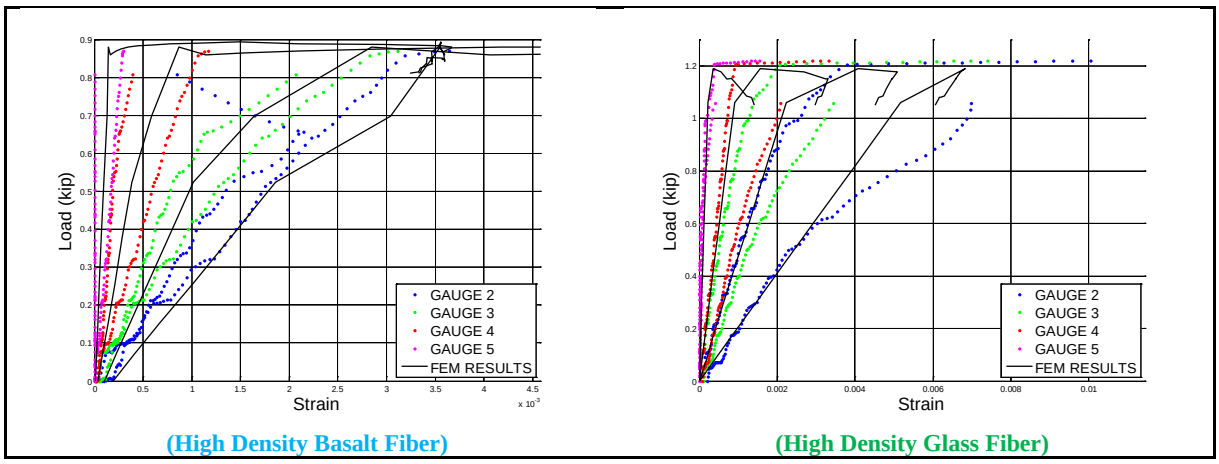

Figure 129. FEM strain comparison of NRi XT impregnated FRP bonded to aluminum

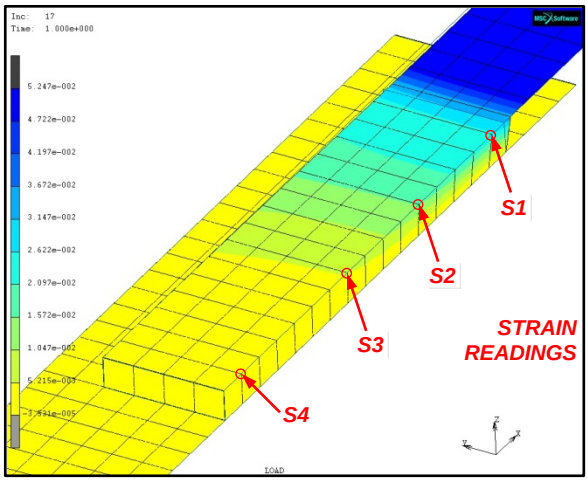

Figure 130. FRP bond to steel strain contour

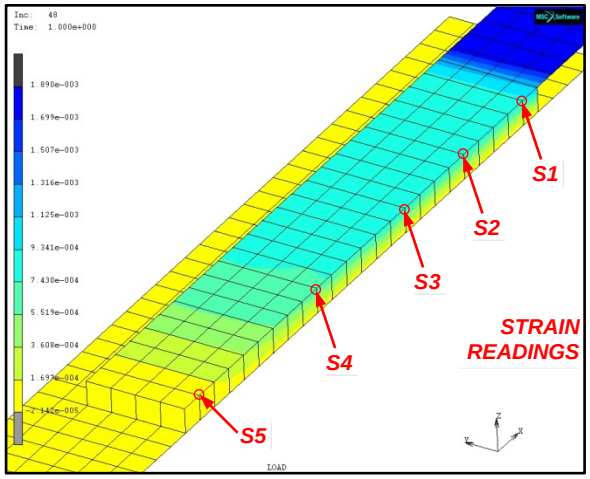

Figure 131. FRP bond to aluminum strain contour

(6) DISCUSSION AND CONCLUSIONS

6.1 Discussion

An analysis of the failure modes of FRP reinforced tapered metallic utility poles is presented in this paper. Five large-scale tests were conducted to determine the prevalent failure mechanism of these structures. These tests involved a steel pipe section, four steel pole sections, and two aluminum pole sections. The pole sections were mechanically damaged by static and dynamic denting induced by hydraulic systems. All of the sections were retrofitted with layers of carbon and/or glass fiber reinforcing systems before being tested to failure.

As expected, the undamaged steel pipe section failed due to the formation of a plastic hinge in the metallic substrate, outside of the reinforced region. As the substrate approached and exceeded the yield capacity of the steel, debonding of the FRP from the substrate was observed beginning on the tension face and traveling circumferentially and laterally outward. The ultimate capacity reached by the pipe exceeded the theoretical yield capacity of the section, but eventually failed from excessive deformations as a result of the formation of a plastic hinge within the substrate. Section S1 failed in a similar fission even though minor damage had been induced in the member beneath the reinforced portion. These tests indicate that when little or no damage is present (when the structure is sufficiently reinforced), the failure mode of the structure relates to the substrate material capacity.

The second set of tests (S2, S3, and A1) involved repair of pole sections with induced damage of substantial depth and spread. The FRP applied to these poles was not successful in

returning the sections to their theoretical undamaged capacity, though the retrofits were sufficient to cause yielding of substrate on the tension face outside the wrapped region. Ultimate failure of these poles resulted from buckling and folding of the compressive FRP leading to hinging of the substrate within the repaired region.

This indicates that the initial failure mode of severely damaged (or insufficiently reinforced) poles repaired with FRP relates first to the compressive capacity of the composite. However, small scale compressive testing of several FRP systems suggests that folding or wrinkling of the composite due to out-of-plane motion of the fibers is the dominant compressive failure mechanism. The transverse fibers in a bidirectional FRP weave provide confinement and help prevent out-of-plane deformations, though wrinkling and folding failures were not completely eliminated for these composite systems.

Two additional pole sections were tested in a cantilever configuration. Section S4 failed when a plastic hinge formed within the damaged section of the pole, but only after resisting a load greater than the theoretical undamaged capacity of the pole. Section A2 yielded to a serviceability failure and the test was ended near the theoretical capacity. The results of these tests show that failure initiated on the compressive FRP face, and the transverse FRP layers contributed significantly to the capacity of the repair.

Due to the location of the induced damage with respect to the pole's access port, a portion of the repair configuration for section S4 did not include continuous circumferential confining fibers. This portion of the FRP reinforcement exhibited minor compressive fiber buckling that ultimately led to the failure of the steel substrate beneath the wrap. The partial confinement capacity within this region is controlled by the transverse fiber's tensile capacity and resistance to slipping. Therefore, an model of the bond-slip relationship for the FRP and

substrate was produced. A set of single-lap bond-slip tests were conducted to characterize the bond response for several FRP repair systems. The results were fitted to exponential and bilinear forms capable of being incorporated into nonlinear finite element analysis. To verify the accuracy of this analysis, models were created to reproduce the results of the bond-slip tests. The FEM results showed excellent agreement with the recorded strain data from the experimental tests.

6.2 Conclusions

Based on the results of the experiments conducted, the following general conclusion can be drawn concerning the failure modes of damaged metallic poles repaired with externally-bonded FRP composites:

- When sufficient reinforcement is provided by the FRP repair system, the dominant failure mode of the structure involves the formation of a plastic hinge in the substrate outside the repaired region.
- If insufficient FRP reinforcement is used, the critical failure mode of the structure is initiated by FRP compressive buckling. Ultimate failure then results from hinging or rupture of the substrate beneath the FRP.
- Transverse fibers oriented circumferentially provide confinement to the compressive fibers and help prevent out-of-plane motion leading to FRP compressive buckling failure. This confining capacity is controlled by the tensile rupture strength of the FRP for circumferentially continuous layers, and the debonding strength of the FRP for discontinuous layers.

- The debonding capacity of the FRP systems tested (for both aluminum and galvanized steel substrates) can be accurately predicted with the use of nonlinear finite element analysis. An exponential model of the bond-slip behavior was shown to be appropriate for the FRP to steel interface, while a bilinear model produced the best results for the FRP to aluminum interface.

6.3 Future Research

Additional research is required to fully implement into practice the findings of this thesis. Specifically, a better understanding of the relationship between the severity of damage induced (dent depth) and the decrease in capacity of the structure must be developed for steel and aluminum poles. Furthermore, little is known about the long term durability of this form of repair. The ambient exposure condition for many metallic pole structures is quite harsh. Therefore, the environmental degradation should be determined before a long-term repair system can be implemented. Finally, the pole structures examined within this thesis have been exposed to artificial loadings intended to simulate flexural stresses produced by a lateral wind load. However, large torsional and shear stresses can also exist within these structures, primarily produced by lateral loads acting on the cantilever arm of standard mast arm assemblies. The effect of these stresses on the repair capacity should be determined.

The impact of these unknown quantities on the capacity of an FRP repair must be established for a complete understanding of the system response. After which, the findings of this thesis can be used to help select an appropriate repair system, as well as design the optimum repair location and fiber orientation to return the structure to its original capacity.

APPENDIX A:

EXPERIMENTAL FRP COMPRESSION TEST DATA

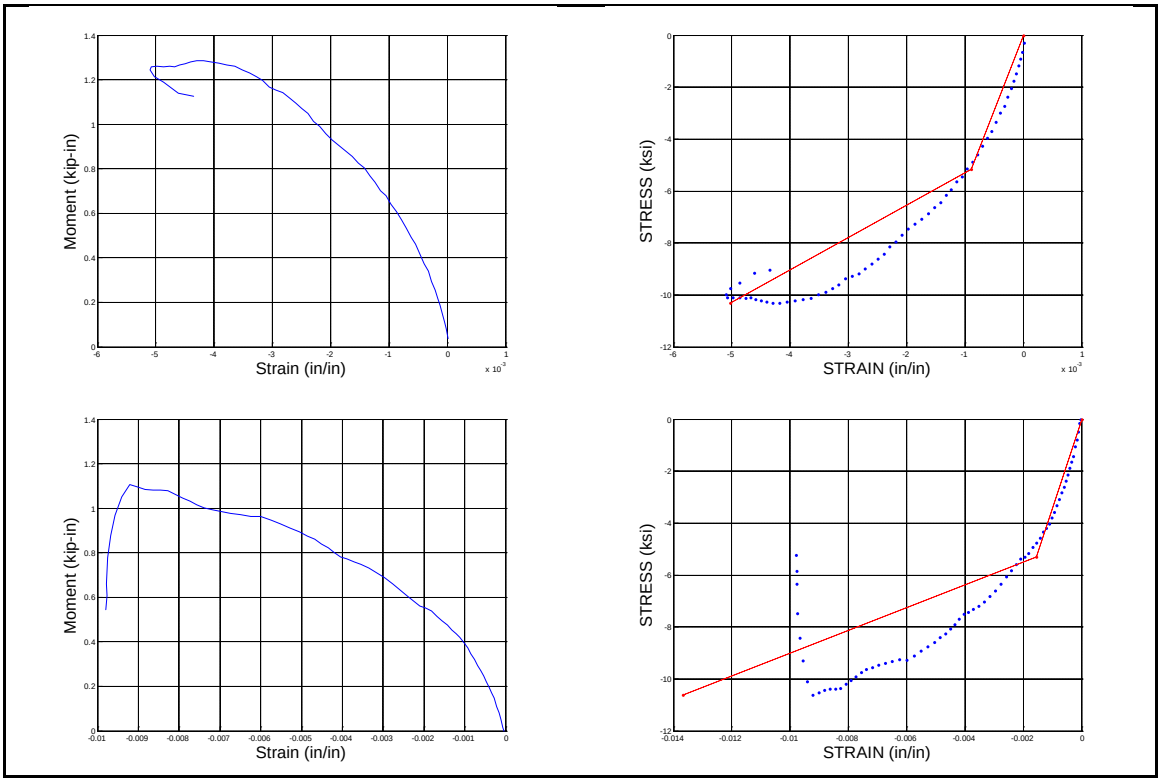

Figure 132. NRi high density basalt compression test data

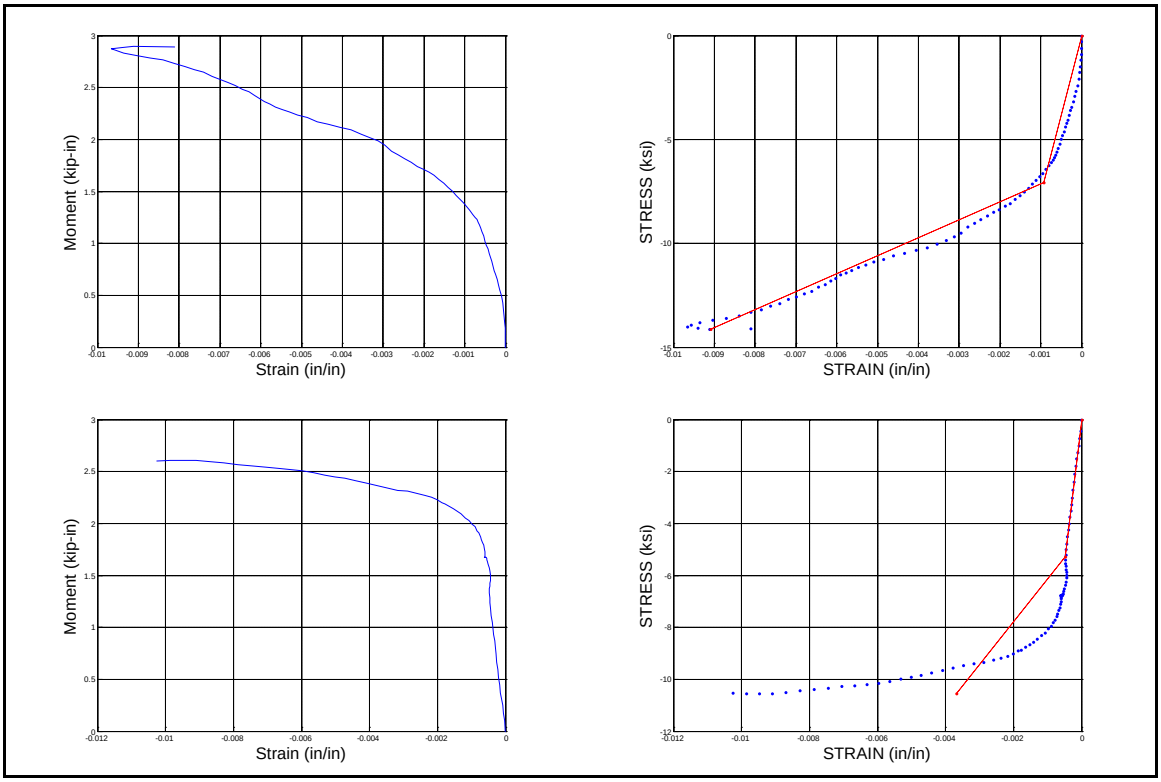

Figure 133. NRi high density glass compression test data

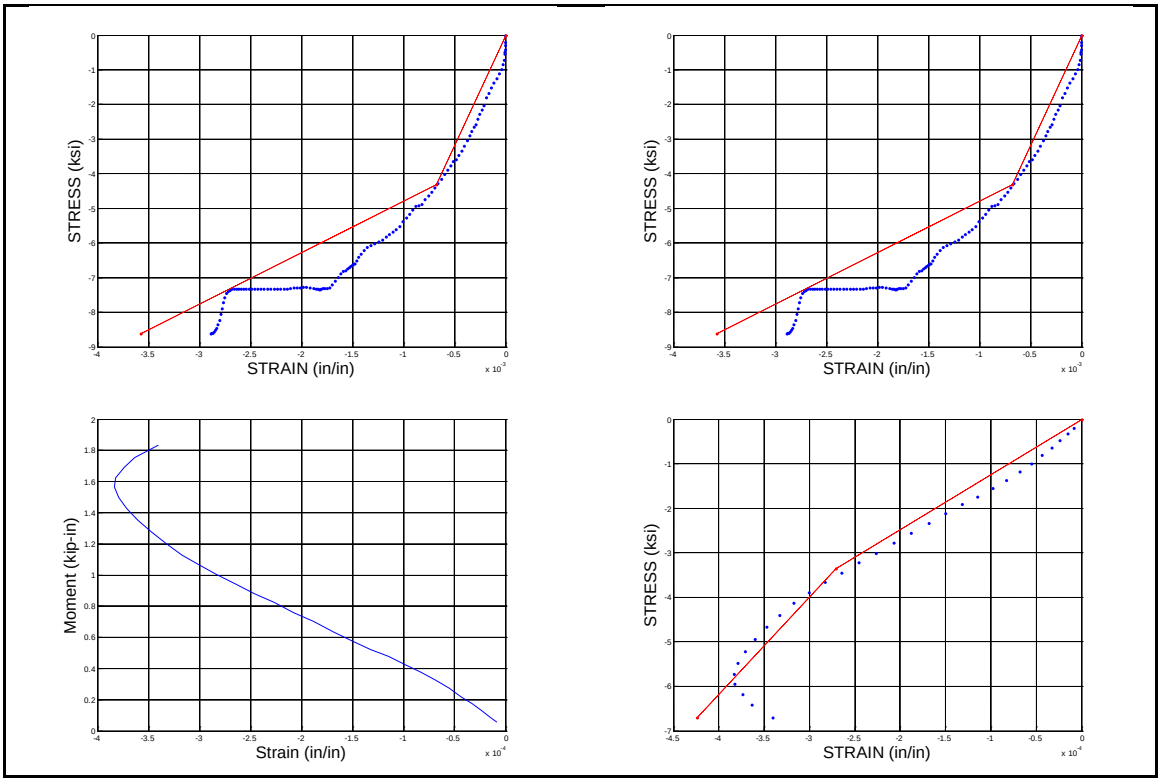

Figure 134. QB high density basalt compression test data

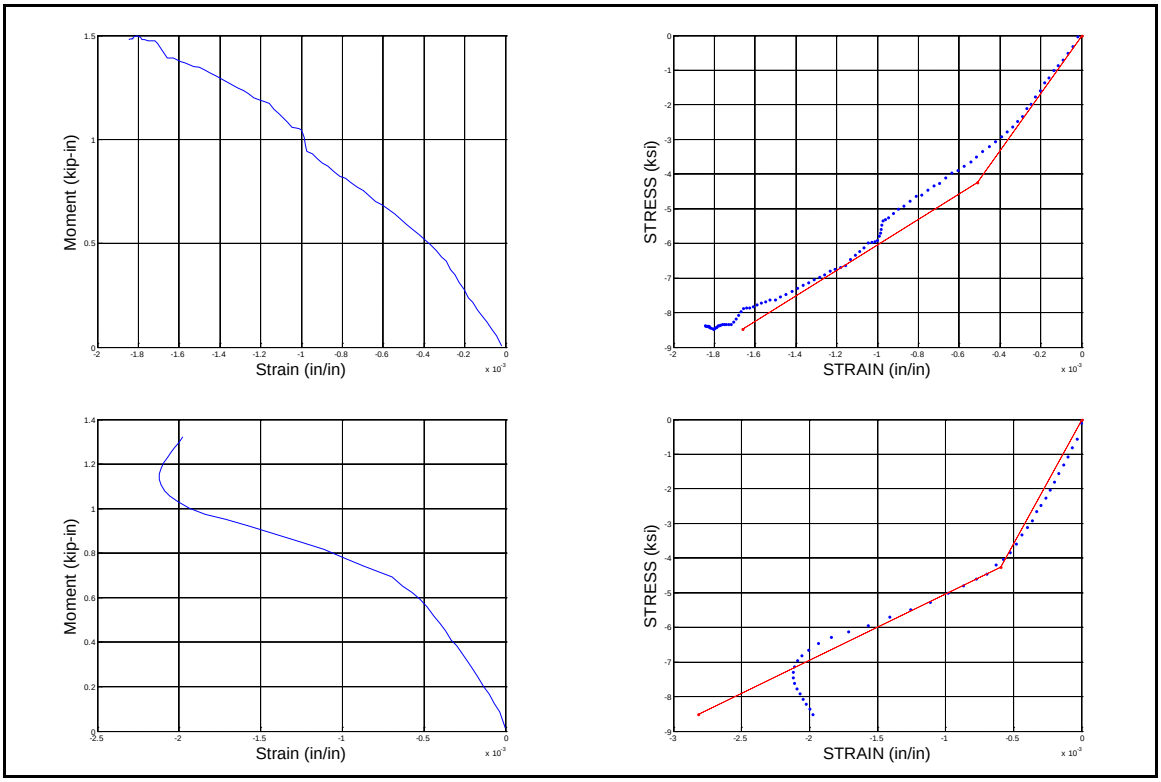

Figure 135. QB high density glass compression test data

APPENDIX B:

EXPERIMENTAL BOND-SLIP DATA

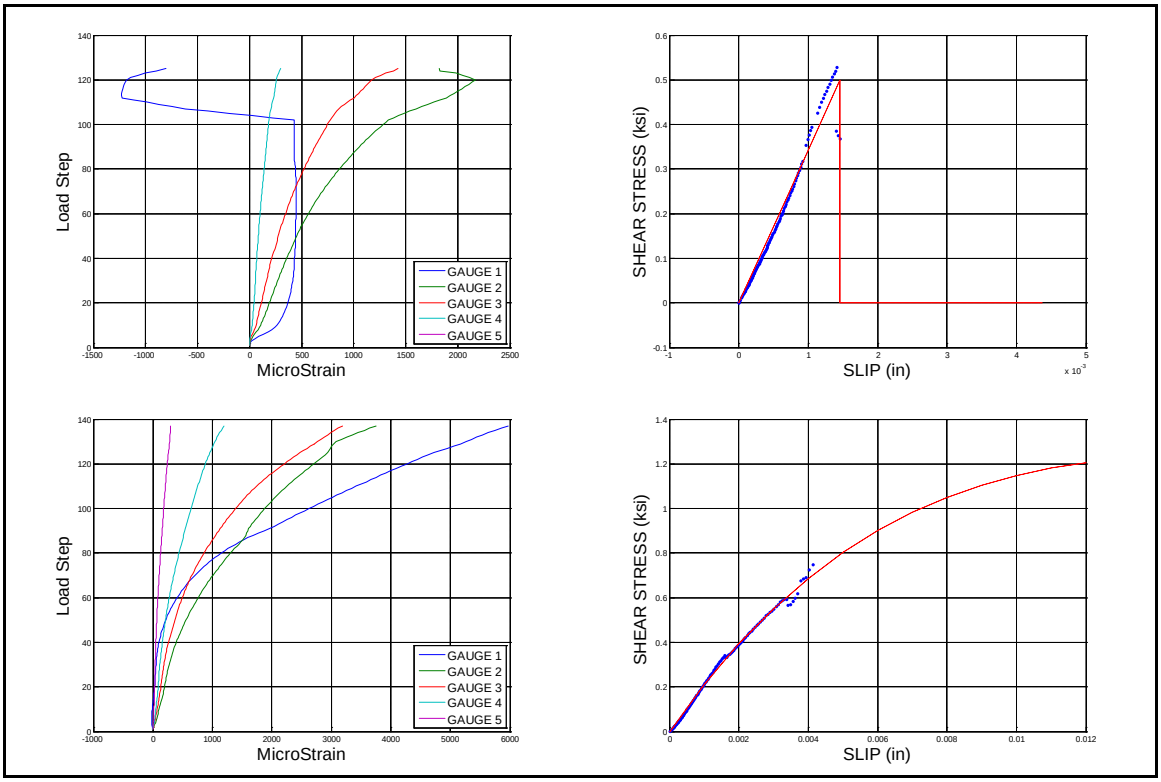

Figure 136. NRi high density basalt adhered to aluminum bond-slip test data

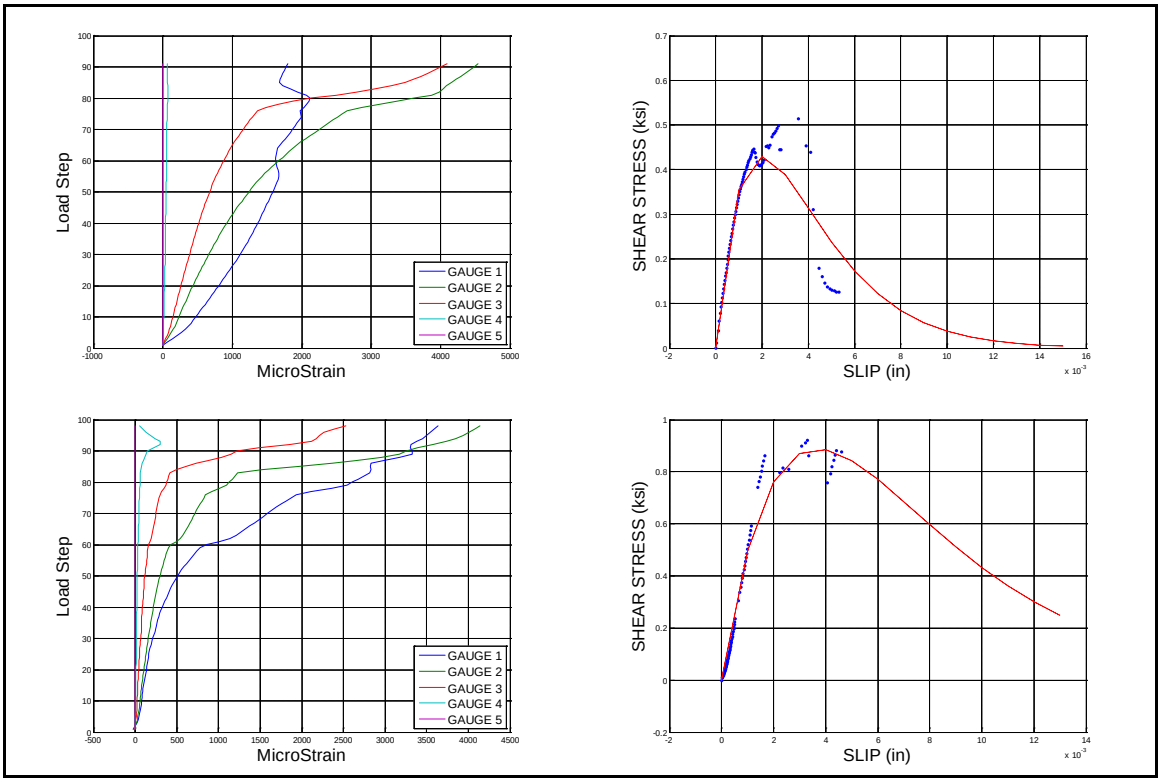

Figure 137. NRi high density basalt adhered to steel bond-slip test data

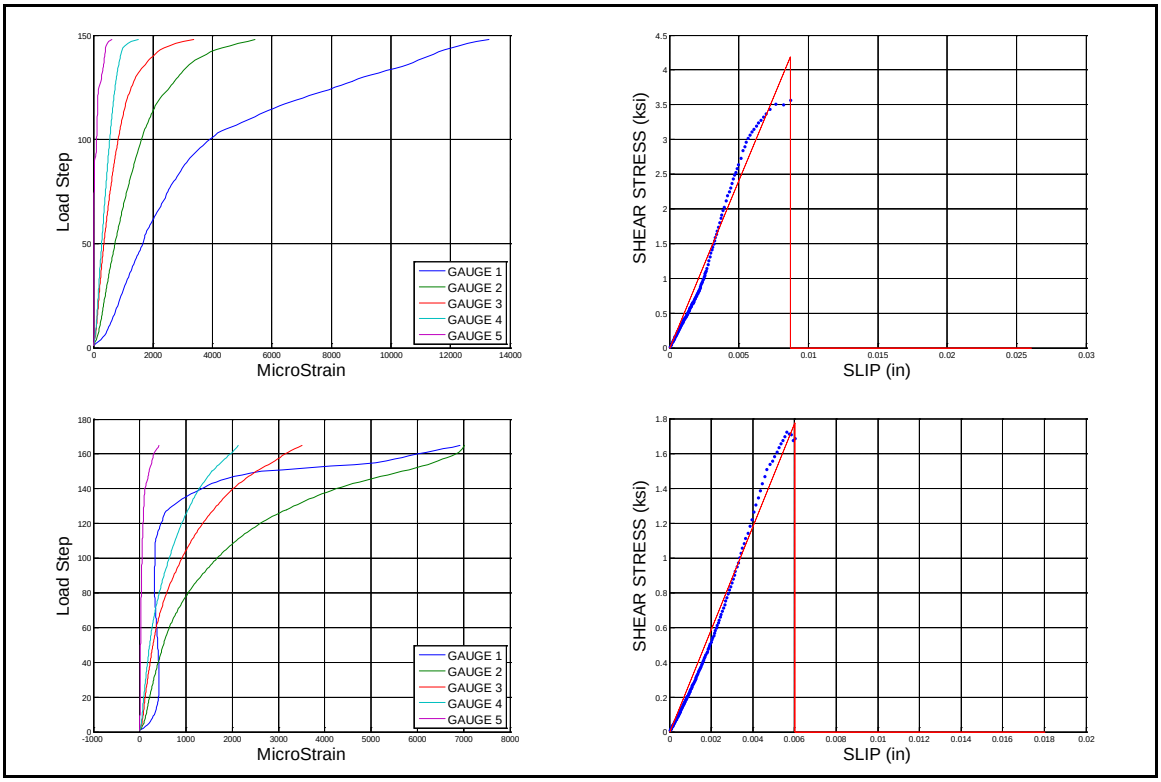

Figure 138. NRi high density glass adhered to aluminum bond-slip test data

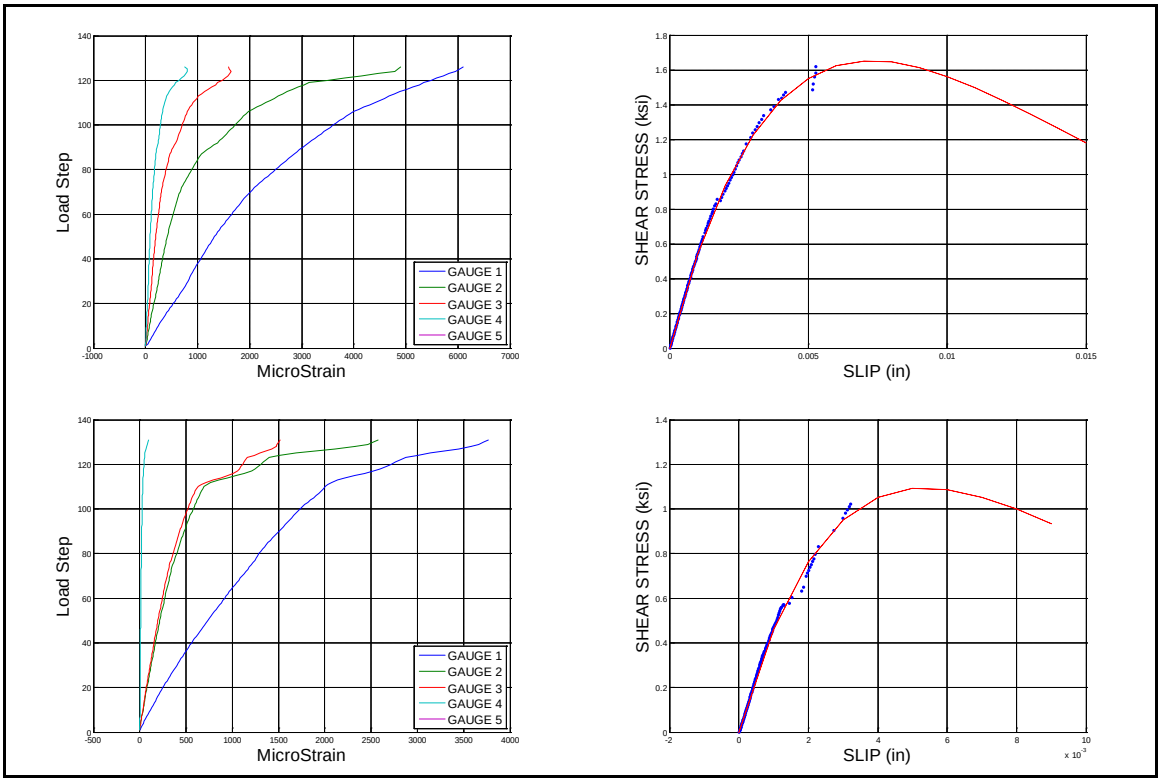

Figure 139. NRi high density glass adhered to steel bond-slip test data

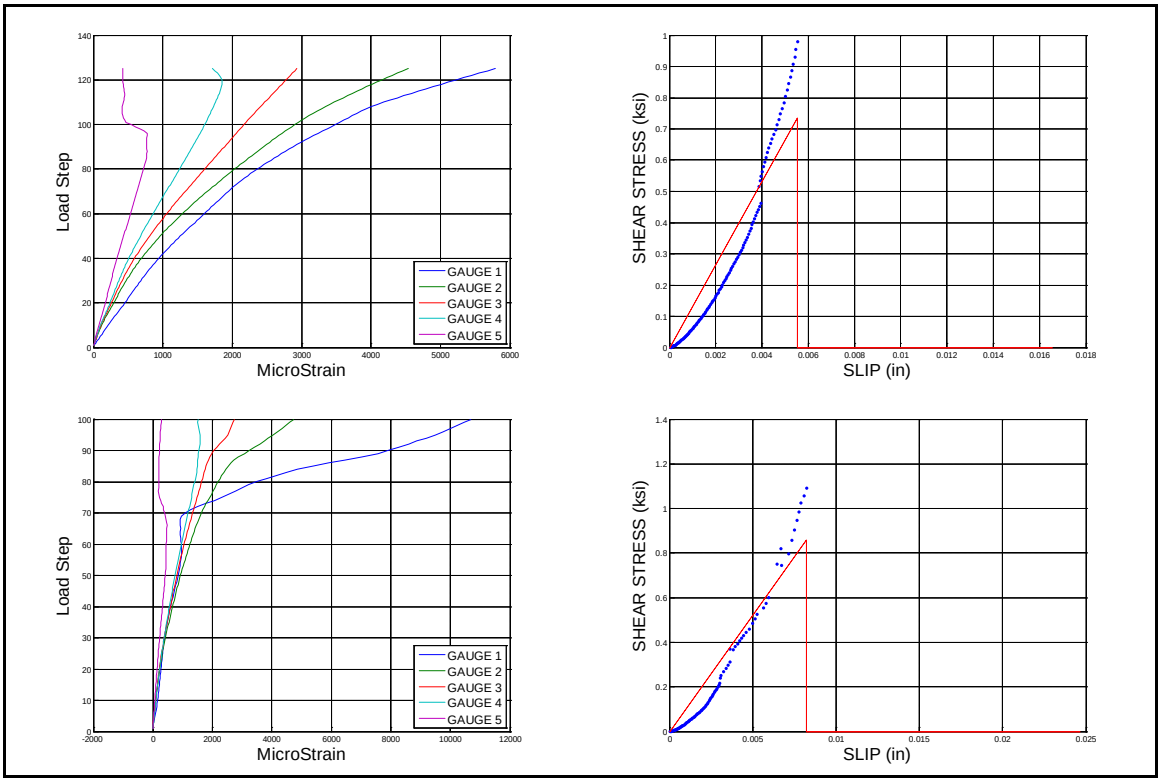

Figure 140. QB high density basalt adhered to aluminum bond-slip test data

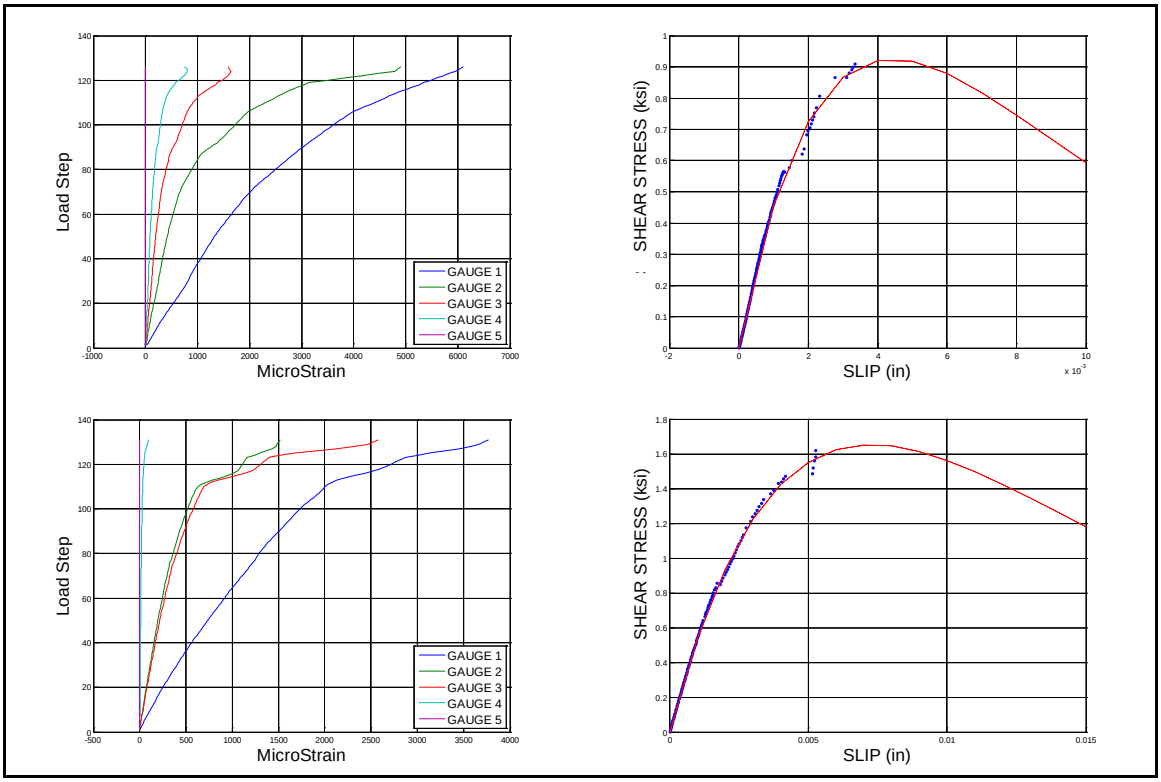

Figure 141. QB high density basalt adhered to steel bond-slip test data

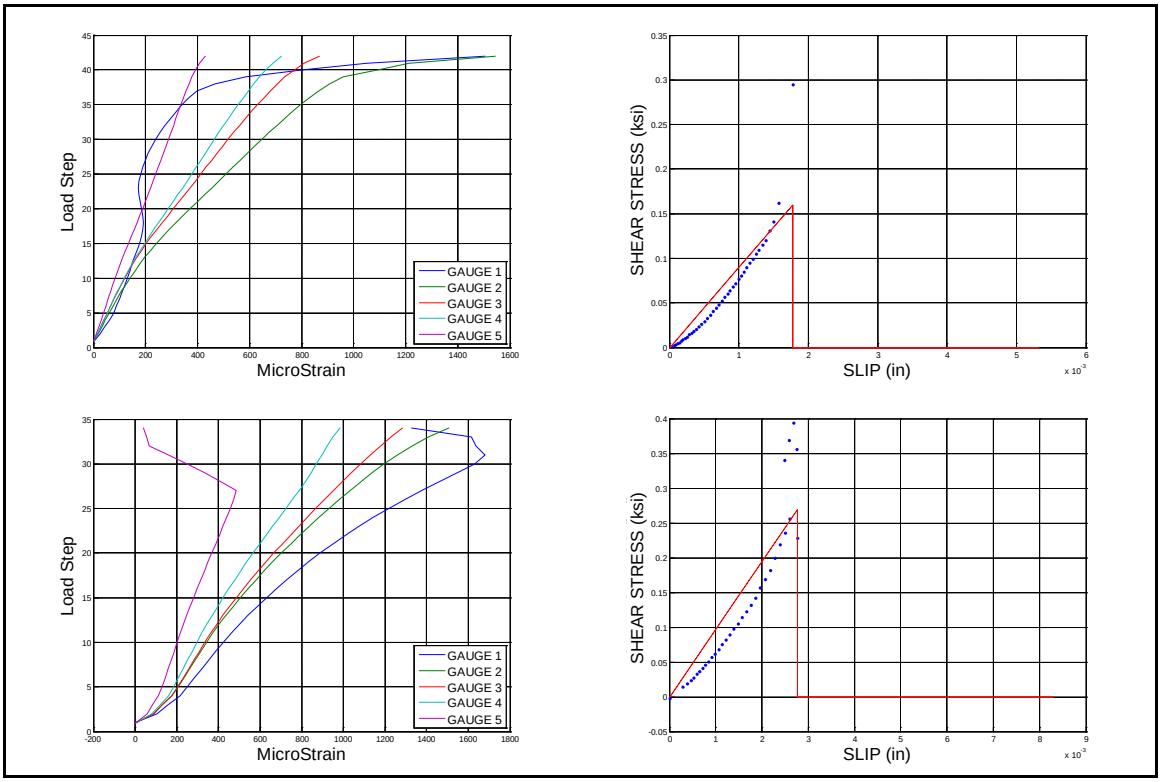

Figure 142. QB high density glass adhered to aluminum bond-slip test data

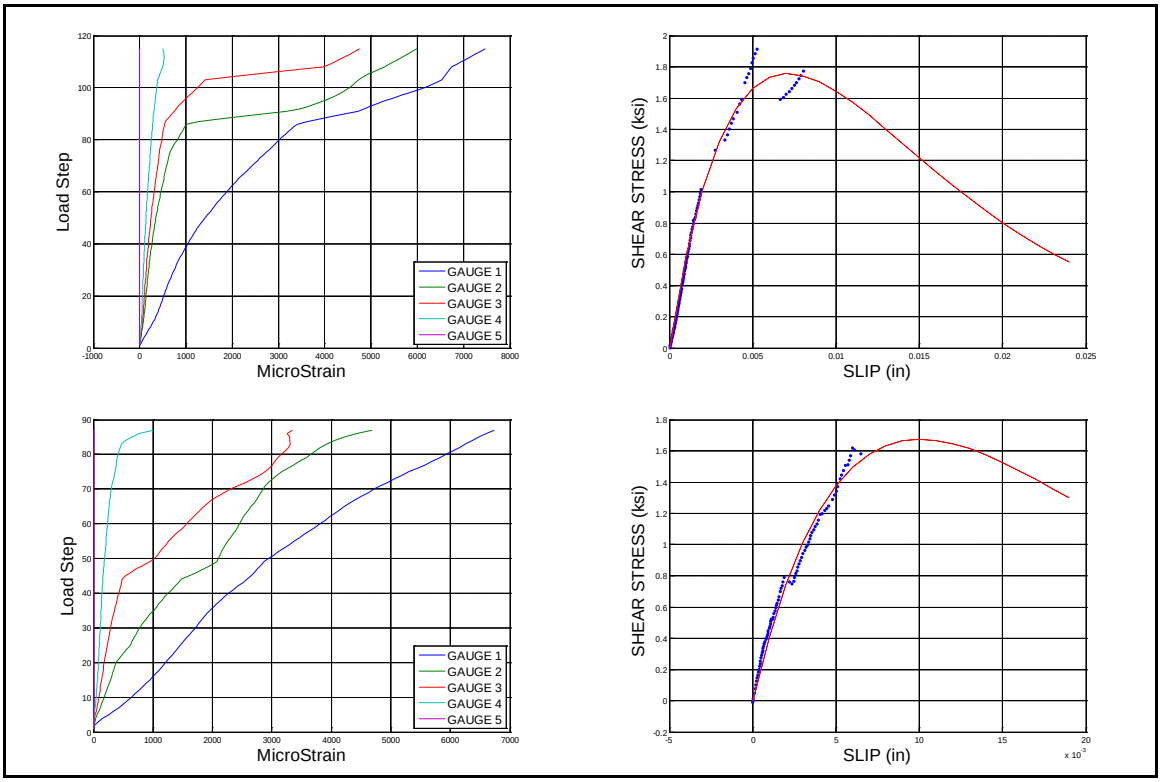

Figure 143. QB high density glass adhered to steel bond-slip test data

system	substrate	specimen #	bond length (in)	width (in)	thickness (in)	area (in^2)	modulus e (ksi)	max load (kip)	max axial stress (ksi)	good for b-s curve?	notes
NRI Basalt	Steel	1	2	1.075	0.090	2.150	1,230	0.880	0.409	Yes	
		2	2	1.036	0.060	2.072	1,230	0.572	0.276	Yes	
		3	2	1.007	0.077	2.014	1,230	0.851	0.423	No	*No grips, previously damaged*
		4	2	1.040	0.073	2.080	1,230	0.724	0.348	~~	*Strain 1*
	Aluminum	1	2	0.895	0.073	1.790	1,230	0.823	0.460	No	*Gage 1 Issue*
		2	3	1.072	0.084	3.216	1,230	1.077	0.335	No	*Strange Strain Data*
		3	3	0.886	0.084	2.658	1,230	0.752	0.283	No	*Reinstalled Gage 1*
1230		4	3	0.951	0.096	2.853	1,230	0.936	0.328	Yes	*Strain Misplacement*
NRI Glass	Steel	1	2	1.000	0.085	2.000	2,395	0.976	0.488	No	*Strain Gage 2 Issue?*
		2	2	1.003	0.061	2.006	2,395	0.770	0.384	No	*Strain Gage 3 Issue*
		3	2	1.100	0.087	2.200	2,395	0.854	0.388	Yes	
		4	2	1.008	0.075	2.016	2,395	0.589	0.292	~~	*Strain Gage 3 Issue*
	Aluminum	1	2	0.960	0.098	1.920	2,395	0.904	0.471	No	
		2	3	1.01	0.089	3.030	2,395	1.215	0.401	Yes	
		3	3	1.003	0.095	3.009	2,395	0.783	0.260	No	*Gage 1*
2395		4	3	0.999	0.075	2.997	2,395	1.142	0.381	Yes	*Gage 1?*
QB Basalt	Steel	1	2	1.010	0.078	2.020	1,841	1.535	0.760	~~	
		2	2	1.028	0.067	2.056	1,841	0.740	0.360	~~	
		3	2	1.014	0.085	2.028	1,841	1.595	0.786	Yes	
		4	2	1.040	0.091	2.080	1,841	1.160	0.558	Yes	
	Aluminum	1	2	1.010	0.084	2.020	1,841	1.428	0.707	No	
		2	3	1.016	0.072	3.048	1,841	1.859	0.610	No	*Strain Misplacement*
		3	3	1.01	0.090	3.030	1,841	1.530	0.505	No	*Strain Misplacement*
1841		4	3	1.045	0.077	3.135	1,841	1.393	0.444	Yes	*Strain Misplacement*
QB Glass	Steel	1	2	1.020	0.072	2.040	1,407	1.320	0.647	~~	
		2	2	1.010	0.072	2.020	1,407	1.282	0.635	Yes	
		3	2	1.009	0.074	2.018	1,407	0.814	0.403	Yes	
		4	2	1.006	0.090	2.012	1,407	0.864	0.429	~~	
	Aluminum	1	2	1.004	0.076	2.008	1,407	1.215	0.605	No	
		2	3	1.048	0.076	3.144	1,407	0.982	0.312	No	*Strain Misplacement*
		3	3	1.017	0.077	3.051	1,407	0.506	0.166	~~	*Strain Misplacement*
1407		4	3	1.008	0.070	3.024	1,407	0.705	0.233	Yes	

~~ usable data, but not preferred

Figure 144. Bond-slip testing notes taken by James Duryea, UCF Structural Research Lab UGRA

REFERENCES

AASHTO, 2009. *LRFD Bridge Design Guide Specifications for GFRP-Reinforced Concrete Bridge Decks and Traffic Railings.*, Washington, DC.: s.n.

ACI-440, 2008. *Guide for the Design and Construction of Externally Bonded FRP Systems for Strengthening Concrete Structures,* s.l.: American Concrete Institute.

Akbar, I., Oehlers, D. & Ali, M., 2010. Derivation of the bond-slip characteristics for FRP plated steel members. *Journal of Constructional Steel Research,* Volume 66, pp. 1047-1056.

Bhattacharya, B. & Seifried, A. E., 2005. *Cracking of Overhead Sign Structures and Their Repair Using Composite Fabric as a Wrap,* Newark, Delaware: Delaware Center for Transportation, University of Delaware, .

Buyukozturk, O., Gunes, O. & Karaca, E., 2004. Progress review on understanding debonding problems in reinforced concrete and steel members strengthened using FRP composites. *Construct Build Mater, 18,* pp. 9-19.

Chahrour, A. H. & Soudki, K. A., 2006. Structural retrofitting of deteriorated concrete lighting poles using FRP sheets in wet layup – field application. *Journal of Composites for Construction, 10 (3),* pp. 234-243.

Fam, A., Witt, S. & Rizkalla, S., 2006. Repair of damaged aluminum truss joints of highway overhead sign structures using FRP. *Construction and Building Materials, 20,* p. 948–956.

FIB Bulletin 14, T. G. 9., 2001. *Externally bonded FRP reinforcement for RC structures,* Lausanne, Switzerland: FIB: Féderation International du Béton.

Gunes, O., Buyukozturk, O. & Karaca, E., 2009. A fracture-based model for FRP debonding in strengthened beams. *Engineering Fracture Mechanics, 76,* p. 1897–1909.

Haber, Z. B., Mackie, K. R., Zhao, L. & Olka, M., 2009. *Thermo-mechanical durability of carbon fiber reinforced polymer strengthened reinforced concrete beams,* Tallahassee FL.: Florida Department of Transportation,.

Haedir, J., Bambach, M. R., Zhao, X. L. & Grzbieta, R. H., 2009. Strength of circular hollow sections (CHS) tubular beams externally reinforced by carbon FRP sheets in pure bending. *Thin-Walled Structures, 47,* pp. 1136-1147.

Hauch, S. & Bai, Y., 1999. *Bending Moment Capacity of Pipes.* s.l., OMAE1999.

Hollaway, L. C. & Cadei, J., 2002. Progress in the technique of upgrading metallic structures with advanced polymer composites. *Prog. Struct. Engng Mater, 4,* p. 131–148 .

Islam, S. M., Zahurul & Young, B., 2011. FRP strengthened aluminum tubular sections subjected to web crippling. *Thin-Walled Structures, 49,* p. 1392–1403.

Ivey, D. L. & Scott, C. P., 2004. *State of the Art Report: Utilities and Roadside Safet,* Washington, D.C.: Transportation Research Board, Committee on Utilities.

Karimi, K., Tait, M. J. & El-Dakjakhni, W. W., 2010. *Experimental Investigation of Two Novel FRP Retrofit Schemes for Strengthening Steel Columns.* Toronto, Ontario, Canada , s.n., p. (Paper No. 364).

Kaw, A. K., 2006. *Mechanics of Composite Materials.* 2nd ed. Boca Raton: CRC Press.

Lanier, B., Schnerch, D. & Rizkalla, S., 2009. Behavior of steel monopoles strengthened with high-modulus CFRP materials. *Thin-Walled Structures, 47,* p. 1037–1047 .

Lu, X., Teng, J., Ye, L. & Jiang, J., 2005. Bond–slip models for FRP sheets/plates bonded to concrete. *Engineering Structures,* Volume 27, pp. 920-937.

Mazzotti, C., Savoia, M. & Ferracuti, B., 2005. *FRP – Concrete Delamination Results Adopting Different Experimental Pure Shear Setups,* Bologna, Italy: Structural Engineering, University of Bologna.

Miller, T. C., Chajes, M. J., Mertz, D. R. & Hastings, J. N., 2001. Strengthening of a Steel Bridge Girder Using CFRP Plates. *Journal of Bridge Engineering, November/December 6,* p. 6.

Pantelides, C. P., Nadauld, J. & Cercone, L., 2003. Repair of Cracked Aluminum Overhead Sign Structures with Glass Fiber Reinforced Polymer Composites. *Journal of Composites for Construction (ASCE), 7,* p. 118.

Pellegrino, C., Tinazzi, D. & Modena, C., 2008. Experimental Study on Bond Behavior between Concrete and FRP Reinforcement. *Composites for Construction, 12,* pp. 1090-0268.

Polyzois, D. & Kell, J. A., 2007. Repair and rehabilitation of wood utility poles with fibre-reinforced polymers. *Canadian Journal of Civil Engineering, 34(1)*, pp. 116-119.

Rizkalla, S. H. & Busel, J. P., 2002. *(2002). Guide for the Design and Construction of Externally Bonded FRP Systems for Strengthening Concrete Structures*, s.l.: ACI 440.2R-02 Committee Report.

Schaumann, P., Keindorf, C. & Brüggemann, H., 2005. *Elasto-Plastic Behavior and Buckling Analysis of Steel Pipelines Exposed To Internal Pressure and Additional Loads.* Halkidiki, Greece, OMAE2005.

Schnerch, D., Dawood, M., Rizkalla, S. & Sumner, E., 2007. Proposed design guidelines for strengthening of steel bridges with FRP materials. *Construction and Building Materials, 21 (5)*, pp. 1001-1010.

Schnerch, D. & Rizkalla , S., 2004. *Strengthening of Scaled Steel-Concrete Composite Girders and Steel Monopole Towers with CFRP.* Adelaide, Australia, CICE2004.

Sen, R., Mullins, G. & Shahawy, M., 2007. Fiber-reinforced polymer repair and strengthening of structurally deficient piles. *Transportation Research Record, 2028*, pp. 221-230.

Su, Y., 2008. *Numerical Simulation of Strengthening Unreinforced Masonry (URM) Walls by New Retrofitting Technologies for Blast Loading* , Adelaide, AU: University of Adelaide School of Civil, Environmental and Mining Engineering.

Zhao, X. L. & Zhang, L., 2007. State-of-the-art review on FRP strengthened steel structures. *Engineering Structures, 29 (8)*, pp. 1808-1823.